Development of Ultrasound Based Techniques for Measuring Skeletal Muscle Motion

By

Jason I. Silver, B.A.Sc.

A thesis submitted to
The Faculty of Graduate Studies and Research
in partial fulfilment of
the degree requirements of
Master of Applied Science

Ottawa-Carleton Institute for
Electrical and Computer Engineering

Department of Systems and Computer Engineering
Carleton University
Ottawa, Ontario, Canada
August 2009

The undersigned recommend to
the Faculty of Graduate Studies and Research
acceptance of the thesis

Development of Ultrasound Based Techniques for Measuring Skeletal Muscle Motion

Submitted by **Jason I. Silver, B.A.Sc.**
in partial fulfilment of the requirements for the degree of
Master of Applied Science

Y. Ono, Thesis Co-Supervisor

A. Adler, Thesis Co-Supervisor

H. Schwartz
Chair, Department of Systems and Computer Engineering

Carleton University
2009

Abstract

This thesis examines the use of ultrasound imaging to study human skeletal muscle in terms of its relative motion and stiffness. The thesis provides background information on skeletal muscle anatomy, ultrasound physics and techniques that are currently used to study muscles. This is followed by a presentation and analysis of simulation and in vivo results.

In order to accurately study muscle motion, a method has been developed to remove the effects of motion artefacts. This methodology as well as all of the other algorithms implemented during research is evaluated in terms of its accuracy and effectiveness during simulation and in vivo experiments.

A simulation environment was constructed to mimic the conditions expected during in vivo experiments. These simulation results as well as software simulations and in vivo results suggest the potential of the developed ultrasonic methodology as a means with which to study skeletal muscles in a novel manner.

Acknowledgements

I would like to thank my supervisors Dr. Yuu Ono, Associate Professor of Systems and Computer Engineering, Carleton University and Dr. Andy Adler, Professor of Systems and Computer Engineering, Carleton University for their expertise, guidance and encouragement. I appreciate both the time and the effort that they provided me with throughout my graduate studies.

I would also like to express my appreciation to Carleton University and the Natural Sciences and Engineering Research Council of Canada (NSERC) for the opportunity and the financial support that they provided for this research.

I am grateful to my colleagues Rachel Morehouse and George Tanev for their efforts and assistance throughout my research work and to Dr. Peter Brands (ESAOTE Europe) for his technical assistance.

Finally, a special thanks to my friends and family for their enthusiasm, patience and support.

Table of Contents

List of Figures

Nomenclature

List of Abbreviations

Abbreviation	Description
A-mode	Amplitude Modality of ultrasound imaging
B-mode	Brightness Modality of ultrasound imaging
EMG	Electromyogram
EMS	Electrical Muscle Stimulator
FM	Frequency Modulated
GUI	Graphical User Interface
LPF	Low Pas Filter
MMG	Mechanomyogram
M-mode	Motion Modality of ultrasound imaging
MRI	Magnetic Resonance Imaging
MSE	Mean Squared Error
PRF	Pulse Repetition Frequency
PZT	Piezoelectric Material used in ultrasound transducers
RF	Radio Frequency
ROI	Region of Interest
SNR	Signal to Noise Ratio
2D	Two-Dimensional

List of Symbols

Symbol	Description	Units
A	Received ultrasonic signal amplitude	
c	Ultrasound propagation velocity	m/s
Δd_z	Estimated instantaneous displacement between two consecutive temporal samples in the ultrasonic beam direction, z	m
d_z	Estimated accumulated displacement in the ultrasonic beam direction, z	m
d_{ext}	Estimated accumulated displacement occurring at a bone boundary representing external or motion artefact displacement in the ultrasonic beam direction, z	m
$d_{artifact}$	Estimation of accumulated displacement at any depth due to external or motion artefact in the ultrasonic beam direction, z	m
d_{int}	Estimated accumulated internal displacement after motion artefact removal in the ultrasonic beam direction, z	m
ε	Axial strain	%
f_c	Ultrasonic center frequency	Hz
f_{dem}	Frequency of reference signal used during demodulation	Hz
$\bar{f_c}$	Estimated center frequency of received ultrasonic signal	Hz
θ	Angle between direction of target motion and ultrasonic beam direction	radians
ϕ	Phase shift between transmitted and received ultrasound signals due to target motion	radians
$\Delta\phi_z$	Estimated phase shift between two consecutive temporal samples	radians

I	In-phase demodulated ultrasonic signal	
i	Scan line number	
L_{ab}	Axial distance between depth locations a and b	m
m	Temporal sample number	
n	Axial sample number	
n_{ab}	Axial region within depth locations a and b inclusively	
Q	Quadrature demodulated ultrasonic signal	
$r_{n,m}(N,M)$	Complex autocorrelation with axial lag N and temporal lag M in the axial and temporal directions n and m respectively	
s_t	Transmitted ultrasonic signal	
s_r	Received ultrasonic signal	
s_{ref}	Reference sinusoidal signal used for demodulation	
SF_z	Scaling factor used for depth scaling	
T	Slow time	seconds
t	Fast time	seconds
T_s	Axial sampling period	seconds

u	Received complex baseband signal	
ν	Estimated velocity	m/s
ω_c	Ultrasonic angular center frequency	rad/s
ω_{dem}	Angular frequency of reference signal used during demodulation	rad/s
ω_d	Doppler shift angular frequency	rad/s
ω_i	Instantaneous angular frequency of received ultrasonic signal	rad/s
z	Unit vector in the direction of the ultrasonic beam	

Chapter 1:

Introduction

The following chapter is an introduction to this thesis and will provide an overview of the entire document and its organization. In addition, the objectives and contributions made throughout research work will be outlined.

1.1 Overview

The properties and characteristics of muscles and their operation have been studied since as early as the 1600's. Specifically, in humans, the musculature of the body has a great deal to do with the overall health and well-being of an individual. For example, an athletic injury or a muscular disorder can cause a number of health related issues. As such, understanding the physical properties of muscles and how and why they move is of ongoing interest to some medical practitioners. The motivation behind the research done for this thesis is driven by the ongoing need to better understand the musculature. By increasing both the amount of information that can be measured as well as the accuracy of existing measurable quantities, muscles and their effect on well-being can be better understood. Providing a unique muscle measurement system capable of making very accurate and novel muscle measurements could prove to be a valuable resource for the study of muscles in applications such as sports medicine and muscular diseases.

1.2 Problem Statement

The thesis research to follow focuses on employing ultrasonic hardware along with digital signal processing techniques to analyze human skeletal muscle at rest and during forced contraction. Although ultrasound techniques have been previously employed to provide information about the musculature, this thesis strives to develop and test the validity of a novel method with which to acquire and process these signals. Specifically, the methods implemented and developed in this thesis will provide displacement, velocity and strain data obtained during tissue motion. In an effort to provide this information, the thesis also analyzes the effects of motion artefacts occurring during data acquisition. Removing the effect of motion artefacts during ultrasound measurements is a widely acknowledged problem and a solution, as it directly applies to the applications discussed in this thesis, is provided.

1.3 Objectives

The goal of the developed ultrasonic system is to be able to measure motion in terms of the displacement and velocity of human skeletal muscles and their surrounding tissues. These measurements should be accurate on the order of microns and should be obtainable both globally on the tissue area as a whole and internally at any location inside the tissue. In addition, information about the relative strain experienced in an imaged area should be provided. These goals are made more accurate by an analysis and development of a novel method with which to remove the effects of potential motion artefacts occurring during data acquisition.

In order to obtain the overall goal of an ultrasonic muscle measurement system, a number of more specific objectives were defined. To begin with, simulations had to be designed in order to allow testing and validation of the developed methodology. These simulations were done using both software techniques and phantom systems designed and developed to mimic the human tissues of interest. In addition, data preprocessing had to be performed in order to obtain a signal from the ultrasonic hardware equipment useful to this thesis research. Finally, in vivo experiments were designed in order to demonstrate the effectiveness of the developed methodology in actual human trials.

It should be noted that the main areas of this thesis are in the experimental design and data processing techniques used to develop and test a methodology that can be used to measure muscle characteristics. It does not deal with the construction of ultrasonic hardware or the exact interpretation of results obtained during in vivo experiments. Instead, these concepts are left as endeavours to be taken on in the future.

1.4 Thesis Contributions

The following is a list of the main research contributions demonstrated in this thesis which will be explained thoroughly in the chapters to follow:

- Developed experimental procedures to obtain ultrasound data during in vivo and phantom simulation testing. In addition, data preprocessing algorithms were designed to allow software analysis of the data acquired from the ultrasound hardware.

- Developed both software and tissue mimicking phantom simulation environments used to test the muscle measurement system. These simulations were also used to evaluate the accuracy of the ultrasonic hardware and both existing and developed ultrasonic techniques.
- Implemented a strain estimation algorithm to obtain stiffness information as well as both a quadrature demodulation and a two dimensional autocorrelation algorithm used to obtain displacement and velocity estimations from received ultrasonic signals.
- Designed and implemented an algorithm to remove the effects of motion artefacts occurring during data acquisition.
- Developed a graphical user interface (GUI) to allow simple display of and navigation through an acquired ultrasound data set.

1.5 Thesis Organization

Chapter 1 introduces the concepts discussed throughout this thesis.

Chapter 2 provides background information about human skeletal muscle physiology and the principles of ultrasonic imaging. In addition, a discussion of the current techniques used to measure muscle properties and motion is provided.

Chapter 3 describes the ultrasonic hardware used as well as the data preprocessing that was developed. It also provides details about the designed GUI.

Chapter 4 defines the established mathematical model for acquired measurements and provides a mathematical justification of the data processing used to obtain estimations of displacement, velocity and strain. It concludes with a discussion of algorithm accuracy.

Chapter 5 provides details about the developed motion artefact removal algorithm and concludes with a discussion of algorithm accuracy and limitations.

Chapter 6 discusses the simulation environment as it applies to phantom development, experimental design and experimental procedure. It includes results obtained during these experiments and an accuracy evaluation of the methodology employed.

Chapter 7 pertains to in vivo experiments. It provides experimental design, procedure and results obtained during in vivo human skeletal muscle experiments. The chapter concludes with an evaluation of algorithm accuracy.

Chapter 8 concludes this thesis by giving a summary of the major findings and a list of recommendations for future work.

Chapter 2:

Background Review

In this work, we study muscle physiology using ultrasound technologies. The following section serves as an outline of human muscle physiology, the physics and principles of medical ultrasound imaging and the current technologies used to study the human musculature as mentioned in a variety of different literature sources.

2.1 Human Muscle Physiology

The human body is made up of a complicated system of muscles used for a number of different purposes. There are three different types of muscles that occur in the human body: skeletal muscle, cardiac muscle and smooth muscle. Skeletal muscles are generally attached to the bones of the skeleton, enabling them to control body movement. Cardiac muscles are found only in the heart and together with skeletal muscles, are classified as striated muscles. Smooth muscle is the primary muscle of the internal organs such as the stomach, urinary bladder and blood vessels. In general, skeletal muscles can be thought of as the voluntary muscles whereas cardiac and smooth muscles are more involuntary. In comparison with cardiac and smooth muscles, skeletal muscles are unique in that they only contract in response to a signal from a motor neuron and that they experience fatigue

[1]. Skeletal muscle is the target of the ultrasound imaging procedure we are studying. Therefore, the remainder of this chapter will ignore both cardiac and smooth muscle.

2.1.1 Skeletal Muscle Physiology

Skeletal muscle is the most abundant type of muscle in the human body and accounts for approximately 40% of total body weight [1]. They are, as their name suggests, responsible for the movement and positioning of the skeleton and are attached at their origin to a large area of bone. The other end of the muscle, called the insertion, tapers into a tendon which is also attached to bone [2]. The skeletal muscles themselves are a collection of muscle fibers arranged with their long axes in parallel [1]. The muscles exhibit a resting potential during a resting state and, when appropriately stimulated, an action potential during an active state [3]. The following section provides an overview of skeletal muscle contraction.

2.2 Skeletal Muscle Contraction

When dealing with the mechanical motion of skeletal muscles, the first concept to discuss is that of the motor unit. A motor unit is comprised of all the muscle fibers that are supplied by one motor neuron. A motor neuron will, through its axonal branches, supply a number of muscle fibers scattered throughout the muscle. If a motor neuron fires, all of the muscle fibers in that unit will contract at the same time, producing a synchronous electrical discharge called an action potential and a generation of force called a twitch [4]. No visible change occurs in the muscle fiber during and immediately following the action potential. This period is called the latent period and lasts from 3 ms to 10 ms [2].

The action potential and subsequent twitch of a muscle are caused by a chemical reaction in the muscle fiber that is not vital to the understanding of the thesis work to follow. Any motor unit will remain in its resting state until it is provided with an adequate stimulus causing it to enter its active state.

The resting potential of the internal medium of a motor unit is in the range of -50 mV to -100 mV [3]. A muscle may be stimulated via its attached nerve or, more directly, by applying a small electric shock across its membrane [5]. When an excitable membrane or neuron has an action potential in response to an adequate stimulus, the ability of that membrane to respond to a second stimulus of any sort is markedly altered. During an action potential, the membrane cannot respond to any stimulus, no matter how intense. This interval is referred to as the absolute refractory period. It is followed by the relative refractory period, wherein an action potential can be elicited by an intense super threshold stimulus. For example, a nerve axon has an absolute refractory period of 1 ms resulting in an upper limit of repetitive discharge of less than 1000 impulses per second [3]. The refractory period necessary to restore the membrane to its resting potential is usually between 1 ms and 2 ms [2].

The process of muscle contraction takes about 50 ms and the relaxation of the fibers can take another 50 ms to 100 ms. Due to the fact that the refractory period is much shorter than the time needed for contraction and relaxation, the muscle fibers can be maintained in the contracted state so long as they are stimulated frequently enough. This sustained contraction is referred to as tetanus [2]. In general, when stimuli are given at a rate of 1 Hz the muscle responds with a single twitch. When the stimulus frequency is increased to between 5 Hz and 10 Hz the individual twitches begin to fuse together into a single twitch which may fluctuate at the stimulus frequency giving rise to a tremulous response called clonus [6]. At a stimulation rate of 50 Hz, the muscle goes into the smooth, sustained contraction of tetanus. The force of contraction is greater in clonus and tetanus than in a single twitch. During normal use of skeletal muscles, the individual fibers go into tetanus for brief periods of time rather than simply undergoing single twitches [2]. This concept can be seen below in Figure 2.1.

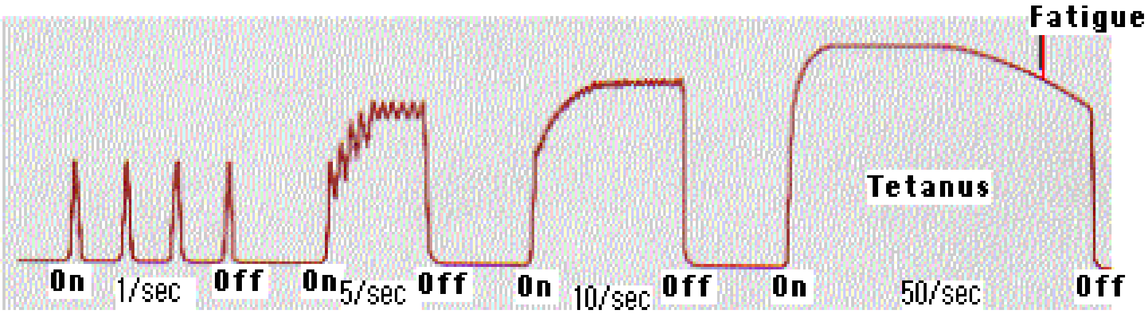

Figure 2.1 Skeletal muscle contraction. Courtesy of John Kimball [2].

A tetanic contraction remains steady until the stimuli are withheld or until fatigue sets in. The result of fatigue is that the latent period becomes longer and the muscle contractions become smaller and more prolonged with slower relaxation. Ultimately, this results in the fact that the muscle does not return to its original length [6].

2.2.1 Electrical Muscle Stimulation

As stated above, a motor unit can be stimulated externally by an electric shock across its membrane. There are many commercial devices available to stimulate muscle contraction and are often referred to as electrical muscle stimulators (EMS) or nerve electrical muscle stimulators (NEMS) [7]. These devices are used for a variety of purposes including sports training and rehabilitation [7], nerve blocks [8], [9], to counteract bone loss and muscle atrophy [10] and to induce muscular growth [11]. An EMS is used in this thesis research to force the contraction of skeletal muscles using two adhesive electrodes placed on the skin surface above a muscle of interest.

2.3 Principles of Ultrasound

Ultrasound imaging uses electrical-to-acoustical transducers to generate repetitive bursts of high frequency sound. These pulses travel into the soft tissue of the body and reflect back to the transducer [12]. By analyzing the signal received at the transducer, measurements can be made and images can be created that represent quantities from within the tissue. Ultrasound itself is defined as acoustic waves with frequencies above approximately 20 kHz, which is the threshold that can be detected by humans. Medical instrumentation typically uses only the portion of the ultrasound spectrum from 1 MHz to 10 MHz. This range is used in order to compromise between spatial resolution which increases with frequency and penetration depth which decreases with frequency [13]. The following section outlines the basic physics behind ultrasound, provides details about ultrasonic transducers and gives a brief description of some of the most common ultrasound imaging modalities.

2.3.1 Ultrasonic Transducer Elements and Probes

Strictly speaking, an ultrasound transducer element is the device that actually converts electrical transmission pulses into ultrasonic pulses, and conversely, ultrasonic echo pulses into electrical echo signals [14]. An ultrasonic probe contains any number of ultrasonic transducer elements arranged in a number of different ways depending on the intended application. Although there are differences between the transducer elements and probes used, there are some common features among all probes and transducers used. All ultrasonic probes contain at least one transducer element made up of a piezoelectric material, matching layer(s) and a backing layer [14]. A diagram of a simple ultrasound imaging probe with a single transducer can be seen in Figure 2.2 below. Usually, there is also a lens which in the case of transducer array probes tends to extend across all the transducer elements. The piezoelectric material (lead zirconate titanate: PZT) used has the property that an applied electric field will produce mechanical displacement, which in turn causes an acoustic wave. Conversely, they also satisfy the reciprocal property that a mechanical displacement will induce an electric potential which can be used to sense an acoustic wave [12].

Matching layers are used to make sure that enough of the transmitted ultrasonic wave propagates into the tissue to be imaged rather than being reflected off of its surface. They are mounted in the probe on the exit side (facing the tissue) of the PZT [15].The acoustic impedance of the PZT is about 20 times larger than human tissue and as such, without matching layers, the majority of the sound wave would be reflected at the PZT-tissue boundary. More on acoustic impedance is described in Section 2.3.2 below. The matching layer(s) aim is to more closely match the acoustic impedance of the probe to that of human tissue, resulting in a much better transmission of a sound waves into human tissue.

The backing layer, located behind the transducer element(s), is used in ultrasonic probes for two different reasons. Firstly, when the front face of the transducer is moved forward, by the electrically induced mechanical motion, an acoustic wave is initiated forward into the medium and backwards into the PZT material itself. The backwards travelling wave will hit the back face of the transducer and reflect toward the front face again [12]. Since this wave is not from within the medium being imaged, it should be removed. It is also possible that some of the transmitted wave will be reflected back into the probe by the probe-tissue interface [14]. This backwards travelling wave should also be removed. A backing layer is used, in either case, to remove the effects of unwanted sound waves. The ideal backing layer should have an acoustic impedance equal to that of the PZT material so that there is complete transmission from PZT to backing layer. In addition, the backing layer should have a high absorption coefficient to prevent ultrasonic energy from re-entering the PZT material [15].

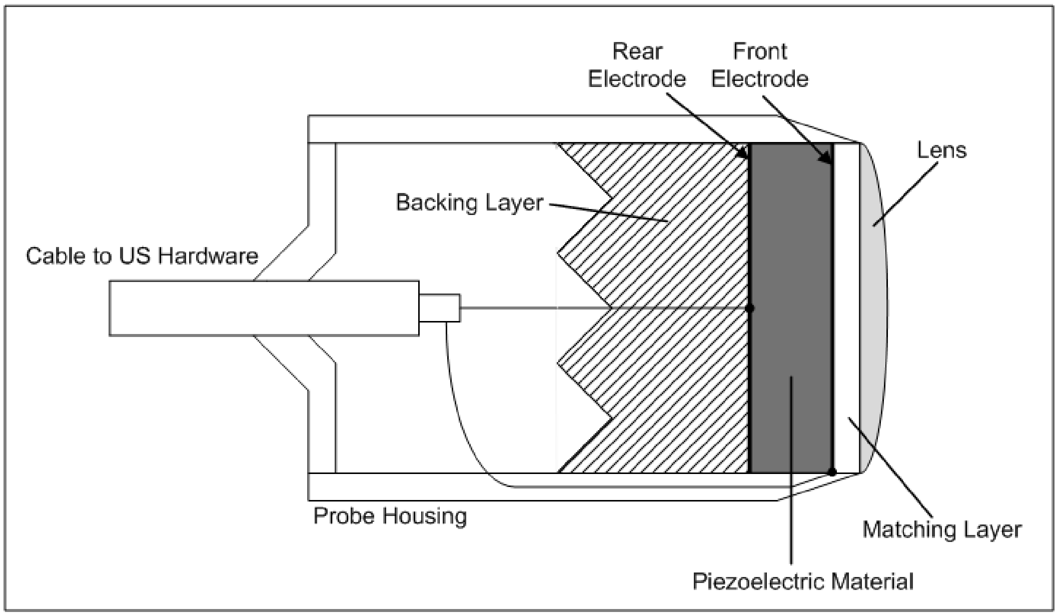

Figure 2.2 Basic ultrasound imaging probe. Based on [12], [14] and [15].

2.3.2 Ultrasound Physics

Ultrasound imaging as a technology is governed by the physics of sound propagation. The following section provides a basic outline of some of the more important concepts in order to convey a general understanding of how ultrasound works. The first important property is that of the speed of sound propagation. The speed of propagation of a sound wave is determined by the medium through which it is travelling [14]. This means that while travelling through tissue, the speed of sound propagation may vary. The following sub sections provide a brief outline of some physical properties of the interaction of ultrasound with tissue.

2.3.2.1 Attenuation

Attenuation is the weakening of sound as it propagates. Attenuation encompasses the absorption (conversion of sound to heat) of sound as it travels and the reflection and scattering of the sound as it encounters tissue interfaces and heterogeneous tissues. Attenuation is a limiting factor on imaging depth [16].

2.3.2.2 Acoustic Impedance

Impedance is the product of density multiplied by velocity and measures the resistance to sound passing though a medium [15]. As sound crosses an interface between two media, the impedance ratio between the two media determines how much of the incident sound wave is reflected back through the first medium [16]. If the acoustic impedance of one medium is the same as it is in another medium, sound will be readily transmitted from one medium to the other. However, a difference in acoustic impedance causes some portion of the sound to be reflected at the interface. It is primarily the change in acoustic impedance at a biological interface that allows visualization of soft tissue structures with an ultrasonic beam [15].

2.3.2.3 Reflection and Scattering

Ultrasound images are constructed from echoes which are generated by reflections of ultrasound waves at tissue boundaries and by scattering caused by small irregularities within the tissue. Reflections occur at tissue boundaries where there is a change in acoustic impedance as mentioned above. When an ultrasound wave travelling through one type of tissue encounters an interface with a tissue of differing acoustic impedance, some of its energy is reflected back towards the source of the wave, while the remainder is transmitted into the second tissue [14]. The proportions of the reflected and transmitted waves are based on the impedance differences between the media and an example of reflection can be seen in Figure 2.3 below.

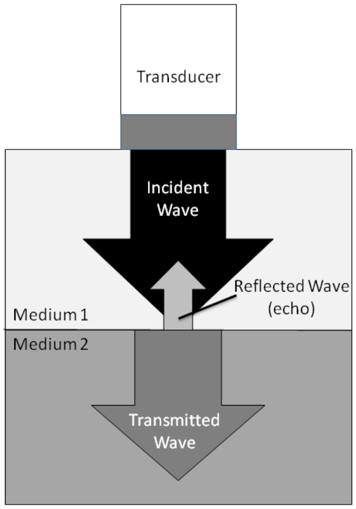

Figure 2.3 Reflection and transmission of a sound wave. The interface between the two media of differing acoustic impedances is perpendicular to the incident wave. Based on [16].

Reflection, as described above, occurs at relatively large interfaces where there is a change in acoustic impedance and is referred to as specular reflection. However, within human tissue and organs, there are many small scale variations in acoustic properties which constitute very small scale reflecting targets of size comparable to or less than the ultrasonic wavelength. Nonspecular reflections from these small targets are referred to as scattering which does not follow the same laws of reflection found at large interfaces [14]. Each small interface acts as a new separate sound source and sound is reflected in all directions independent of the direction of the incoming sound wave [15]. An interface of this size causing scattering is often referred to as a scatterer. (c) Figure 2.4 below demonstrates both specular and nonspecular reflection.

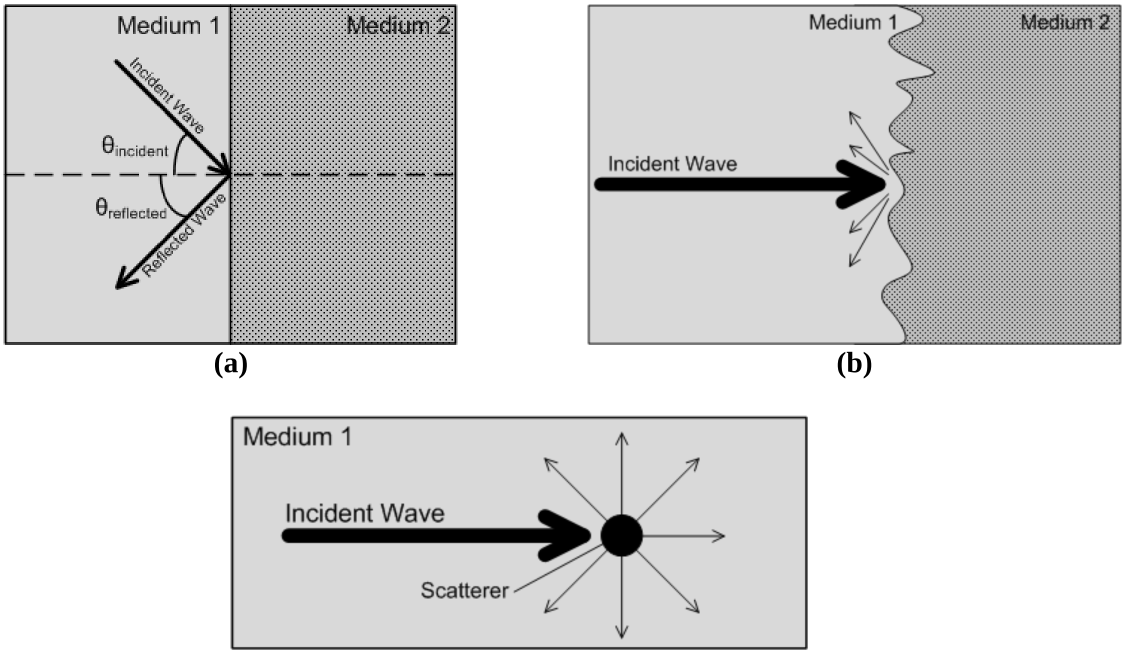

(a)

(b)

(c)

Figure 2.4 Types of ultrasonic reflection. The incident wave is reflected: (a) at a large, smooth interface resulting in equal incident and reflected angles, (b) at a large, rough interface resulting in reflected waves at a range of angles and (c) at a single scattering particle resulting in nonspecular reflection. Based on [14].

2.3.2.4 Speckle Echo

An ultrasound pulse, with its finite length and width, simultaneously encounters many scatterers at any location in its travel. Thus, several echoes are generated that can either interact constructively or destructively with each other. During scanning, the interference pattern can alternate from constructive to destructive which results in a displayed grainy appearance that does not directly represent scatterers but rather represents the interference pattern of the scatterer distribution scanned [16]. This phenomenon is called acoustic speckle and as such, echoes resulting from scatterers are often referred to as speckle echoes.

2.3.3 Imaging Modalities

Ultrasound imaging can be used for a number of different applications. All of these applications are ultimately based on similar principles having to do with the propagation of sound. However, it is how sound propagation is interpreted that sets apart differing applications. In order to provide the most useful tool to clinicians, a number of imaging modalities are currently used that have been tailored for specific purposes. The following section provides an outline of the most common A-mode, M-mode and B-mode ultrasound imaging modalities.

2.3.3.1 A-Mode

The A-mode or amplitude mode signal is generated from the envelope detected echo signal. In order to generate and display a succession of these signals, the transducer is excited on a repetitive basis [12]. The envelope or amplitude signals are then displayed on an oscilloscope or similar device. The time between successive transducer excitations is called the pulse repetition frequency (PRF). The PRF is chosen such that it is long enough to ensure that returning echoes have died out, but fast enough to be able to capture motion that may be of interest. The A-mode display is the simplest form of ultrasonic information and is currently used in only a few specialist applications [14]. An example of an A-mode scan can be seen below in Figure 2.5.

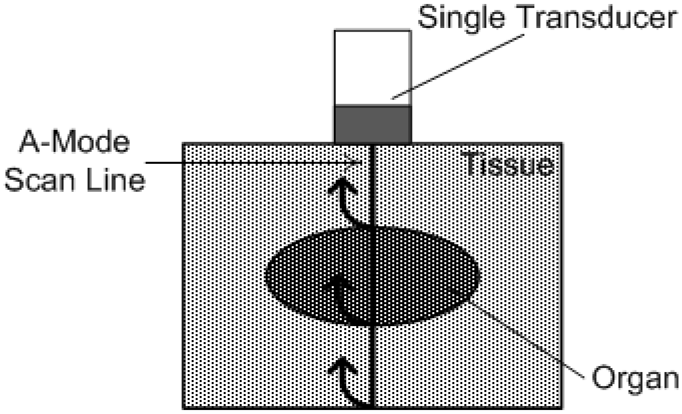

Figure 2.5 A-mode scan.

2.3.3.2 M-Mode

An M-mode scan is created by using each of the A-mode signals as a column in an image. In these cases, the value of the A-mode scan line becomes the brightness of the M-mode image. The scan lines are displayed in successive columns until the last column of the image has been reached at which point they wrap around to the first column of the image [12]. In M-mode imaging, the beam location remains fixed which provides a single, straight line of sight of any motion occurring in a direction towards or away from the transducer. For this reason, this modality is called motion mode which has been shortened to M-mode [14]. M-mode is useful for analyzing areas experiencing motion such as a heart valve.

2.3.3.3 B-Mode

B-mode or brightness mode images provide a two dimensional field of view that gives a cross sectional image of internal tissue. Traditionally, this was accomplished by moving the transducer laterally along the skin surface while collecting A-mode scan lines. More recently, however, array ultrasonic probes have been developed that contain a number of transducers which provide multiple A-mode scan lines. In either case, the obtained A-mode scan lines are collected and compiled to provide an image giving both lateral (perpendicular to beam direction) and axial (parallel to beam direction) information. A number of probes have been specifically designed for different B-mode applications resulting in a different number, size and orientation of transducers. However, the most common are the linear, curvilinear, trapezoidal, sector and radial probes [14]. An example of a B-mode scan can be seen below in Figure 2.6.

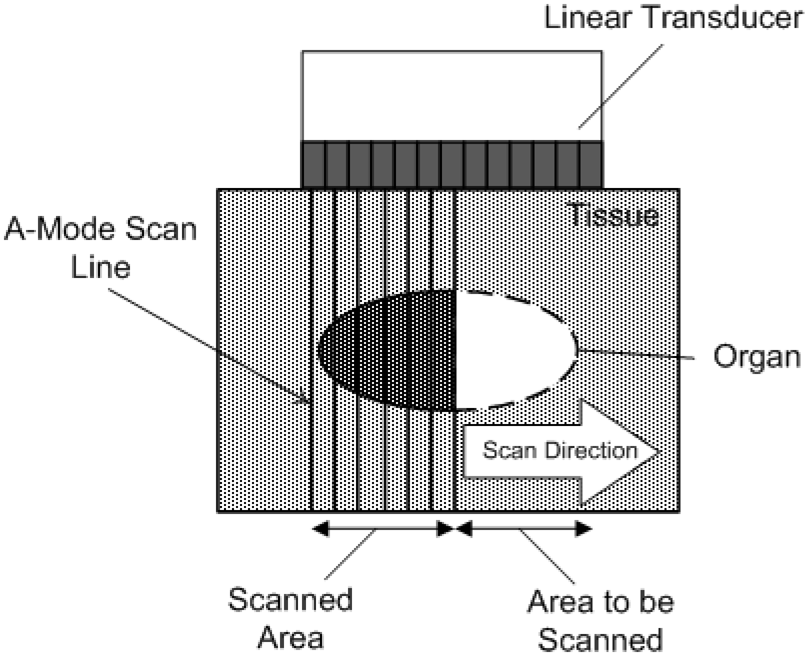

Figure 2.6 B-mode scan. Based on [14].

2.4 Current Methods of Studying Skeletal Muscle

Currently, there are a wide variety of techniques that are used to measure a number of different aspects of the musculature. Some of the more common techniques that are currently in use include electromyography (EMG) [17]-[24], mechanomyography (MMG) [25]-[31], magnetomyography [32], magnetic resonance imaging (MRI) [33], [34] and ultrasound imaging [35]-[55]. This wide range of techniques is used for a variety of different applications including the study of muscular disease [17], [23], [52], sports medicine [53], prosthesis control [19], [55], motion tracking [38]-[44], strain imaging [34], [45]-[48] and tissue characterization [45],[47]. The following section provides an outline of these techniques with a concentration on the details of ultrasound imaging as it applies to muscle measurements.

2.4.1 Electromyography

When a muscle contracts, a complex electrical signal commonly referred to as the myoelectric response, myoelectric signal or EMG is generated [22]. This signal can be recorded using conductive electrodes placed externally on the skin surface [17], [18] or internally with a needle electrode [23]. In the case or surface electrodes, the myoelectric signal results from the summation of the motor unit potentials produced in muscle tissue underlying the electrodes [22]. The signal recorded from a needle electrode can be a more discrete measurement due to the much smaller surface area of the electrode. In either case, as stated above, EMG measurements are based on the concept of measuring the electrical signal produced during muscle activation.

2.4.2 Mechanomyography

The mechanomyogram is a recording of the mechanical motion that is detectable over a contracting muscle [28]. Motion is detected by surface MMG techniques using optical distance sensors, accelerometers, piezoelectric contact sensors and microphones [29]. The most commonly used technique employs accelerometers [29] and examples of this method can be found in [27], [28]. Motion is measured with piezoelectric contact sensors by forcibly applying the sensor to the skin surface. When the tissue moves, the voltage output of the sensor changes and can be correlated to measure displacement. Microphones are used to measure the pressure waves produced by moving tissue [30]. In general, MMG provides an external or global representation of the total motion of the tissue under the area of the employed sensor.

2.4.3 Magnetomyography and MRI

Magnetomyography is a non-invasive technique to detect currents associated with action potentials in muscle which is immersed in a well conducting fluid [32]. This technique is less common than the other techniques mentioned and produces results similar to EMG as both techniques measure the electrical signals resulting from muscle activations. Muscles can be studied using MRI by observing the high resolution and detailed images obtainable with MRI technology [33] or by analyzing a time series of MRI images in a real-time fashion to produce estimations of quantities such as strain [34]. MRI is also less commonly used for muscle measurements which is most likely due to their cost and lack of portability.

2.4.4 Ultrasound

Ultrasound is a common medical imaging modality and its basic principles have been outlined above. As an imaging modality, ultrasound is applied to measure a variety of different quantities, but with respect to its use as a tool to study muscle, it is most commonly used to track muscle motion [38]-[44] and to measure strain [45]-[48]. These techniques are applied to a very wide range of applications as mentioned above. The following subsection outlines the current use of ultrasound for muscle measurements.

2.4.4.1 Measurements of Strain by Ultrasound

Strain provides an indication of relative deformation in such a way that stiff tissue shows less strain than softer tissue under identical applied forces. Strain measurements are important because research has found that pathological and physiological changes are often correlated with changes in tissue stiffness [44], [56]. Ultrasound provides a means to measure tissue strain non-invasively in a number of different ways including, most commonly, shear wave elastography [35], [47]-[48] and transient elastography [36], [45]-[46]. Shear wave elastography involves propagating mechanical shear wave interference patterns [47] through the tissue or object being imaged. Comparison of the relative frequency dependent changes between shear wave speed estimates can be used to estimate viscoelastic properties [35].

Transient elastographic or conventional ultrasonic strain estimation methods are based on estimating displacements between ultrasonic signals acquired before and after the application of stress [56]. The displacement estimations are then converted to estimations of strain. The basic principles involved in this type of elastography are fairly commonly used and were chosen as the method with which to obtain strain data for this thesis. This choice was made because strain data can be obtained with this methodology whenever a displacement has occurred and involves no external apparatuses such as a mechanical vibrator to produce shear waves for shear wave elastography. The specifics of the techniques used during research to calculated strain are further detailed in the following chapters.

2.4.4.2 Measurements of Muscle Motion by Ultrasound

Muscle motion can be measured and tracked with a number of different techniques using ultrasound including Doppler imaging [37], correlation [38]-[40], [44], [49]-[50], B-mode observations [41], [43], and peak or speckle tracking [42]. The two most commonly used methods seem to be peak or speckle tracking and correlation. Speckle tracking usually involves tracking a specific region of interest (ROI) as it moves with respect to time [42]. It is not uncommon to accomplish this tracking using correlation methods, but because only one specific ROI is defined and tracked, the term speckle or peak tracking is often used.

Correlation methods to measure muscle motion involve correlating two signals differing in time. The signals most often used are the received RF signal [38], [49] or the demodulated baseband signal [50], [56] and are explained in more detail in the following chapters. By correlating two signals from a pre and post compression state, displacement and therefore strain can be estimated. Using ultrasound to track in vivo muscle motion and velocity is a fairly new area of research, but some groups have been able to measure muscle contraction displacement and velocity in novel manners [38], [40]. The use of recently developed ultrafast ultrasound machines, with very high B-mode frame rates, has allowed Deffieux et al. [38] to develop a system able to track the propagation of muscle contraction after an electrical stimulation. Their work focuses on estimating displacement and velocity under forced electronic contraction of the bicep brachii muscle. Guo et al. [40] have shown the ability to produce superior results to EMG measurements when analyzing the Extensor carpi radialis muscle of the forearm during voluntary wrist extension.

2.4.5 Methodology Comparison

There is debate in literature over the best method to measure muscle signals such as comparing EMG to MMG [25], [26] and comparing ultrasonic techniques to EMG [24], [40]. Although these articles discuss superiorities as they relate to specific applications, the choice of overall optimal technology to use in any application is difficult to make. It is, however, possible to make some distinctions between these methods that can aid in understanding the overall advantages and disadvantages of each technology. MRI has very high spatial resolution, but is very expensive and not very portable. In contrast, EMG and MMG are both much more portable and are relatively inexpensive technologies. However, EMG signals can be very noisy and only represent a summation or average of the electrical signals occurring under the electrodes. MMG signals can be very accurate, but are also only able to provide a measurement of surface motion. Although ultrasound systems may be less portable or more expensive than EMG and MMG systems, they can provide both global and internal motion measurements with high spatial resolution.

Chapter 3:

Ultrasound Imaging System and Data Acquisition

The following chapter deals with the ultrasound imaging system used for this thesis. It provides hardware specifications and a description of the ultrasound signals the machine is capable of emitting. In addition, all of the data preprocessing necessary to obtain a useable signal for later analysis is also detailed. The chapter closes with a description of a designed GUI that provides a user with useful information about their data and allows them to quickly and intuitively access their data after preprocessing has occurred.

3.1 Ultrasound Hardware Specifications

A medical ultrasound imaging system (Model: Picus, ESAOTE Europe, Maastricht, Netherlands) was used for this thesis and was accompanied by an Asus digital signal processing computer running Windows XP. The computer ran ART.LAB which is software that was used to both view and store data. The Picus machine used can be seen in Figure 3.1 below.

Figure 3.1 Picus ultrasound hardware. Reproduced from [57].

3.1.1 Ultrasound Probe

The ultrasound probe used for our research contained a 40 mm linear array of transducers (Model: L10-5). The probe, seen below in Figure 3.2, is made up of four major layers and contains 127 individual transducers separated by 315 µm. The first layer contains the transducers made up of piezoelectric crystals having a thickness of 188 µm. The next two layers are impedance matching layers used to optimize the transfer of ultrasound waves into and out of biological tissue. The first matching layer has a thickness of 65 µm and an ultrasound propagation velocity of 2290 m/s. The second matching layer has a thickness of 85 µm and an ultrasound propagation velocity of 2750 m/s. The final layer is an acoustic lens which is used to focus ultrasound waves into the desired medium. It has a thickness of 1010 µm and an ultrasound propagation velocity of 975 m/s [58].

Figure 3.2 L10-5 40 mm linear array ultrasonic probe. Reproduced from [59].

3.1.2 Ultrasound Signal Specifications and Operation

The ultrasound system samples the received waveform every 0.03 µs. The center frequency of the emitted ultrasound waves can be varied from 2.7-12.5 MHz [57]. The system has three major imaging modalities: M-mode, B-mode and Fast-B mode. The number of scan lines used varies based on the acquisition mode. An M-mode frame contains 37 single scan lines. Since M-mode obtains only a single line from a single location, an M-mode frame is merely a method used to more easily store data. A B-mode frame contains 127 scan lines from all 127 transducers in the linear array probe. Finally, a Fast-B mode frame contains eight 14 line Fast-B mode images. Eight Fast-B images are packed into a single frame for storage purposes.

The pulse repetition frequency (PRF) varies based on the imaging modality and is analogous to the frame observation rate. The frame observation rate or frame rate is not related to the data storage concept of frames as mentioned in the preceding paragraph above. The frame rate is equal to the repetition rate of a signal from a single specific transducer known as a line of sight. For the remainder of this thesis, a frame will be defined as follows: M-mode frames contain one scan line, Fast-B mode frames contain 14 scan lines and B-mode frames contain 127 scan lines. While operating in M-mode, the maximum frame rate is 980 Hz. In B-mode, a frame rate of up to 30 Hz is achievable and Fast-B mode has a maximum frame rate of 687 Hz.

In M-mode, a single scan line over time is captured. In B-mode, 127 scan lines are obtained for every temporal sample. Each scan line is separated by 315 µm which results in a total lateral coverage of 39.69 mm. In Fast-B mode, 14 lines of sight are used with a separation of 1260 µm resulting in a total lateral coverage of 16.38 mm. In B-mode and M-mode axial signal acquisition is possible for a total of about 35 mm in depth whereas in Fast-B mode only about 30 mm in depth are acquired. These values can vary based on the ultrasonic propagation velocity through the material(s) being measured. Temporally, signal acquisition of the system allows for the continuous capture of about 5.66 seconds of data.

3.1.3 Analog to Digital Converter

The received ultrasound signals are sampled with an analog to digital converter (ADC) that has 16 bits including a 4 bit offset. This results in a 12 bit recorded RF signal with a dynamic range of 72 dB [58]. The data is stored in a four bit shifted or signed 16 bit format. The resultant amplitude of the received RF signal has a range of values from -32768 to 32752 with a step size of 16 due to the 4 bits of offset. Therefore, although there are 16 bits in total, the analog to digital converter may be thought of as having 12 bits for numerical representation because of the 4 offset bits. All signal processing within the

Picus system is done in the digital domain. Signals are converted to analog in order to transfer the data from the scanner to the digital signal processing computer where they are again converted back to digital for processing and storing with ART.LAB.

3.2 Data Preprocessing

The ultrasound system used allowed access to any recorded digitized RF ultrasound signal. This data was stored using ART.LAB in a '.zrf' file format. This format was created by Esaote and allowed for signal analysis with Matlab using a function called 'readzrf.m' that was included with the ultrasound hardware. Although it was very convenient to have access to this digital information, it was still necessary to preprocess this data before any real results could be obtained. The following section contains information about the methods used to properly format the raw data to allow for accurate analysis of the desired signals.

3.2.1 Raw Data Format and Header Removal

All data were stored using ART.LAB with a custom file format developed by Esaote in a file having a '.zrf' extension. The file is formatted as follows: File header, Signal processing settings, Login information, Z-data matrix, RF-data matrix and Checksum. The file header includes information about the file type, version, trigger and size. The signal processing settings contain information about how the data in the file were collected. This includes such information as machine software settings, ROI and information about various options unique to an ART.LAB application which were not all used to achieve the goals of this thesis. The login information contains details about the patient the data were collected on such as name, weight, blood pressure, etc. This header was not used because all information of this nature was recorded manually when necessary. The data in the file header, signal processing settings and login information were therefore allowed to be automatically removed by a supplied Matlab function.

The Z-data and RF-data matrices were the storage areas for the recorded data. Both are similar in that they contain 16 sample points of header information. This information was stripped away during data preprocessing and stored as useful information. These headers contained information pertaining to the size of the file, file type, format and some information about the acquisition of the data. The RF-data matrix contained 1516 sample points after its header was stripped away. Each point is a sample from the ADC of the raw RF ultrasound waveform. The total number of points in a file is a result of both sampling rate and the captured depth region as discussed above. The Z-data matrix contained 758 sample points and represents the envelope of the RF ultrasound waveforms. The total number of points in the Z-data matrix is always equal to one half that found in the RF-data matrix. Finally, the checksum contained error checking that was automatically handled by the supplied Matlab function.

3.2.2 Lens Echo Removal

As mentioned above, there are several layers between the ultrasonic transducers and the physical surface of the ultrasonic probe that account for a certain time delay. This time delay results from ultrasound propagation inside the acoustic lens and the two impedance matching layers. Using the thickness and ultrasound propagation velocities within these materials as provided above, the time delay within each of these materials can be calculated. It was determined that the total round trip time delay within the matching layers and the lens corresponded to about 4 axial and 69 axial sample points, respectively. This resulted in a total time delay of 73 axial sample points within the probe. The time delay and potentially the echoes from within the probe will be experienced by all received RF signals and for the remainder of this document will be termed the lens echo. Due to the fact that this signal comes from within the ultrasonic probe itself, the time delay period of the lens echo was removed before any data processing was performed.

An envelope signal was obtained without placing the probe on a specimen resulting in an interface between the lens surface and air. This envelope was used to determine the time delay period of the lens echo as shown in Figure 3.3. Ultrasound will not propagate into air because of the impedance mismatch at the lens-air interface. Rather, the ultrasound waves will be totally reflected back into the probe where they are detected by the transducers. To further increase the observed effect of the echoes from within the lens, the amplifier gain of the system was maximized during signal acquisition. By finding the location of the first echo from the lens-air interface, it was experimentally determined that 69 sample points made up the time delay from within the lens. This value agrees with the calculated value of 73 sample points discussed above and as such, 69 points were removed from the beginning of every scan line during preprocessing in order to negate the lens echo and its time delay.

It should be noted that the experiment to obtain the results shown in Figure 3.3 was specifically designed to observe clear echoes from within the lens. In practice, ultrasonic couplant gel is used to match the impedance of the probe with the impedance of the object being imaged and therefore the reflection from the lens along with its multiple echoes should not be observed.

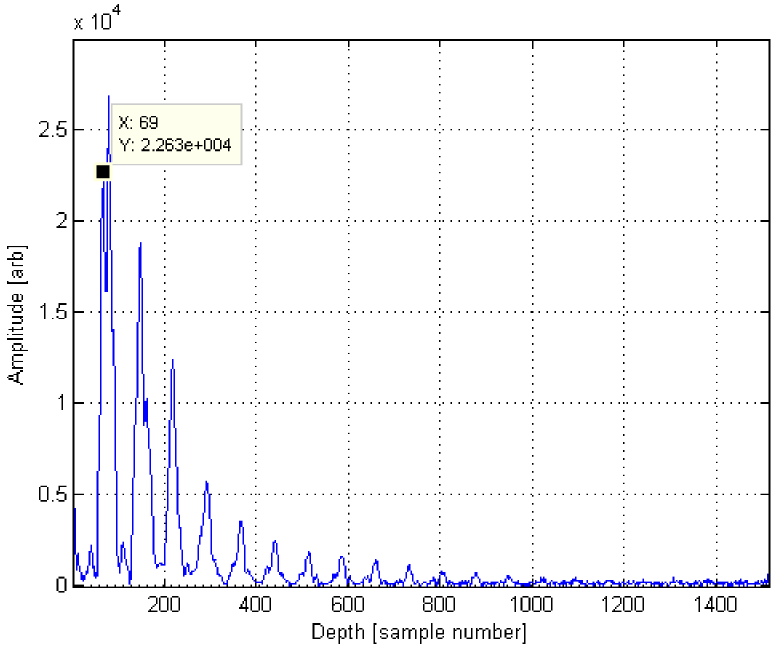

Figure 3.3 Envelope of RF scan line used to determine effect of lens echo. The first echo from the lens boundary has been marked and was used to calculate the time delay resulting from the lens echo.

3.2.3 Temporal Reorganization

Temporal reorganization deals with the way a file is stored during data acquisition. There is a circular buffer that contains about six seconds of data at any given time. When data are stored by selecting the storage option on the machine, the circular buffer is dumped exactly as it is into a file. This often results in a signal that is out of order with respect to time. It was therefore necessary to correct this order during data preprocessing. An example of this phenomenon called time wrapping can be seen in Figure 3.4 below.

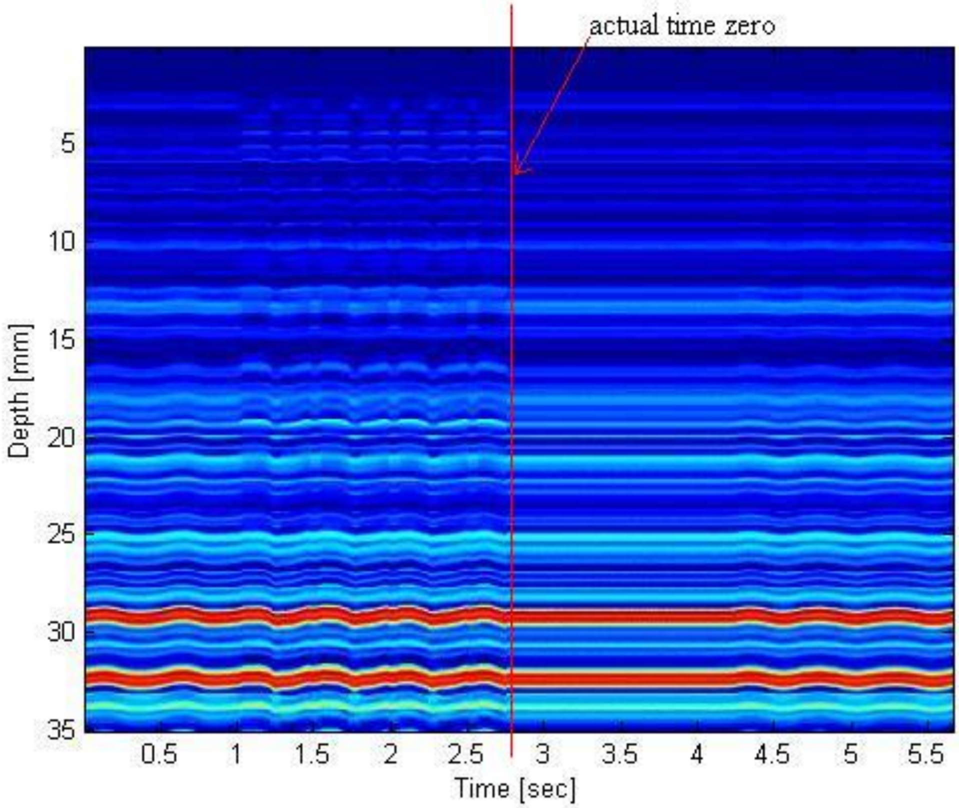

Figure 3.4 M-Mode image before temporal reorganization. The arrow points to the true beginning of the sequence.

This problem was fixed by locating time t_0, when the data began being captured, by analyzing the frame counter located in the header of the Z-data matrix. Specifically, this was done by locating the transition in the frame counter. An example of the frame counter with the transition marked can be seen below in Figure 3.5. The first scan line after the transition represents the first recorded scan line at time t_0. All data were then reorganized in time using the determined t_0 as the reference starting time. A final example of an RF waveform after all of the aforementioned preprocessing had been done can be seen below in Figure 3.6.

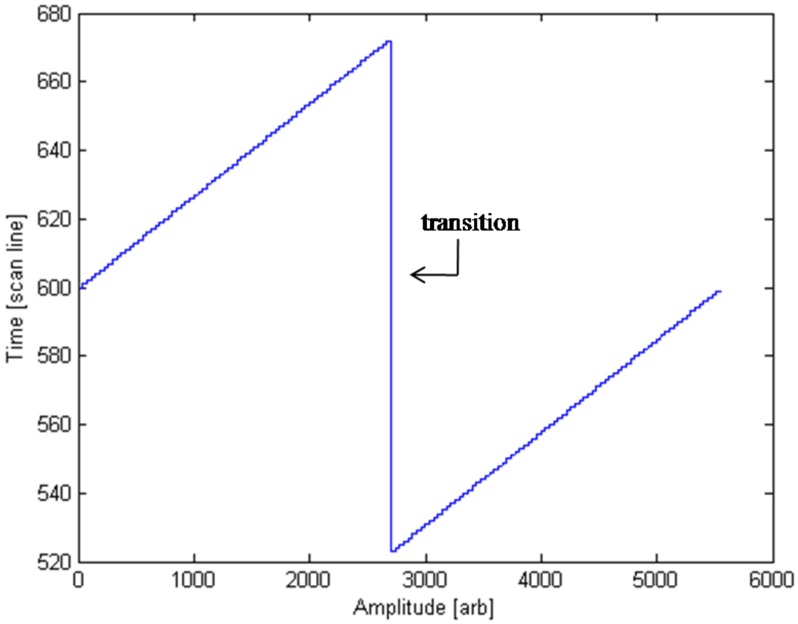

Figure 3.5 Frame counter from the Z-data matrix header. This counter shows the transition used for temporal reorganization.

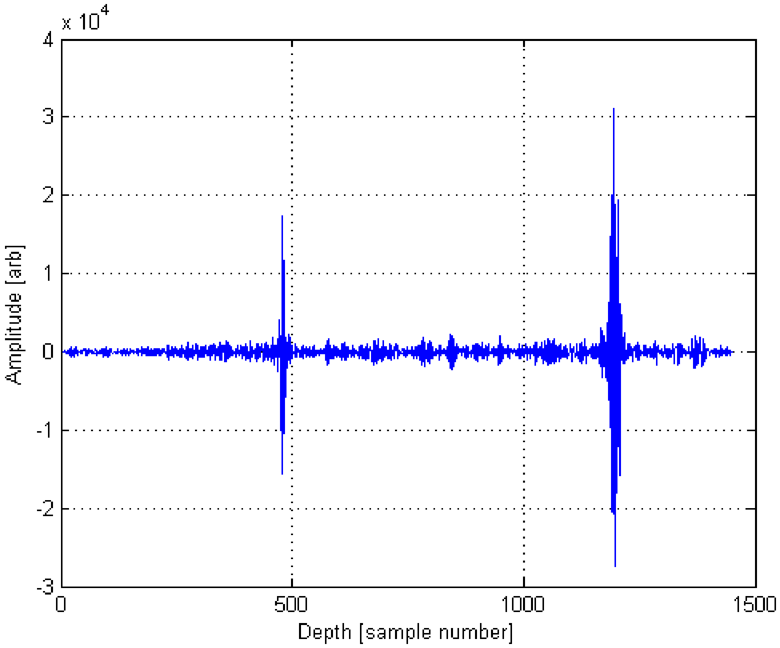

Figure 3.6 Raw ultrasonic signal obtained after applications of all data preprocessing. This particular waveform is from a set of M-mode measurements taken of a multiple layer phantom. The details of the phantom are discussed in Chapter 6.

3.3 GUI Development

A graphical user interface (GUI) was designed in order to simplify the process necessary to view acquired data. Even after the data preprocessing mentioned above is done, there are still a number of steps required to view data. For instance, a number of calculations need to be done in order to locate a specific scan line in a specific frame of a specific type of data. These calculations are necessary because of the way in which data are stored. In addition, header information that a user may want to know is not always in an intuitive location. For this reason, the GUI was developed to allow any user easy access to their recorded data and to some important information about it.

The GUI works by allowing a user to browse for any '.zrf' file that they wish to view. The GUI will then open and display the first RF scan line after all of the necessary preprocessing has been completed. In addition, it will display an envelope image, the imaging modality of the file as well as the total number of frames and scan lines present in the file. There are three modalities to consider. They are M-mode, B-mode and Fast-B mode as described above. Due to the fact that each file format has a different frame organization, the GUI must process each type in its own unique way. In addition, the GUI allows a user to select and view any frame and scan line they want using a track bar or input window. A screen shot of the GUI is shown in Figure 3.7 below.

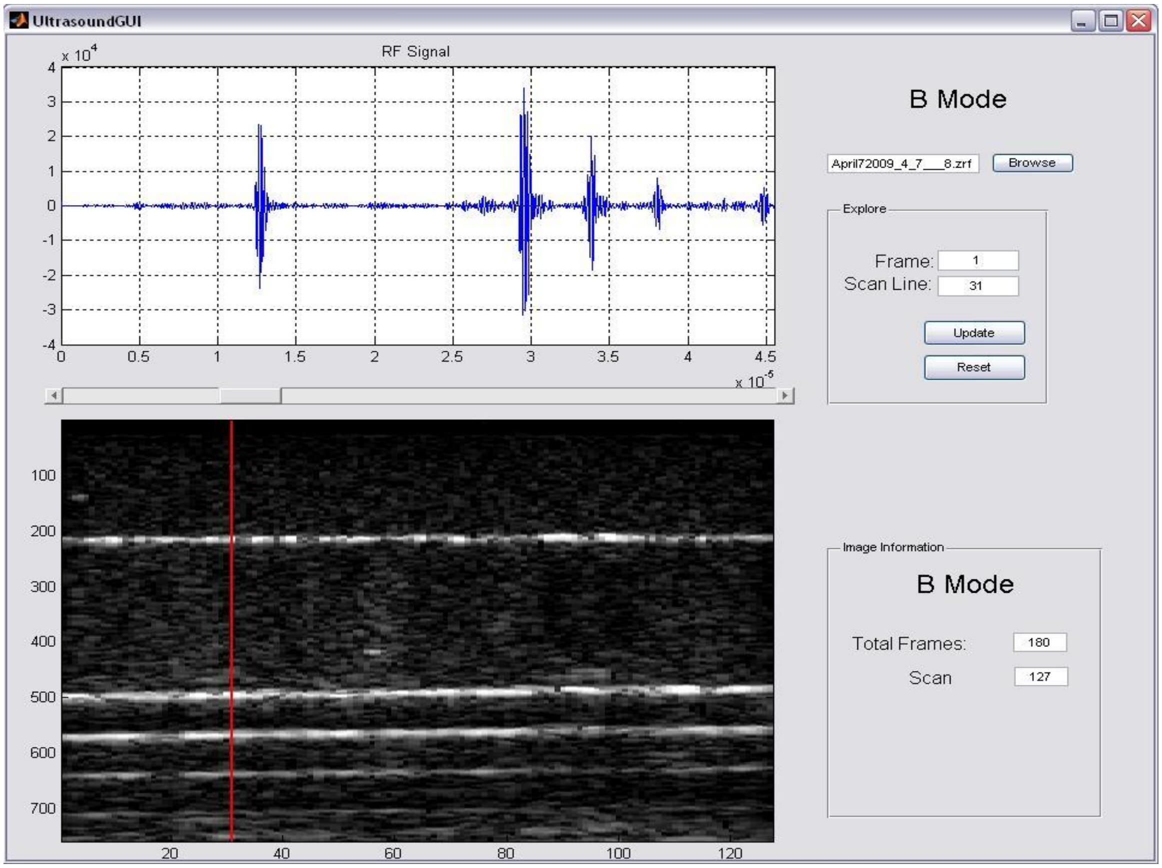

April72009_4_7___8.zrf

Frame: 1
Scan Line: 31

Total Frames: 180
Scan 127

Figure 3.7 Screenshot of GUI. The red line in the B-mode image indicates the location of the currently viewed scan line.

Chapter 4:

Mathematical Model and Data Processing

Data processing has to do with all of the steps involved in taking a signal from its raw form to a desired result. In the case of this thesis, raw data are considered to be the received digital ultrasonic waveform as obtained after all preprocessing steps described in Chapter 3 have been completed. These signals are processed in order to obtain estimates of tissue displacement, motion velocity and strain. The following chapter outlines the mathematical model of our imaging environment as well as a mathematical description of the frequency modulation (FM) analogy, quadrature demodulation, displacement estimation and strain estimation techniques used during data processing. In addition, an accuracy evaluation of the data processing procedure is discussed.

4.1 Mathematical Model

The data processing steps as well as the procedures used throughout the remainder of this thesis all relate to a specific imaging environment or mathematical model. We describe this model in terms of the coordinate system used and the effects that using this system has on acquiring measurements. The coordinate system defines all motion measured with the ultrasound system to be relative to the surface of the ultrasonic probe. The frame of reference is then referred to as the ultrasonic probe reference frame and motion observed with respect to this coordinate system differs from what an experimenter with a global frame of reference would observe. Figure 4.1 and Figure 4.2 below demonstrate the differences between identical probe motions as observed with respect to the two differing global and ultrasound probe frames of reference.

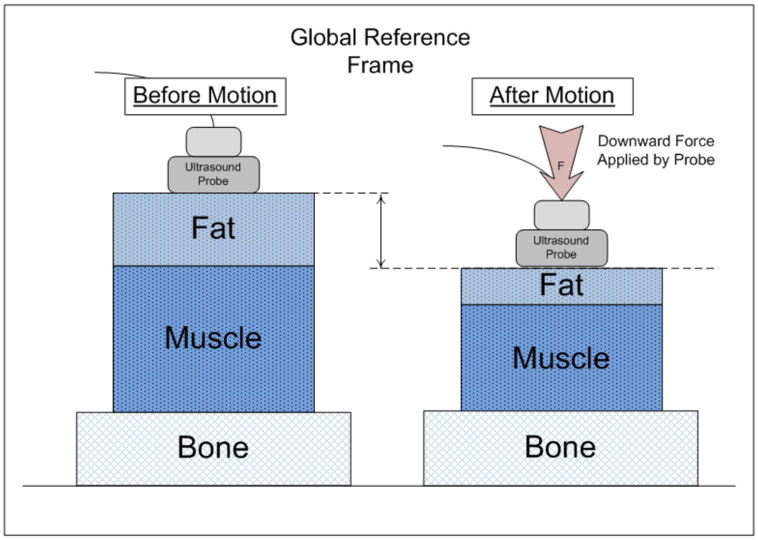

Figure 4.1 Probe motion as observed with respect to a global reference frame.

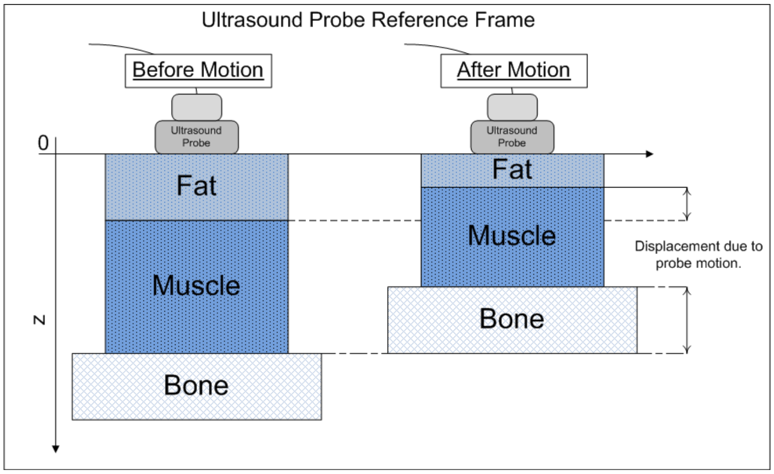

Figure 4.2 Probe motion as observed from the ultrasound probe reference frame.

The case of the reference frame being at the probe surface results in the fact that observed displacement will increase with respect to depth. Specifically, it was assumed that for any constant externally applied force at the surface of the probe, the magnitude of the displacement observed would increase linearly with respect to depth. This implies that the stress-strain properties of all materials under consideration are linear. A positive displacement is defined as motion in a direction away from the probe whereas a negative displacement denotes a displacement in a direction towards the probe.

Once the frame of reference had been established, variables and conventions were defined that would be used for mathematical definitions and description. A list of the variables used can be found in the Nomenclature section found above. To begin with, a distinction is made between the conventions of fast and slow time. When dealing with ultrasonic signals, all information is directly related to some amount of time. Time, however, is used to represent two different quantities with respect to the axial (depth) and temporal directions often referred to as fast and slow time respectively [60], [61].

The convention established for this thesis was to denote fast time with a t and to represent slow time with a T. Fast and slow time, as well as the different sampling conventions of M-mode and B-mode, are shown in Figure 4.3 and Figure 4.4 below in which the variables m, n and i represent temporal, axial and lateral samples respectively. Fast time has to do with time as it relates to depth or axial samples of a received ultrasound waveform. Slow time refers to the time between transmitted pulses from a transducer and is analogous to the pulse repetition frequency, frame rate or temporal sampling rate of the ultrasonic system depending on the imaging modality.

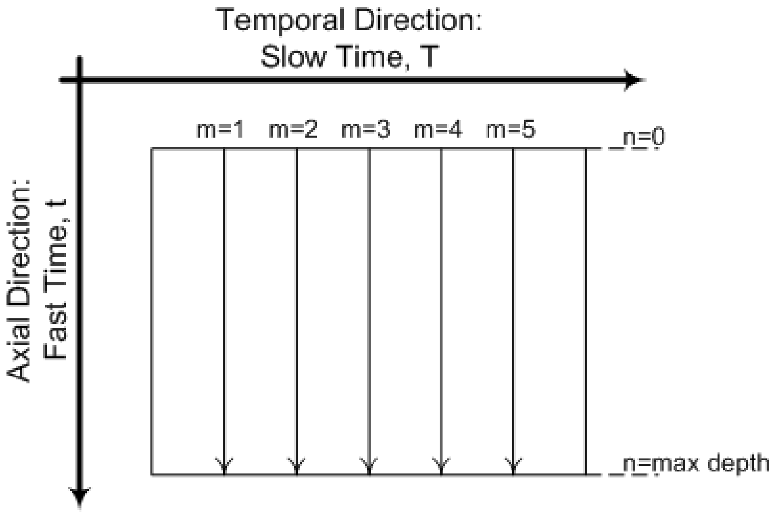

Figure 4.3 M-mode sampling structure. During M-mode, temporal samples, m, are equivalent to scan lines and represent the pulse repetition frequency. Axial samples, n, represent depth.

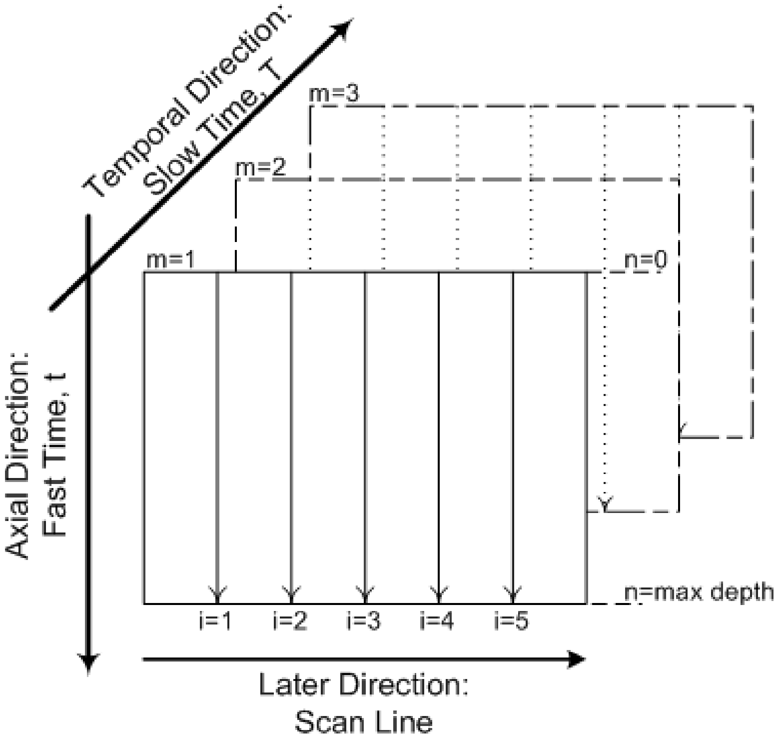

Figure 4.4 B-mode sampling structure. During B-mode, temporal samples, m, are equivalent to image frame number. Scan line number, i, corresponds to samples in the lateral direction. Axial samples, n, represent depth.

4.2 Frequency Modulation

There are two mechanisms that affect the received ultrasound signal. The first is that of the classical Doppler shift where, because of the relative velocities of the ultrasound source and target, each received pulse is expanded or contracted with respect to the transmitted pulse which changes the frequency of the received pulse. The second is due to the targets in a sample volume moving either toward or away from the probe, causing consecutive received pulses to experience a time shift with respect to the time of transmission. This time shift results in a change in the phase relationship between the ultrasound signal and the master oscillator of the ultrasound machine.

It is this shift in phase that is of interest for our research. The change in phase results in a detected frequency shift that is virtually identical to the shift caused by the Doppler effect and any difference can be ignored for most practical purposes [62]. Therefore, the basic Doppler equation, Eq. 4.3, applies equally to the frequency shift due to particle motion as it does to the shift caused by the Doppler effect.

The phase shift of concern to our research is caused by target motion. As such, measurements of phase shift can be obtained and converted to represent the characteristics of the target motion such as displacement and velocity. This section describes the concept that a received ultrasonic signal can be represented as a pure-tone frequency modulated (FM) process [63], [64]. Based on this FM representation, phase information can be obtained by demodulating the received ultrasound signal. The following section details the description of a single received ultrasonic signal as an FM process [63]-[67]. The transmitted signal is assumed to be represented by [63]

$$s_t(t) = cos(w_c t) \tag{4.1}$$

where *t* is fast time, or the time after pulse transmission and ω_c is the ultrasonic center frequency, which can be thought of as the FM carrier frequency. The signal representing the motion of the scatterers can be thought of as the message of the FM signal. The displacement of the motion is represented by $d(t)$ and the velocity is denoted by the first derivate of the displacement as $\nu(t) = \dot{d}(t)$. The received ultrasound signal can be written as [64], [67]

$$s_r(t) = A(t)cos\left(\int_{-\infty}^{t} \omega_i(t)dt\right) \tag{4.2}$$

where $A(t)$ is the received amplitude, $\omega_i(t) = \omega_c + \omega_d(t)$ is the instantaneous frequency and $\omega_d(t)$ is the Doppler shift frequency due to the motion of the target. The Doppler shift frequency can be expressed as [12], [68]

$$\omega_d(t) = \frac{2\nu(t)cos\theta}{c}\omega_c \tag{4.3}$$

where θ is the angle between the vibration direction and the direction of ultrasound wave propagation and c is the ultrasound propagation speed. Substitution of Eq. 4.3 into the equation for $\omega_i(t)$ can be written as

$$\omega_i(t) = \omega_c - \frac{2\omega_c\nu(t)}{c}\cos\theta \tag{4.4}$$

which is then itself substituted into Eq. 4.2. The result is a pure-tone FM equation for the received signal as

$$s_r(t) = A(t)cos\left[\omega_c t + \phi(t)\right] \tag{4.5}$$

where $\phi(t)$ is the resultant phase shift signal due to particle motion and is the desired message signal for this research. The displacement of a target particle is related to and can be calculated from this phase shift by Eq. 4.14. Received ultrasound signals are often referred to as radio-frequency (RF) signals due to the FM analogy and their high frequency.

4.3 Quadrature Demodulation

A received ultrasound signal can be represented by a pure-tone FM signal. Using such a convention, the motion of the ultrasonic scatterers represented by a shift in phase is analogous to the message of a received ultrasonic signal. The frequency of the received signal has been modulated by the center frequency of the ultrasonic wave which can be thought of as the carrier frequency of an FM signal. The phase varying message and therefore the particle motion can be removed from the FM signal by demodulation [69].

As stated above, the motion of a target induces a phase shift in the ultrasonic signal. It is this shift in phase that is of interest in this research as it can be converted to a measure of displacement. Therefore, the process of quadrature demodulation [71]-[83] was used throughout this research to recover a shift in phase. The following section details the description of the demodulation procedure applied to a single received ultrasonic signal represented by

$$s_r(n) = A(n)cos(\omega_c(n) \cdot nT_s + \phi(n)) \tag{4.6}$$

where n and T_s denote the axial depth sample number and axial sampling period respectively [71]. The phase shift is represented by $\phi(n)$ and the received amplitude is denoted by $A(n)$. During demodulation, the received RF signal is multiplied by a reference sinusoid described by

$$S_{ref} = e^{-j\omega_{dem} nT_s} \tag{4.7}$$

where ω_{dem} is the demodulation frequency. The quadrature demodulation process can then be described by

$$\begin{aligned} I(n) &= LPF\{s_r(n) \cdot \cos(\omega_{dem} nT_s)\} \\ &= LPF\Big\{\frac{A(n)}{2}\cos\big[(\omega_c(n) - \omega_{dem})nT_s + \phi(n)\big] + \frac{A(n)}{2}\cos\big[(\omega_c(n) + \omega_{dem})nT_s + \phi(n)\big]\Big\} \\ &= \frac{1}{2}A(n)\cos\left[\Delta\omega(n) \cdot nT_s + \phi_n(n)\right] \end{aligned} \tag{4.8}$$

$$\begin{aligned} Q(n) &= LPF\{s_r(n) \cdot [-\sin(\omega_{dem} nT_s)]\} \\ &= LPF\Big\{-\frac{A(n)}{2}\sin\big[(\omega_c(n) + \omega_{dem})nT_s + \phi(n)\big] + \frac{A(n)}{2}\sin\big[(\omega_c(n) - \omega_{dem})nT_s + \phi(n)\big]\Big\} \\ &= \frac{1}{2}A(n)\sin\left[\Delta\omega(n) \cdot nT_s + \phi_n(n)\right] \end{aligned} \tag{4.9}$$

where $I(n)$ and $Q(n)$ respectively denote the in-phase and quadrature signals, LPF denotes low pass filtering and $\Delta\omega(n) = \omega_c(n) - \omega_{dem}$ is the down shift of the received ultrasound frequency. The complex baseband signal can then be represented by

$$u(n) = I(n) + jQ(n) \tag{4.10}$$

and the message or phase information can be obtained by

$$\angle u(n) = \Delta\omega(n) \cdot nT_s + \phi(n) \tag{4.11}$$

where $\angle$ denotes phase angle. The addition of depth variability to ω_c as $\omega_c(n)$ is an important concept. It demonstrates how the center frequency of the received RF signal can vary with respect to depth. This variation is usually due to depth and frequency dependent attenuation [77]. Therefore, it can be seen from Eq. 4.11 that $\Delta\omega(n)$ is a source of error in the phase estimation. Specifically, accurate phase estimation requires an accurate estimation of ω_{dem} such that it is as close to $\omega_c(n)$ at any depth as possible.

4.4 Displacement Estimation

Once the complex baseband signal has been obtained, an estimation of displacement can be made using an autocorrelation method [77]-[83]. In order to exactly explain the procedure used, the aforementioned derivations are extended to include both the axial and temporal directions. In this way, the RF ultrasound signal received after transmitting an ultrasonic pulse can be represented by $s_{r_z}(n,m)$, where z is the ultrasonic beam direction, n is the axial or depth sample number and m is the pulse number of a specific transducer, scan line or frame number depending on the imaging modality. The variable m always represents the sample number in the temporal or slow time direction.

Aside from the spatial inconsistency of the RF center frequency, the center frequency also varies temporally with slow time because of the change in time frames. For this reason, the received ultrasonic center frequency is described dependent on both the axial and temporal directions by $\omega_c(n,m) = 2\pi f_c(n,m)$. The complex baseband signal $u_z(n,m)$ is then obtained by quadrature demodulation of the RF signal as explained above and summarized by

$$u_z(n,m) = LPF\left\{s_{r_z}(n,m)e^{-j2\pi f_{dem} n T_s}\right\} \tag{4.12}$$

where $f_{dem} = \frac{1}{2\pi}\omega_{dem}$. The two-dimensional correlation function is then defined as [81]

$$r_{n,m}(N,M) \equiv u_z(n,m) \cdot u_z^*\ (n+N, m+M) \tag{4.13}$$

where * represents the complex conjugate and $r_{n,m}(N,M)$ defines the complex autocorrelation function with lags N and M, in the axial and temporal directions, respectively.

4.4.1 Phase-Sensitive Method

Displacement in the direction of ultrasound propagation can be calculated in the conventional phase-sensitive method using the estimated phase shift between two consecutive frames represented by $\Delta\phi_z(n,m) = \angle r_{n,m}(0,1)$. The instantaneous displacement $\Delta d_z(n,m)$ between two consecutive frames is then calculated as follows [80]

$$\Delta d_z(n,m) = \frac{c\Delta\phi_z(n,m)}{4\pi f_c(n,m)} \approx \frac{c\Delta\phi_z(n,m)}{4\pi f_{dem}(n,m)} = \frac{c}{4\pi f_{dem}(n,m)}\angle r_{n,m}(0,1). \tag{4.14}$$

In Eq. 4.14, knowledge of the center frequency $f_c(n,m)$ is needed in order to obtain an accurate instantaneous displacement estimate. However, because it is unknown, in conventional phase sensitive methods the frequency of the reference sinusoid, f_{dem}, is used as the frequency term in the denominator of Eq. 4.14. Ideally, it should be the actual center frequency $f_c(n,m)$ that is used. This method makes the assumption that $\omega_c(n,m) = \omega_{dem}$ which causes the reduction of Eq. 4.11 to $\angle u(n,m) = \phi(n,m)$. The accumulated displacement $d_z(n,m)$ is then obtained by accumulating the estimated instantaneous displacement $\Delta d_z(n,m)$ between two consecutive frames as follows

$$d_z(n,m+1) = d_z(n,m) + \Delta d_z(n,m), \qquad \text{where } d_z(n,0) = 0. \tag{4.15}$$

This method of estimating displacement can also be referred to as the 1D autocorrelation method because only the autocorrelation function with respect to the temporal direction is utilized.

4.4.2 Two Dimensional Autocorrelation Method

The use of f_{dem} in place of $f_c(n,m)$ in Eq. 4.14 often induces error as the demodulation frequency rarely matches the true center frequency. To compensate for this error, the mean center frequency, $\bar{f}_c(n,m)$ can be estimated as in the method described by [77], [82] as

$$\bar{f}_c(n,m) = f_{dem} - \frac{\angle r_{n,m}(1,0)}{2\pi T_s} . \qquad (4.16)$$

It is this mean center frequency that is used in Eq. 4.14 instead of the demodulation frequency in order to obtain an unbiased estimate of the instantaneous displacement between two consecutive frames as follows

$$\Delta d_z(n,m) = \frac{c}{4\pi \bar{f}_c(n,m)} \angle r_{n,m}(0,1) . \qquad (4.17)$$

This instantaneous displacement is then substituted into Eq. 4.15 in order to obtain the accumulated displacement. This method is similar to the phase-sensitive method in that it uses temporal direction autocorrelation $r_{n,m}(0,1)$, but it also estimates the local variations in center frequency with the axial direction autocorrelation $r_{n,m}(1,0)$ present on the left side of Eq. 4.16. It is for this reason that this method is referred to as the two dimensional (2D) autocorrelation method and was the method used to estimate displacement in this research. Velocity estimates were obtained by taking the first derivative of the accumulated displacement.

4.4.3 Displacement Estimation Limitation

Although the method used to estimate displacement can be very accurate, it does have one major limitation. This is the fact that the displacement is estimated based on a phase shift occurring between two consecutive temporal samples. As a result, a shift in phase of more than 2π radians between consecutive temporal samples cannot be accurately detected. Rather, such a large shift in phase will be measured as if it was within the range from 0 to 2π radians. This measurement will not take into account the phase shift from possible integer multiples of 2π radians that may have occurred. This fact places the stipulation that no motion measured should cause a phase shift greater than 2π radians between two consecutive temporal samples. An experimental procedure has been developed to allow post-acquisition verification that such a phase variation of 2π radians between two consecutive temporal samples has not occurred.

4.5 Strain Estimation

As mentioned in Chapter 2, strain or relative deformation is a measure of the relative displacement of a region of an object in comparison to the displacement of neighbouring regions. It is defined as the deformation of an object, relative to its original shape [84]. Axial strain ε is given by the spatial gradient of the axial displacement d in the axial direction z as [85]

$$\varepsilon = \frac{\delta d}{\delta z}. \tag{4.18}$$

Ultrasound elastography aims to provide tissue stiffness information non-invasively which can be accomplished in a number of different ways. However, one method commonly found in literature, has been adopted for this research and is based on estimating the strain on an object caused by its compression [84]-[90]. The source of this compression is the application of stress which can either be applied externally by the ultrasound probe or internally due, in the case of skeletal muscle imaging, to muscle contraction. Strain indicates the amount of deformation and stiff tissue shows less strain than softer tissue under equally applied forces [56]. Strain is a relative quantity and as such is represented throughout this thesis as a positive percentage.

For our research purposes, strain was estimated based on the accumulated displacement of a specific frame analyzed over depth. The accumulated displacement provides a profile of displacement as it varies with respect to depth in the axial direction. Therefore, an estimation of the slope of the accumulated displacement over depth within an axial region from points a to b, defined by $n_{ab} = [a, b]$, is equivalent to the axial strain in that region as

$$\varepsilon_z(n_{ab}, m) = \frac{\Delta L_{ab}}{L_{ab}} = \left| \frac{d_z(a,m) - d_z(b,m)}{a-b} \right| \tag{4.19}$$

where L_{ab} is the original distance between points a and b and ΔL_{ab} is the resultant distance between them as caused by the displacement of the points by $d_z(a,m)$ and $d_z(b,m)$ after the application of stress and as estimated by Eq. 4.15. Pre-stress and post-stress states can be seen in Figure 4.5 below with the region n_{ab} defined from points a to b which are located at the interface boundaries. The location of points a and b are shown at the interface boundaries for simplicity, but can actually be located anywhere within the area being imaged. A strain image can be created by displaying the estimated strain for all regions within an object. In this way, the resolution of the strain image or an object's measured strain distribution is directly related to the size of the selected region, n_{ab}.

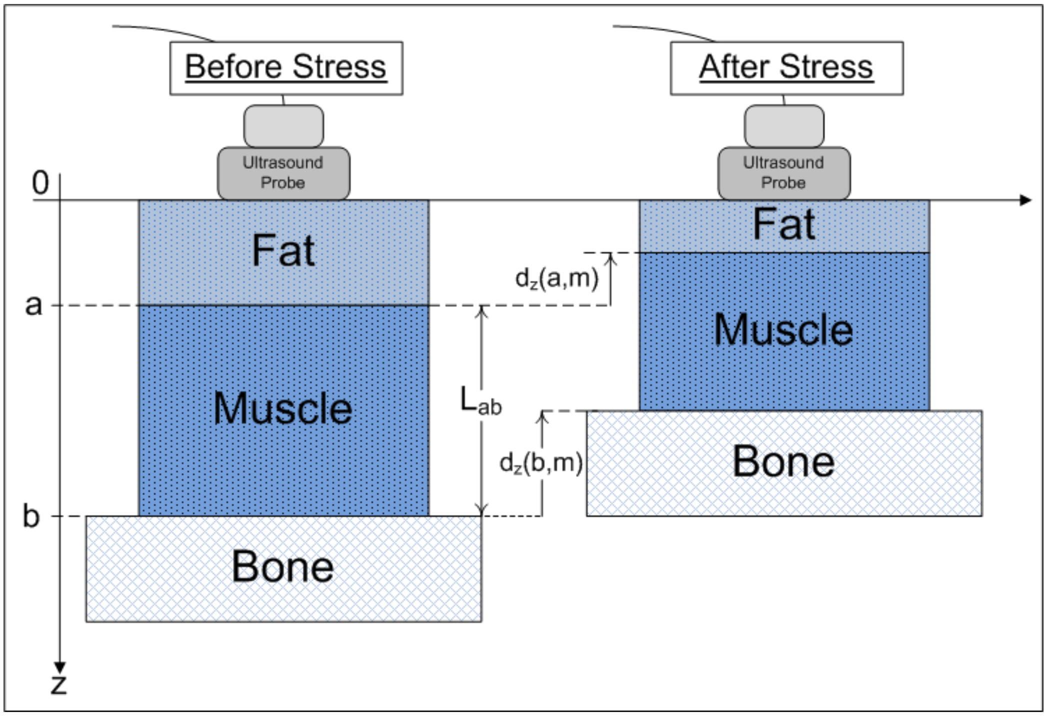

Figure 4.5 Axial strain during pre-stress and post-stress states.

4.6 Accuracy Evaluation

The following section provides a simulation based evaluation of the accuracy of the quadrature demodulation method when exposed to white gaussian noise. In addition, a definition and discussion of a large source of error encountered during this thesis research termed phase jumping is provided.

4.6.1 Simulated Quadrature Demodulation Phase Accuracy

A simulation was designed in order to demonstrate the phase accuracy of the quadrature demodulation procedure. This simulation used a sinusoidal signal as the message of a received ultrasonic signal to be demodulated. The sinusoidal message signal was multiplied by a carrier or center frequency of 5 MHz in order to simulate conditions found in the ultrasonic hardware. White gaussian noise was then added to the signal such that the signal to noise ratio (SNR) varied from -50 dB to 20 dB. This noisy signal was averaged using a moving average filter with a window size of 21 samples before it was demodulated using the described quadrature demodulation method and compared to the initial known ideal message signal. Based on this comparison the standard deviation was calculated and represents demodulation accuracy.

An example of an ideal signal along with the demodulated version can be seen below in Figure 4.6 when the SNR was -5 dB. The standard deviation as it varied with SNR can be seen in Figure 4.7 below. By analyzing the results of this simulation it can be shown that in order to obtain a displacement measurement resolution better than 5 µm a minimum SNR of at least 3 dB is required. This SNR should be obtainable using the described ultrasonic hardware. Therefore, it can be seen from these results that the demodulation method used is accurate assuming a reasoniable level of SNR is obtained.

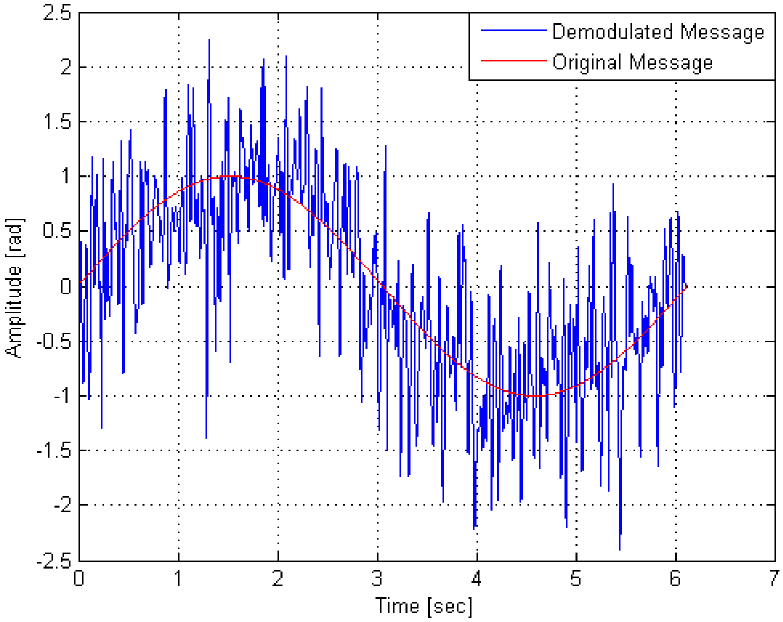

Figure 4.6 Original and demodulated phase signal. The signal was demodulated from a received signal having a SNR of -5 dB.

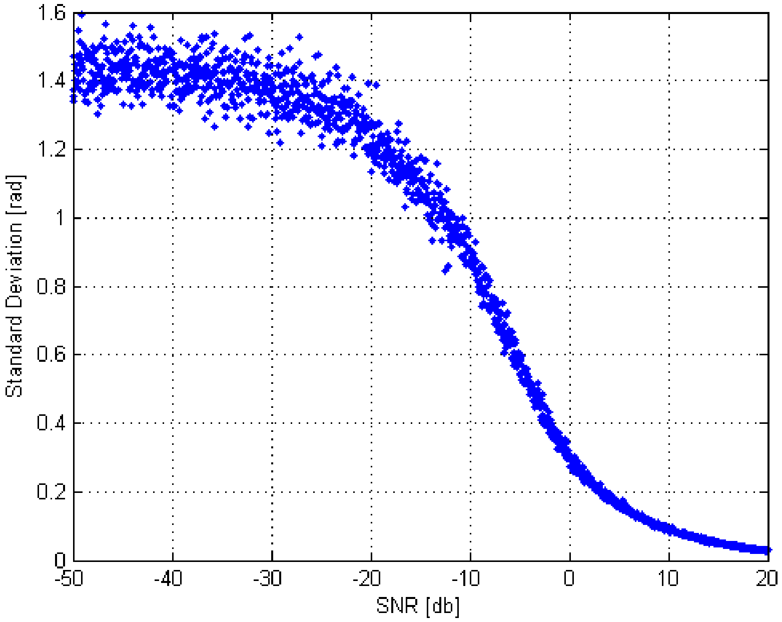

Figure 4.7 Simulated standard deviation vs. SNR.

4.6.2 Phase Jumping

The issue of phase jumping is mentioned throughout this thesis. Phase jumping is a source of error that seemed to occur during the demodulation process and most effected results measured with respect to fast time. This error was observed during both phantom and in vivo experiments and appeared as seemingly arbitrary jumps in phase of the demodulated signal. These jumps resulted in a signal that appeared to be discontinuous. The phase jumping error was the largest source of error encountered during research, and work was done to lessen its effects and to determine its source. The phenomenon was never fully resolved and its complete definition and subsequent removal are left as future work. However, a simulation was designed in order to display the concept of phase jumping as well as a possible solution. The results of this simulation can be seen below.

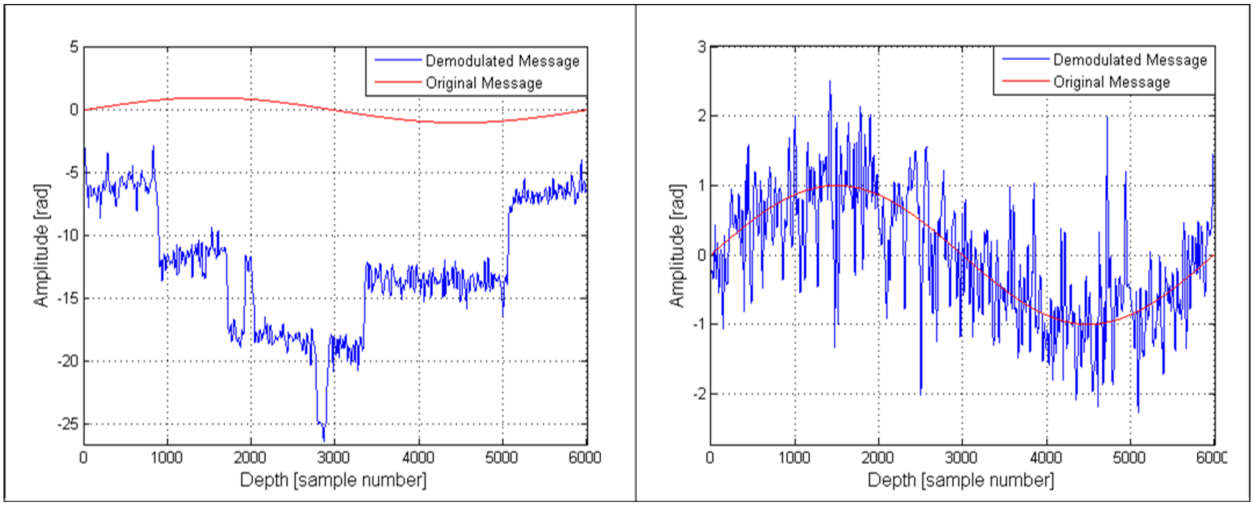

(a) **(b)**

Figure 4.8 Phase jumping phenomenon. Simulated original and demodulated message signals shown before (a) and after averaging (b), with a SNR of -5dB.

The simulation involved demodulating an FM signal with a sinusoidal message signal. The received signal was degraded by adding white Gaussian noise at varying signal to noise ratios (SNR). The above figure demonstrates the results of the simulation when noise was added which resulted in a SNR of -5 dB. In Figure 4.8 (a), the phase jumping phenomena is clearly observed on the demodulated signal. The demodulated signal looks as if it should be continuous, but has many seemingly arbitrary jumps in phase. These phase jumps are not present in the original signal and as such they represent a source of error. However, after applying a 21 point moving average filter, the demodulated signal in Figure 4.8(b) does not show the phase jumping effect. Although the demodulated signal in this figure is extremely noisy due to the low SNR, it can still be seen to follow the general trend of the ideal message signal.

The results of Figure 4.8 provide evidence that a possible solution to the phase jumping problem could be found with the application of filtering. However, because much more complex operations were done on actual measurements it was very difficult to determine the optimal location and type of filtering that should be used. This simulation demonstrates the phase jumping phenomenon along with a suggested solution of using some form of filtering such as averaging to remove its influence. The exact implementation of this solution is left as future work.

Chapter 5:

Methods of Muscle Motion Measurement and Motion Artefact Removal

In laboratory experiments it is possible to create situations in which it is very unlikely that the ultrasound probe or material being imaged will experience movement. However, in many clinical ultrasound applications, the probe is held by a trained medical practitioner. In this case, it is very likely that the probe and imaging area will move during measurement. For the ultrasonic monitoring of muscle motion studied in this thesis research, the probe or object motion is desirable when measuring overall global tissue motion, but should be removed when measuring internal tissue motion.

In clinical applications such as blood flow measurements, a notch filter called a clutter filter is used to remove unwanted motion caused by such phenomena as the heartbeat or breathing [62]. However, when considering the goals of this thesis, the use of a clutter filter is not desirable. The reason for this is that the musculature motion signals of interest could have a motion frequency content close to that of the frequency of the unwanted motion signals that should be removed. Therefore, a unique motion artefact removal technique has been developed and will be discussed in the chapter to follow.

5.1 Motion Artefact Definition

The concept of motion artefact is one that must be defined in order to fully understand the purpose and methodology developed in this chapter. The concept of motion artefact will be defined in this section as it applies to this thesis research. To begin with, the term motion artefact will be used to refer to motion caused by very specific phenomenon. In addition, it should be noted that it may not always be desirable to remove this motion artefact as will be explained to follow.

Motion artefacts, for the purposes of this thesis, are defined as any motion in a direction parallel to the ultrasonic beam caused by the external motion of the ultrasonic probe or of the entire object being imaged. This concept of motion artefact corresponds to global motion when the probe is coupled with the object being imaged and allowed to move freely with its surface. However, when dealing with measurements of internal motion, this motion artefact represents a source of error that needs to be removed. Details of these concepts will be provided in the remainder of this chapter.

5.2 Principles and Assumptions

The following section deals with the principles of motion as observed by the ultrasonic probe. It outlines how motion relates to the concept of motion artefacts as well as when and why these artefacts are desired in some cases but removed as unwanted signals in others. However, before describing motion and its measurement, some assumptions used throughout this chapter and thesis should be defined. The first has to do with the object being imaged. In order to analyze skeletal muscle motion, a phantom system was designed to mimic the conditions found in actual human skeletal muscle. The phantom systems developed are described further in Chapter 6. However, regardless of whether considering phantom or in-vivo images, it is always assumed that the area being imaged will contain a layer of soft material such as fat. This layer will be followed by one or more deeper layers of stiffer material like muscle. This stiffer layer is then followed in depth by an area of uncompressible material such as bone. For the purposes of this chapter, the compressible layers are often referred to as tissue and the uncompressible layer is referred to as bone.

It should be noted that as stated previously in Section 4.1 the origin of the measurement coordinate system is located at the surface of the probe. The result of this definition is that all motion captured during ultrasound measurements are relative to the probe surface. Therefore, if a uniform object being imaged is uniformly compressed, the largest motions will be observed at the deepest areas with the magnitude of the displacement decreasing towards the surface of the probe. Finally, it is assumed that motion as measured in this thesis occurs in a direction parallel to the ultrasonic beam in the axial direction unless stated otherwise.

5.2.1 External Motion

External motion is defined as occurring due to motion of the probe or of the object being imaged. This type of motion has been classified as a motion artefact. In the case of imaging an area containing some uncompressible material or bone, this type of motion can be defined as when the distance between the probe surface and the bone varies. This occurs due to some combination of the probe moving towards or away from the bone or the bone moving towards or away from the probe. Motion of the bone is assumed to be caused by external motion of the object being imaged. Due to the fact that the coordinate system origin is taken at the probe surface, motion as a result of probe movement appears identical to motion caused by external object movement during ultrasonic measurements. An example of external motion can be seen in Figure 5.1 below. This figure depicts a scenario in which the probe is physically pushed down towards the bone layer. The result is the appearance of the bone layer moving closer to the probe surface.

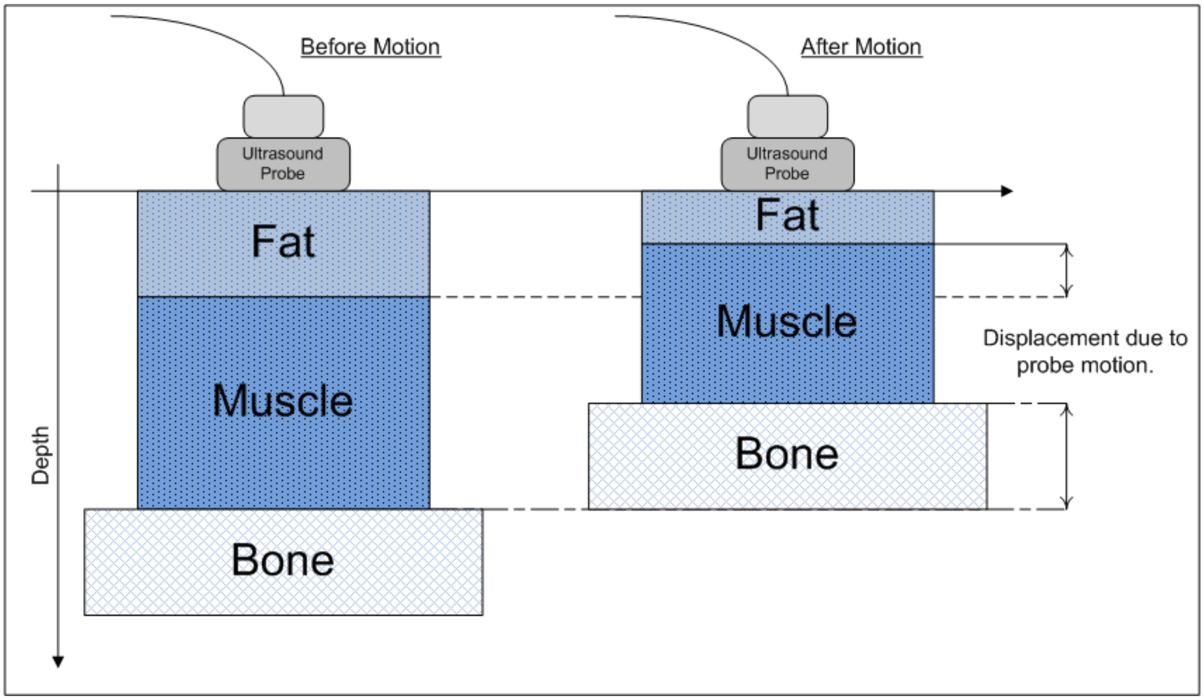

Figure 5.1 External motion due to probe movement.

5.2.2 Internal Motion

The other type of motion that must be considered is that of internal motion. Internal motion occurs and originates, as its name would suggest, internally to the object being imaged. In the ideal case of measuring internal motion, the probe and object being imaged would be completely fixed. This would result in a constant distance between the probe surface and the bone. In this ideal case, observed motion can only be as a result of internal movement. During in vivo conditions, internal movement can be thought of as a muscle contraction originating within the tissue area being imaged at some depth within a layer of muscle. An example of this type of motion can be seen below in Figure 5.2. It can be seen in this figure that the muscle layer expands which consequently contracts the fat layer while the distance between probe and bone remains constant.

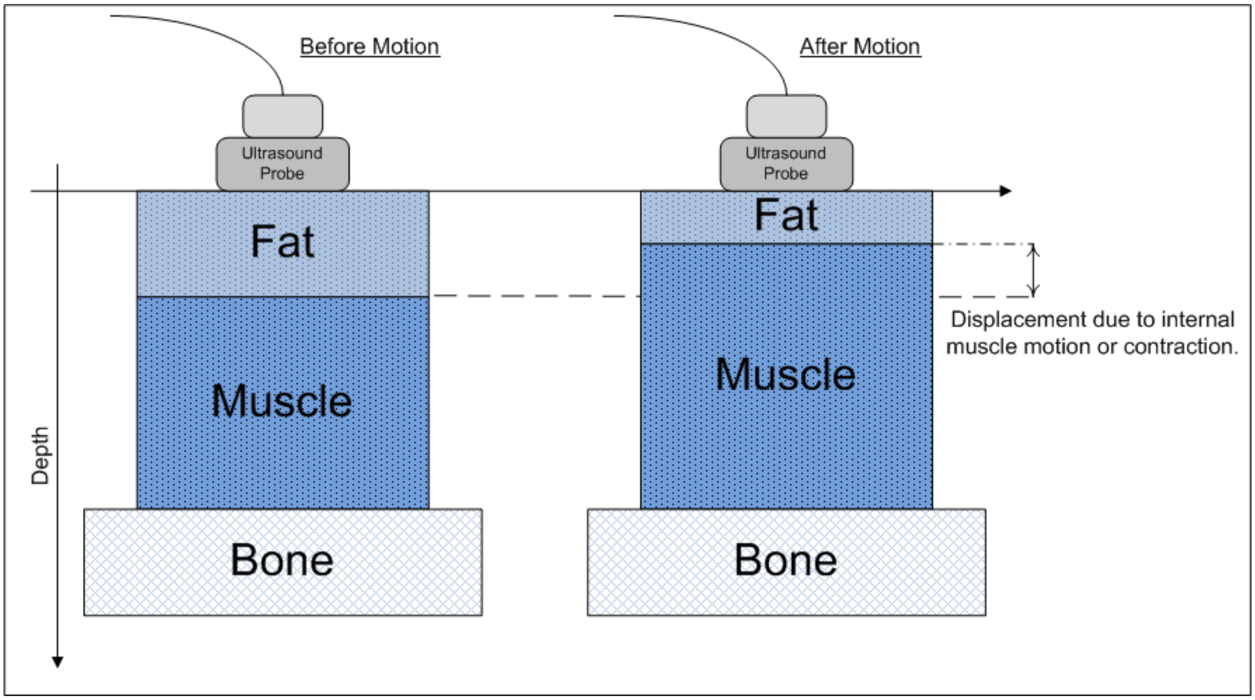

Figure 5.2 Internal motion due to muscle contraction.

5.3 Ultrasonic Motion Measurements

It is first necessary to understand when motion artefacts should be removed before describing the procedure used to remove them. Firstly, as described above, there are two different kinds of motion; external motion, in which the probe or entire object being imaged move and internal motion. These two different forms of motion result in two different types of motion that can be measured. The first is that of global surface motion and the second is that of internal motion.

Motion can be measured using ultrasound by estimating the time delay change of an ultrasonic echo from within the object being imaged. Specifically, a probe or external object movement can be estimated by measuring the time delay change of an ultrasound echo reflected from the surface of the bone or uncompressible material. If this time delay does not change it can be said that the distance between the probe and the bone has been kept constant. This, in turn, means that there has been no relative probe or object motion during measurements.

5.3.1 Measuring Global Surface Motion

In the first case of global motion, it is the motion at the surface of the object that is of interest. The motion at the surface of the object represents a summation of any motion that has occurred internally. For instance, when a muscle contracts, the surface of the skin above it moves in relation to the motion occurring within the muscle. This type of movement tends to be measured with MMG as mentioned in Section 2.4.2. However, it can also be measured ultrasonically. This can be done ideally by fixing the probe to the surface of the object being imaged, i.e. the skin, such that it moves dependently with respect to the surface motion of the object. In this case, the motion artefact is equivalent to the global motion at the object surface.

This type of global motion is measured when the probe is allowed to move relatively to the surface of the object being imaged. The probe itself will move in response to a force originating within the object being imaged. This motion of the probe will result in a change in distance between the probe surface and the bone which is defined as the global motion experienced at the surface of the object being imaged. In this case, as explained above, the motion artefact is equivalent to the desired global motion measurement and should not be removed. The concept of global surface motion measurement can be seen in Figure 5.3 below.

5.3.2 Measuring Internal Motion

In order to measure motion internal to the object being imaged, the distance between the probe and the bone must remain fixed. In this case, any motion of the probe or of the entire object being imaged is unwanted and should be removed. Defining a way in which to remove the motion artefact in this case is essential because any externally occurring motion will be observed in addition to the internal motion. If not removed, the external motion becomes a source of error on the measurement of internal motion.

As stated above, if the probe is completely fixed and the entire object being imaged does not move then the distance between probe and bone will remain fixed. In this situation, any motion measured will be as a direct result of only that motion occurring internally to the object being imaged. Practically, however, physically fixing the distance between the probe and the bone is difficult. During in vivo measurements the probe may be pushed into or pulled away from the tissue being imaged by the individual holding the probe. In addition, the tissue being imaged may move due to voluntary or involuntary muscle contractions. Even in phantom simulations the probe cannot be completely fixed and tends to move slightly with the expansion and contraction of the phantom beneath it.

Due to these reasons and the fact that internal tissue motion can be much smaller than motion artefacts, it is important to remove as much of the motion artefact as possible.

In order to remove the motion artefact and accurately measure internal motion, a method has been developed and was used to obtain the results shown in the following chapters. Through analysis of the ultrasonic signals obtained, the developed methodology essentially fixes the distance between the probe and bone regardless of the motion occurring during signal acquisition. The differences between measuring global surface and internal motion are illustrated in Figure 5.3 below.

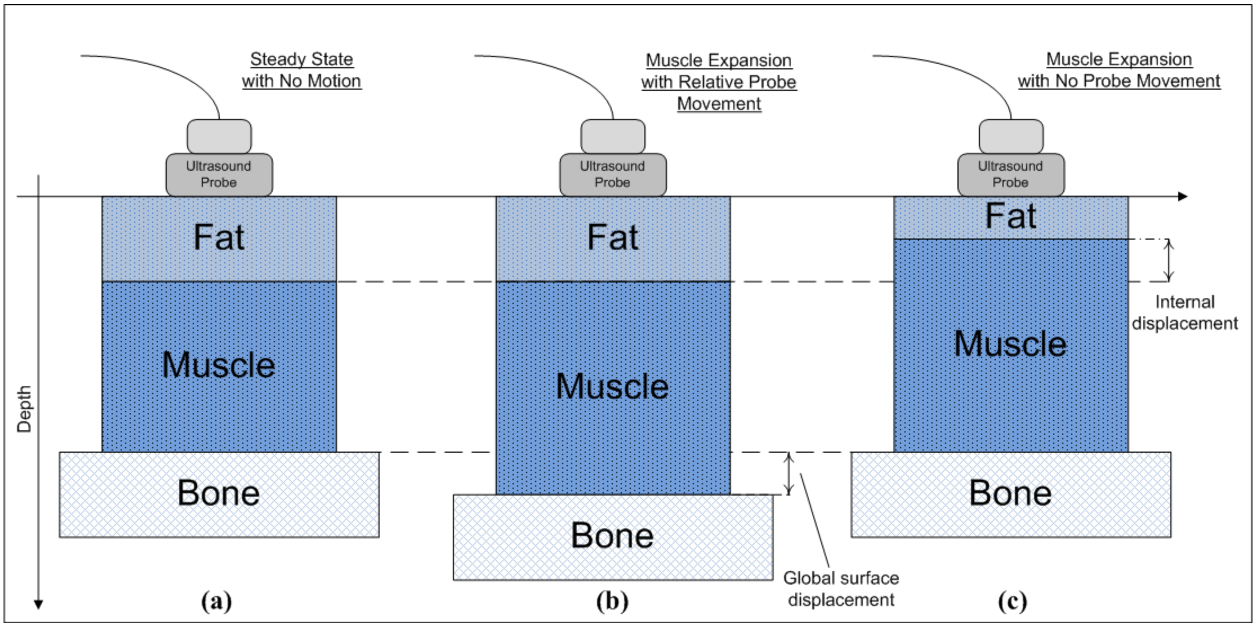

Figure 5.3 Ultrasonic motion measurements. The measurement conditions are: (a) tissue at steady state with no motion of any kind occurring, (b) muscle expansion with the probe moving relative to the surface allowing measurement of global surface motion and (c) muscle expansion with no probe motion resulting in a fixed distance between probe and bone allowing for internal motion measurements.

5.4 Removing Motion Artefacts

The principles used to remove motion artefacts are based on the way in which motion occurs. As stated above, ultrasonic measurements were taken of human tissues or similar materials. In such cases, it was assumed that the area to be imaged contained layers of compressible material such as fat and muscle followed by an area of uncompressible material such as bone. The areas of compressible material will experience motion as a result of any internal or external motion such as muscle contraction or probe movement. However, because it cannot be compressed, the uncompressible material or bone should experience no motion as a direct result of any internal motion. Rather, motion observed at the bone surface or boundary is due only to motion artefacts as defined above. For this reason, any motion captured from an area of known uncompressible material such as bone can be assumed to be only as a result of external motion of the probe or of the global motion of the area being imaged. Ideally, by using this motion measured at the bone surface, it is possible to remove the effects of motion artefacts from any measured motion signal.

There are three major aspects of the process used to remove motion artefacts. The first has to do with the measurement procedure used to collect data. The second requires the location and tracking of the interface between the compressible and uncompressible material or bone. This tracking signal from the uncompressible material or bone boundary represents displacement as a result of only the motion artefact and is referred to as the bone boundary displacement signal. The final major aspect of motion artefact removal involves scaling the bone boundary displacement signal with respect to depth and subtracting it from the measured displacement at any other depth. The result of this subtraction represents a measurement of the internal motion that occurred at that depth.

The specifics of the procedure used to remove motion artefacts are detailed in the following sections. Due to the necessity of obtaining a signal from an uncompressible material or bone boundary the developed motion artefact removal algorithm will be referred to as the Bone Boundary Referencing Method of Motion Artefact Removal or bone boundary method for short.

5.5 Measurement Procedure and Reference Data

As mentioned above, one of the main components of the bone boundary method is the manner in which data is collected. As stated in Section 4.1, displacement magnitude varies with depth through a material. Due to this fact and the defined coordinate system, in a uniform object under uniform stress, the largest displacement magnitudes will be observed at the deepest locations and the displacement magnitude will decrease linearly as the observation area becomes shallower. It was always assumed that the uncompressible material or bone would occupy the deepest region of interest in any experiment. Therefore, the displacement estimated from the surface of the bone had to be scaled relative to depth before it could be used to subtract the effects of motion artefacts from any particular depth. This scaling was accomplished by analyzing a section of the collected data referred to as the reference section.

To facilitate depth scaling, a time period of signals containing motion as a result of only probe motion was always obtained. This was done by pushing the probe down into the object being imaged before experimental muscle motion data acquisition occurred.

Once this data had been acquired, the data for measuring muscle motion was obtained. The result is that any collected data set is referred to as having two major sections: the reference area containing the known probe motion and the experimental section containing the desired experimental signal(s). Figure 5.4 below shows a simulation of displacement at an arbitrary depth containing both the reference and experimental sections. The reference data section can be seen as a change of displacement representing a smooth push and release of pressure applied by the probe into the object being imaged. The experimental data section shows a triangular pulsatile displacement used to represent a periodic muscle twitch.

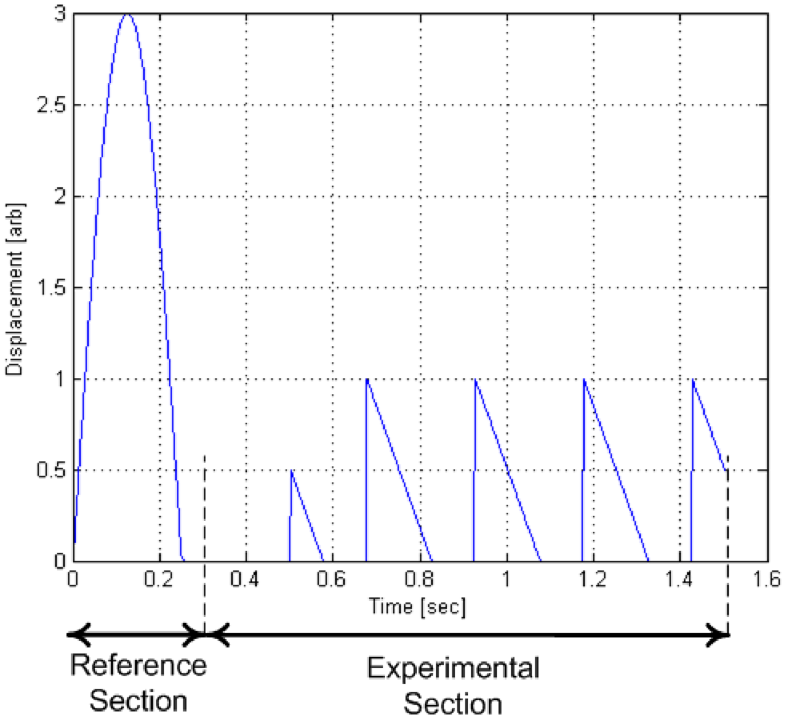

Figure 5.4 Simulated reference and experimental data. The triangular pulses in the experimental section approximate the signal observed during in vivo electrical muscle stimulation.

5.6 Bone Boundary Echo Tracking and Bone Boundary Displacement

Once the data is acquired using the experimental method described in Section 5.5, the data processing can begin. The first step has to do with locating and tracking the displacement of the surface of the bone. For the purposes of this step in the bone boundary algorithm, the region of interest was located at the exact depth where the ultrasound wave first encounters the tissue-bone interface. The displacement at the bone boundary and therefore of the motion artefact can be estimated by measuring the time delay change of an ultrasound echo reflected from the surface of the bone.

The tracking of the bone boundary is done with respect to the demodulated baseband envelope signal with reference to a B-mode image. The first step in the procedure requires the identification of the initial location of the bone boundary. This was done by analyzing the envelope of the first acquired scan line as well as a B-mode image. An approximate location in depth of the bone boundary can be determined from the B-mode image based on knowledge of anatomy and ultrasound imaging properties. A large peak can then be found in the envelope signal near where the bone boundary location is expected to be from the approximation using the B-mode image. It was usually obvious where the bone boundary was located just from an analysis of the baseband envelope. However, the B-mode image was used as an extra measure of certainty. An example of a baseband envelope signal with the bone boundary location marked is shown below in Figure 5.5.

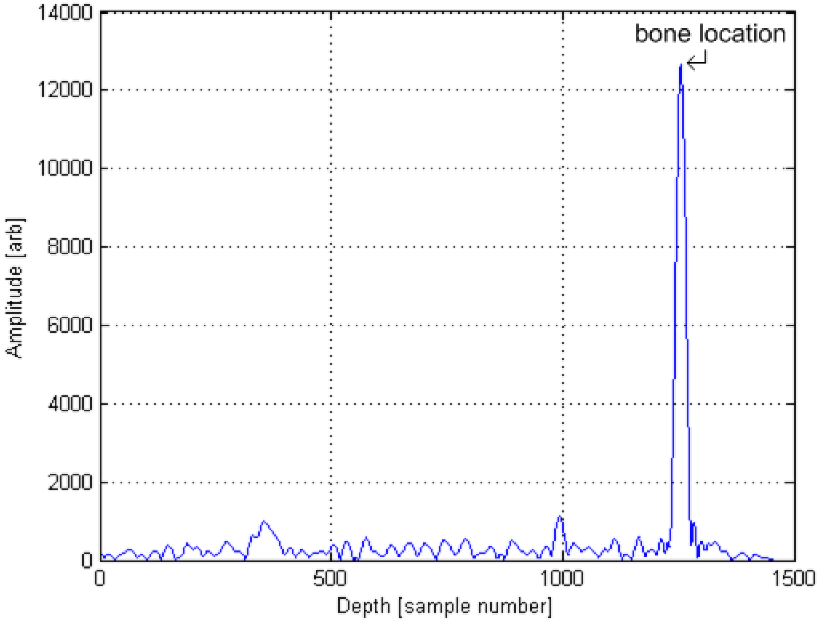

Figure 5.5 An envelope signal used to determine bone surface location. It is marked in this figure due to its large amplitude and was verified with the inspection of a B-mode image.

Once the initial bone boundary location was defined, it was automatically tracked for all scan lines to follow in the subsequent data set. This was done using a developed windowed peak detection algorithm. The algorithm works by looking for the largest value within a defined window size. The window is defined by setting the center point to the last known sample number location of the peak in the envelope signal corresponding to the bone boundary. The purpose of this window is to eliminate the effect of signal amplitude variation and decreases the effect of location jumping from peak to peak. Optimal selection of the width of the window can all but ensure the same peak is being tracked over all time under our experimental conditions.

Through experimental observations, a window size of 21 sample points in depth was adopted as the default size. This window size is small enough to provide accurate tracking while remaining large enough to account for a wide range of possible motions. Assuming an ultrasound wave propagation velocity through a material of 1540 m/s [91], a window size of 21 sample points allows the bone location to move 231 µm in either direction between two consecutive frames. This contains all possible movements of the bone due to the stipulation explained in Chapter 4 that no motion may cause a phase shift of more than 2π radians between consecutive temporal samples. Assuming an ultrasonic center frequency of 5 MHz the result of the 2π radian constraint is that displacement must be no more than 154 µm between consecutive temporal samples since the ultrasonic wavelength is 308 µm at 5 MHz. The window size was chosen such that the resulting motion was high enough above the 154 µm threshold to account for some possible variations due to noise and all possible temporal acquisition rates.

The bone boundary displacement signal is a slow time dependant estimation of displacement obtained by tracking the bone surface location over time with the aforementioned windowed peak tracking algorithm. It is used to subtract the effects of motion artefacts from internal motion measurements. For each scan line in every frame, the peak tracking algorithm locates the sample number corresponding to the bone boundary location. The displacement occurring at this determined depth is then stored as the value of the bone boundary displacement signal for the current scan line in the current frame. By repeating this process over all time (temporal, slow time samples), a time dependant displacement signal from the uncompressible material or bone boundary is obtained. The bone boundary displacement signal d_{ext} in the beam direction z representing the global external surface and motion artefact can be represented as

$$d_{ext}(m) = d_z(n_{bone}, m) \tag{5.1}$$

where $d_z(n, m)$ is the accumulated displacement as obtained in Chapter 4 and n_{bone} is the located depth sample number of the bone boundary at temporal sample number m.

5.7 Depth Scaling and Motion Artefact Removal

The magnitude of the displacement due to motion artefacts occurring within an object varies with respect to depth based on the stress-strain profile of the object. Therefore, the bone boundary displacement signal representing motion artefact was scaled relatively to any particular depth location by a scaling factor determined for all depths. This was done using the reference section of the collected data as it was assumed that this section of the data contained motion occurring only as a result of a motion artefact. Specifically, by comparing the peak-to-peak displacement during the reference section of the bone boundary signal to the peak-to-peak displacement during the reference section of the signal from any depth, a scaling factor for any particular depth was obtained. The scaling factor $SF_z(n)$ in the beam direction z, at a depth sample number n can be represented by

$$SF_z(n) = \frac{|max\{d_z(n, m_{ref})\} - min\{d_z(n, m_{ref})\}|}{|max\{d_{ext}(m_{ref})\} - min\{d_{ext}(m_{ref})\}|} \tag{5.2}$$

where m_{ref} represents all temporal samples within the reference section, $d_{ext}(m)$ is the bone boundary displacement signal and $d_z(n, m)$ is the accumulated displacement at depth sample n and temporal sample m.

Ideally, it is only necessary to compare displacement magnitudes at a single point. However, the end goal of the methodology is to be applicable during in vivo measurement. In these scenarios, the stiffness of the tissue can change over time due to muscle contraction and relaxation. This physical change in the tissue can affect how the tissues themselves deform. Specifically, a peak displacement occurring at some time observed at one depth may occur at some other time at some other depth. Therefore, the peak-to-peak displacement magnitude is used in order to ensure that similar quantities are being compared regardless of any time shift that may have occurred. It was experimentally determined that this method provided the best results for our research.

The bone boundary displacement signal is multiplied by the scaling factor for all depths in order to obtain $d_{artifact}$, the depth scaled bone boundary displacement signal. This displacement is due only to motion artefacts and represents their effect on displacement at any particular depth, calculated by

$$d_{artifact}(n,m) = SF_z(n) \cdot d_{ext}(m). \tag{5.3}$$

Due to the practical potential error introduced during conversion from phase to displacement, the scaling was actually done on the estimated phase. However, displacement and phase are ideally treated as equivalent values in this chapter with the assumption that the conversion from phase to displacement is error free. In order to remove the effects of motion artefacts at any particular depth, the depth scaled bone boundary displacement due only to motion artefacts is subtracted from the displacement at any depth. The result is d_{int}, an estimation of the actual internal displacement at any depth without the effect of motion artefacts, given as

$$d_{int}(n,m) = d_z(n,m) - d_{artifact}(n,m). \tag{5.4}$$

A flowchart of the entire procedure developed and used to remove the effects of motion artefacts can be seen in Figure 5.6 below.

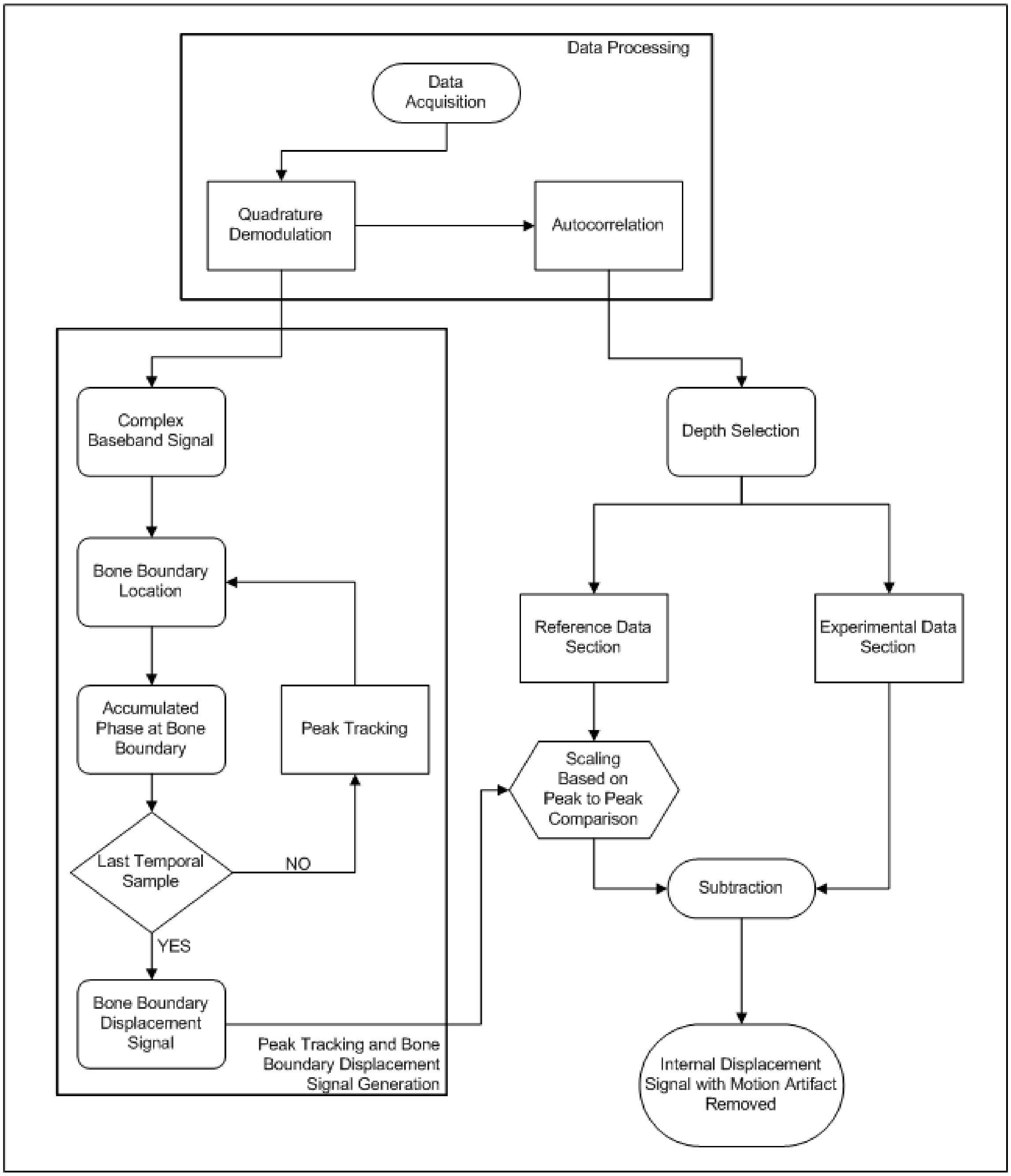

Figure 5.6 Flowchart of bone boundary method of motion artefact removal.

5.8 Accuracy Evaluation

In order to test the validity and evaluate the robustness of the bone boundary algorithm, a software simulation was designed and performed. The simulation created 1472 M-mode scan lines over a depth range of 100 sample points. The object being imaged was assumed to be uniform and as such, the displacement magnitude increased linearly with respect to depth. The scan lines were sampled at a rate of 980 Hz which is the M-mode temporal sampling rate of the employed ultrasound imaging machine and resulted in a total of about 1.5 seconds of data.

The reference and experimental artefact motion were simulated using a periodic sinusoidal wave. The muscle contractions were simulated using a train of triangular pulses with a width of 0.15 seconds and a repetition rate of 4 Hz. This pulse train provided similar results to those seen in actual in vivo measurements during electrical muscle stimulation presented in Chapter 7. An example of a simulated waveform containing reference and muscle contraction signals can be seen without any motion artefact above in Figure 5.4. The simulated motion artefact, muscle pulse and muscle pulse with motion artefact can be seen below in Figure 5.7. The simulated reference and experimental data with motion artefact present can be seen combined together at an arbitrary observation depth in Figure 5.8 below.

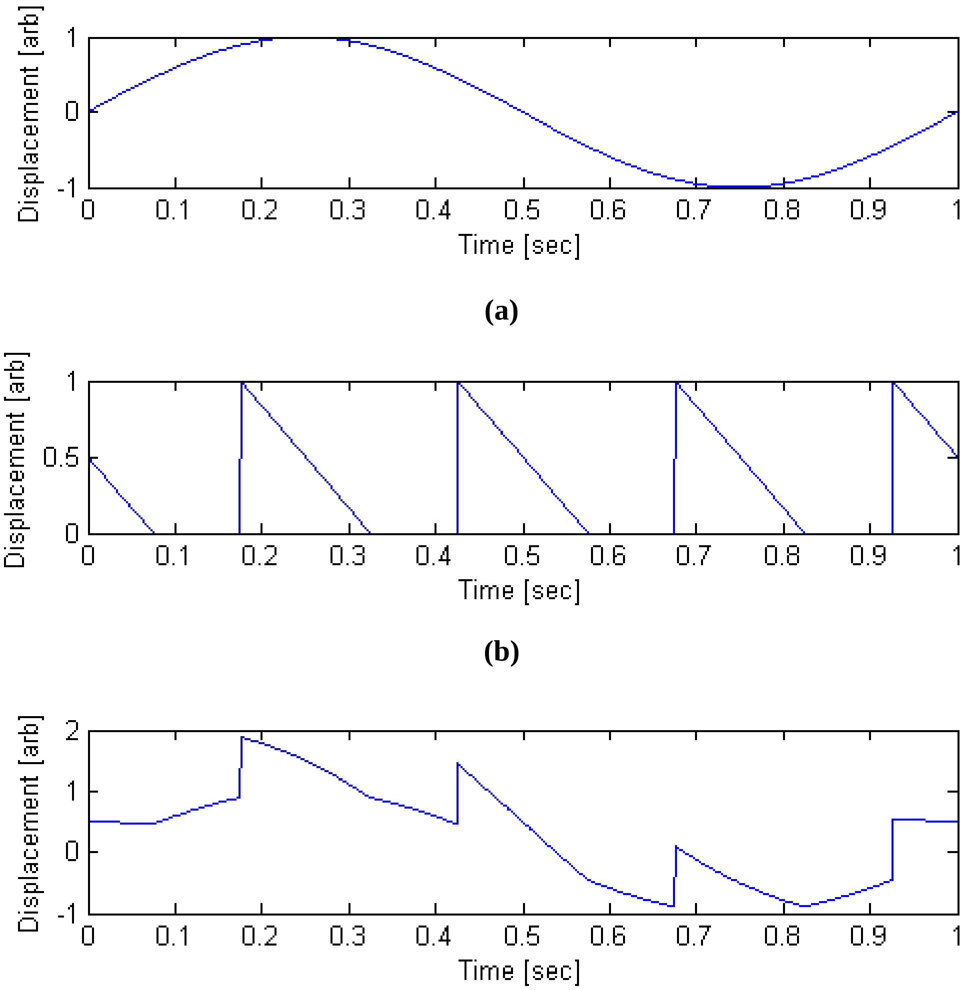

(a)

(b)

(c)

Figure 5.7 Simulated (a) motion artefact, (b) muscle motion and (c) muscle motion with motion artefact.

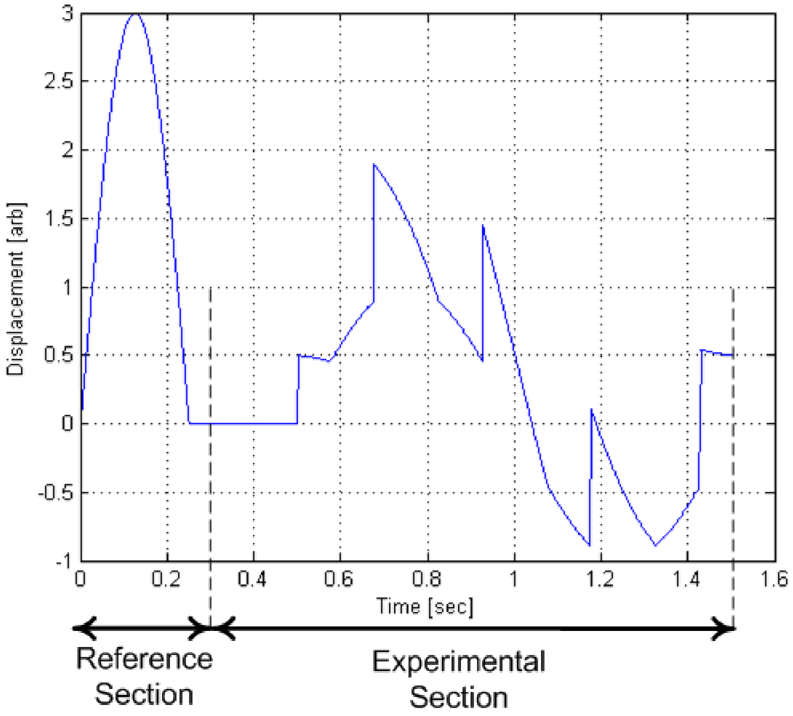

Figure 5.8 Simulated reference and experimental data containing motion artefact.

This simulation environment was developed in order to provide a platform that can be used to evaluate the performance of the bone boundary algorithm for motion artefact removal. The simulated signals described above can be utilized and manipulated in a number of different ways in order to test various aspects of the bone boundary algorithm. In order to demonstrate one such example, the results shown in Figure 5.9, Figure 5.10 and Figure 5.11were obtained after adding Gaussian noise as error to the simulated displacement estimation.

The purpose of this simulation was to test the ability of the bone boundary algorithm to function under varying conditions of raw displacement estimation error. In addition, the muscle pulse amplitude with respect to artefact motion amplitude was varied and the effect of this variation was analyzed. The following simulation was done to verify the hypothesis that the bone boundary algorithm is not a limiting factor on the overall accuracy of our muscle measurement system.

In order to test how well the motion artefact removal algorithm performed under varying conditions of displacement estimation error, white Gaussian noise was added as error to the simulated collected data in both the reference and experimental sections. For this reason, raw displacement estimation error is referred to as noise for the purposes of this simulation. The signal to noise ratio or SNR was varied from 30 dB to -10 dB by steps of 0.5 dB. The SNR actually represents the ratio between ideal displacement estimation and displacement estimation error rather than a conventional signal to noise ratio. However, because noise is assumed to be caused by estimation error in this simulation, the term SNR is used.

After adding noise and applying motion artefact removal by the bone boundary algorithm the resultant signal was compared to an ideal signal and the standard deviation was determined. The result of this simulation can be seen in Figure 5.9 below which shows that at 15 dB an error of about 20% should be expected. Although this value seems very high, it is important to recall that SNR actually represents error that has been added to the displacement estimation. These simulation results suggest that the bone boundary algorithm error is more a reflection of the addition of displacement estimation error as noise than of the algorithm itself.

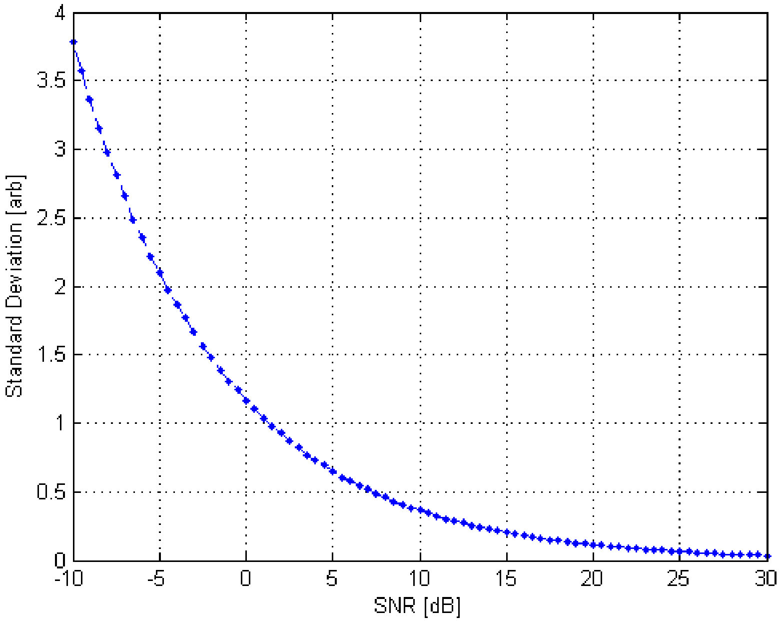

Figure 5.9 Simulation results of standard deviation of bone boundary algorithm vs. signal to noise ratio (SNR).

The second simulation was used to test the performance of the bone boundary algorithm in the case of a constant level of displacement estimation error added as noise. The purpose of this simulation was to test the effect of varying the magnitude of the desired muscle twitch displacement with respect to the magnitude of the motion artefact. To accomplish this, the muscle displacement magnitude was varied from ten times larger to ten times smaller than the artefact motion magnitude. The result of the bone boundary algorithm was compared to an ideal result and the standard deviation was calculated for the varying ratio of artefact to muscle motion magnitude.

In the ideal case, when no noise was added, the standard deviation of the bone boundary method was on the order of 10^{-16}. This error level is so low that it is more likely a representation of the round-off error of the computer used during simulation than of the algorithm itself. However, this low error level could suggest that the accuracy with which the bone boundary algorithm removed the motion artefact is not dependent on the magnitude of the muscle motion relative to the magnitude of the motion artefact.

To help verify this hypothesis, the simulation was repeated with the addition of raw displacement estimation error as white Gaussian noise resulting in a SNR of 30 dB. This value of 30 dB was chosen because it can be seen from Figure 5.9 above that the bone boundary method will have less than 3% error at 30 dB. The result of this simulation can be seen in Figure 5.10 below. This figure demonstrates a fairly constant error regardless of simulated muscle motion magnitude. The error is approximately equal to that seen in Figure 5.9 at 30 dB. This helps to verify that there is no correlation between muscle motion magnitude and the bone boundary algorithm accuracy when the raw displacement estimation error is small enough. These results allow for the assumption that if the muscle displacement is large enough to be detected then the bone boundary algorithm is a viable method to use for the removal of the effects of artefact motion.

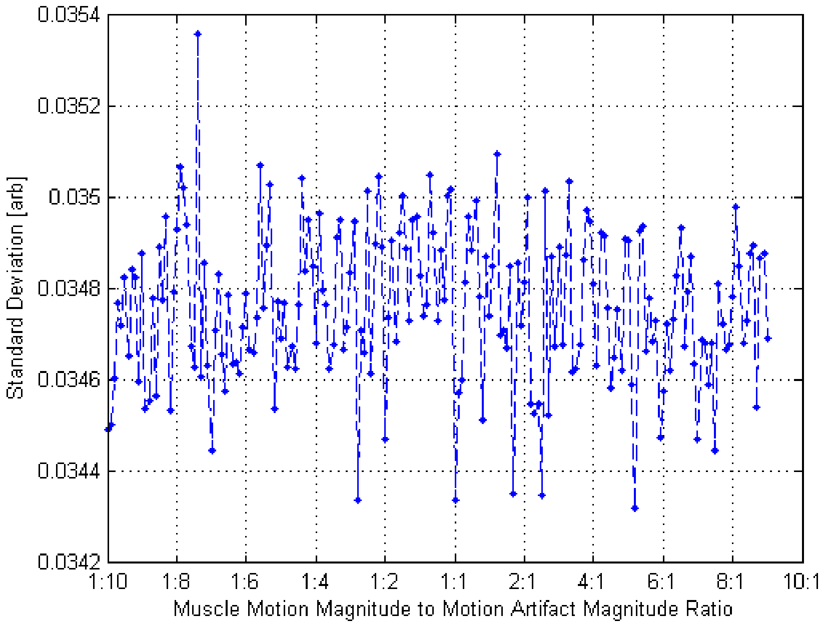

Figure 5.10 Simulation results of varying muscle motion magnitude with respect to motion artefact magnitude. The SNR during this simulation was kept constant at 30 dB.

The final simulation was used to simultaneously test both the effect of displacement estimation error and the variation of the muscle motion magnitude with respect to the magnitude of the artefact motion. The muscle signal magnitude was varied from ten times to one tenth smaller than the artefact motion magnitude. For each value of muscle motion magnitude, the SNR was varied from 30 dB to -10 dB with steps of 0.5 dB. The results are shown below in Figure 5.11 and seem to again suggest the trend of the bone boundary algorithm accuracy being more dependent on displacement estimation error variations than on variations in displacement magnitude.

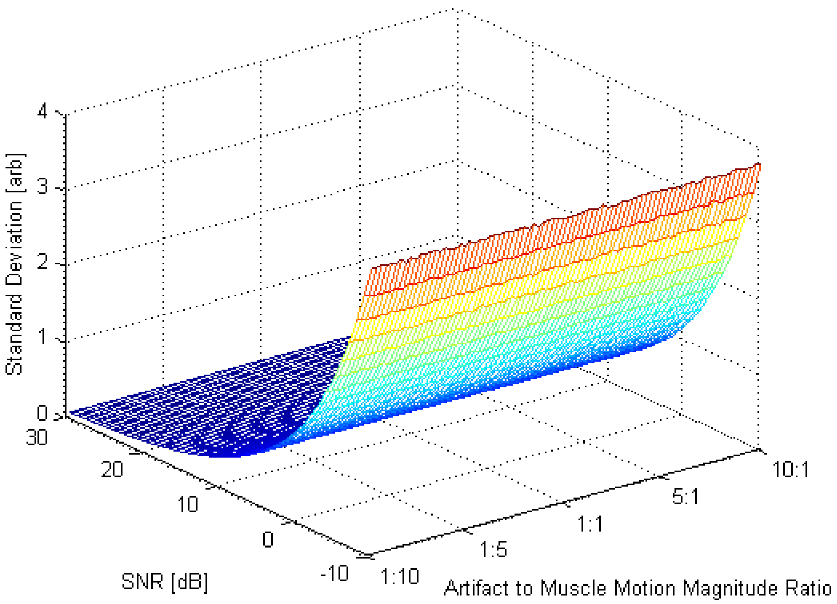

Figure 5.11 Simulation results of varying muscle signal magnitude and SNR.

This accuracy evaluation is just one example of how the simulation signals developed and shown in Figure 5.7 and Figure 5.8 can be used to analyze the bone boundary method of motion artefact removal. The simulation results verify the intuitive hypothesis that the bone boundary algorithm is not a limiting factor on the overall accuracy of the muscle motion measurement system. Rather, the error of the motion artefact removal algorithm is dependent on the error of the displacement values that it is applied to. Work can be done in the future to analyze the simulated motion signals with the addition of more complicated noise and error.

5.9 Limitations

The bone boundary algorithm can and has been shown to be very effective at removing motion artefacts. However, it does have its limitations. There are two major types of drawbacks that should be considered. Firstly, there is the problem of motion not in the direction of the ultrasonic beam. The bone boundary method is only able to effectively remove motion artefacts that are a result of motion in the direction of the ultrasonic beam. It will not properly remove or take into account any motion with a component in the direction perpendicular to the beam. However, the effect from this type of motion can be lessened with the use of various experimental designs and procedures. This issue is also encountered by any acquisition method that only considers two dimensions of displacement as is the case with the hardware system used for this thesis.

In addition, the bone boundary algorithm will not be able to correct angular motion of the probe or of the object being imaged. This can affect the algorithm because it is based on a peak detection method of object tracking. Due to the nature of ultrasonic measurements, the angle of the ultrasonic beam relative to any reflector has an effect on the amplitude of the received ultrasonic signal. This received signal is used to create the baseband envelope signal which, in turn, is used to track the desired bone boundary location based on a peak magnitude. A significant change in the peak magnitude may have an effect on the algorithm’s ability to locate the bone boundary. For example, if certain angular motion occurred, it could be possible that the amplitude at the bone boundary location would become too small to detect. This could cause a problem during the peak tracking algorithm and as a result, the accuracy of the entire bone boundary method could suffer.

Finally, there is the issue of time varying physical property changes of the tissue being imaged during in vivo measurements. A muscle contraction changes the physical properties of tissues as areas of contracted muscle become stiffer. This change in stiffness changes the stress-strain profile with respect to depth. The scaling factor used to compensate for depth dependent displacement magnitude is calculated during the reference section of the data when all of the tissue is at a steady state. The scaling factor is used both when the tissue is and is not at a steady state. This fact could introduce some error into the motion artefact removal algorithm used.

Although there are limitations to the motion artefact removal methodology, it is still a viable way to greatly reduce the effects of motion artefacts. A demonstration of its use during phantom simulation and actual in vivo experiments is provided in the chapters to follow.

Chapter 6:

Simulation Environment and Experiments

The end goal of most research is the use of a developed technique or idea in a real world application. The goal of this research is to develop techniques to perform useful in vivo measurements. It was therefore necessary to design and test a simulation environment that would simulate the conditions present in vivo while providing a more controllable experimental procedure. In previous chapters, methods used to mathematically model, simulate and test concepts have been discussed. This chapter introduces these concepts as applied to a real application using a designed simulation environment. This environment uses tissue mimicking phantoms in a designed configuration to simulate the conditions expected during actual in vivo skeletal muscle measurements. Results of testing with this system are presented and an evaluation of accuracy using the simulation environment is discussed.

6.1 Phantom Development

This section deals with both the development of the phantoms used as well as the configuration of the skeletal muscle simulation environment. It details the three different types of phantoms created as well as the preparation procedure developed to create what were found to be the most effective phantoms for this thesis research. Although three different phantoms were developed, they all shared the same overall goal to be as similar to human skeletal muscle tissue and fat as possible. Aside from being physically similar to human tissues, it was also necessary that any phantom used would have an ultrasonic propagation velocity on the order of 1500 m/s. This value was chosen due to the widely accepted standard of ultrasonic propagation velocity through human tissue of 1540 m/s [91]-[93]. A value of ultrasonic propagation velocity through a material of 1540 m/s ± 100 m/s was adopted as an acceptable range for a phantom analog of human tissue for experimental purposes in this thesis.

6.1.1 Silicone Phantom

The first phantom developed was a silicone based phantom. Although it was only briefly used, its discussion is important in the overall development of the final ultrasound phantom employed. The silicone material used was supplied by Dascar Plastics and is called RTV-1000. The procedure used to make a phantom out of this material was very simple. The material comes in two separate containers. One contains a base and the other an activator. A 5cm x 5cm x 5cm mould was constructed. Once this was done, ten parts base to one part activator by weight were mixed together. The entire solution solidified after 1.5 hours and had set firmly within 24 hours. Once set, the phantom’s properties were tested. It was found that the ultrasonic velocity through the material was on the order of 1500 m/s. This is consistent with the accepted standard as mentioned above.

Although the ultrasound velocity through this silicone phantom was within the acceptable range and it had a very long lifetime, there were attributes that made it un-useable for the experiments to follow. Overall, there were three main flaws with this silicone phantom. Firstly, the material, once set, was far stiffer than biological tissues of our interest such as muscle and fat. This meant that testing for internal vibrations would produce very different results from those expected within actual tissue.

Secondly, the material is sonically transparent. This means that all ultrasonic waves pass through the material and are not reflected back to the transducer. For this reason, ultrasonic scattering material had to be uniformly added to the mixture. However, due to the high viscosity of the material during mixing, it was difficult to approach a uniform distribution of particles with our facilities at the time of writing this thesis. This non-uniformity would greatly skew any results obtained when using this type of phantom. It should be noted that better uniformity can be attained with more robust mixing equipment.

Finally, there was a practical problem with degassing the phantom during production. This material required pouring and mixing to ensure a good phantom. However, the pouring and mixing introduced air bubbles. This was an obvious problem as there are no air bubbles in any human tissue and ultrasound signals are entirely attenuated by air. In the future, degassing could be performed using a vacuum pump. For these reasons, the silicone phantom was dismissed as a viable option for phantom study with respect to this thesis research.

6.1.2 Gelatin Phantom

The second type of phantom material used was gelatin and was chosen due to its mention in literature such as [94]. Gelatin is a solid substance derived from the collagen inside animals’ skin and bones. Specifically, Knox brand gelatin was used which is derived from pork products. The packaging states that one envelope containing the equivalent of 15 mL of gelatin powder will set a 500 mL volume into a liquid state or 375 mL into a more solid state. Increasing the concentration of gelatin increased the stiffness of the resultant solid. In addition, gelatin that has set into a solid is also transparent to sound and as such the addition of a sonic scattering material was necessary for its use as an ultrasound phantom.

The procedure for making these phantoms is described as follows. Firstly, 1 L of distilled water was brought to a boil and continued to boil for 30 minutes. This was done to degas the water. Once the water was degassed, 100 mL of it was poured into a separate beaker on a heater. The heater kept the water just below the temperature of a vigorous boil. The desired amount of gelatin powder was then added to the water and the mixture was transferred off the heat and onto a magnetic stirrer. The mixture was transferred between the heating element and the stirrer until it appeared that all of the gelatin had been dissolved. At this point, the beaker was placed back on the stirrer for the final time and the desired amount of carbon particles were added to act as ultrasonic scattering particles. The entire mixture was allowed to air cool while stirring until it began to set. Once setting began, the mixture was poured into a mould and the magnetic stirrer was removed. The mixture in the mould was then covered with saran wrap and placed in a refrigerator where it was left for at least 24 hours in order to completely solidify.

This phantom seemed to provide a better analog to human tissue than the silicone phantom. The speed of sound through the material was within the acceptable range and a similar stiffness to that of human tissue was obtained by adding 3 g of Knox gelatin to every 100 mL of water. However, gelatin phantoms also had some drawbacks. Firstly, there was the recurring issue of air bubbles. Although steps were taken to degas the mixture as much as possible, air bubbles still formed within the phantom.

Secondly, due to the density of the water-gelatin mixture, many of the heavier carbon particles settled to the bottom of the phantom during solidification. This problem was worsened by the large amount of time required for the gelatin to fully solidify. This resulted in a very non-uniform distribution of carbon particles which was the major flaw of the gelatin phantoms and the reason why this type of phantom was not extensively used during research.

6.1.3 Agar Phantom

The final material used to create a phantom was agar. It was chosen due to its mention in literature [95], [96] and its similarities to and differences from animal gelatin. Agar is similar to gelatin in that it has similar physical properties, but it is derived from seaweed instead of animal products. Agar is a gel at room temperatures and remains in this state up to temperatures as high as 65 ºC. The melting temperature of agar is 85 ºC. The agar used was obtained from BioShop and is of laboratory grade.

Agar was chosen as the material to make the majority of phantoms used during research. This decision was made because the speed of sound through agar is within the acceptable range. In addition, its stiffness and speed of solidifying allowed for the creation of phantoms with a near uniform distribution of carbon particles and with a stiffness that seemed very similar to the touch of biological tissue. The following section discusses the specifics of the ultrasound scattering particles used and gives a detailed description of the procedure developed to create a phantom from agar powder.

A graphite powder of carbon particles was used to scatter ultrasonic signals within the phantom. The specific powder used was number 10129 supplied by Alfa Aesar. The particle size distribution is as follows: 10% 6.813 µm, 50% 26.03 µm and 90% 50.33 µm. It was experimentally determined that 3 g of graphite powder provided the most uniform distribution of carbon particles and as such, the most useful resultant RF signals for our research. Assuming a uniform distribution of carbon particles with a size in the ninetieth percentile of 50.33 µm, it was calculated that there were approximately 2 particles per ultrasonic wavelength which resulted in a scattering echo from any location within the phantom. Therefore, a concentration of 3% by weight of carbon particles was adopted as the standard for all phantoms to follow.

There are many mentions of agar being used in literature. However, there is no standardized, recorded reference to one specific procedure used to create a useful phantom from agar powder. The following is the procedure developed and used throughout this thesis to create human analog phantoms for our research using the equipment at our disposal. There is room for improvement in the creation of these phantoms and as such future work should be done in this area. The procedure required: agar powder, carbon powder, water, a beaker, a kettle, a small pan, a magnetic stirrer, a heating source, a refrigerator, a scale and a mould. The mould was constructed in the shape of a cube using overhead transparencies and clear adhesive tape. The general shape adopted had a 5 cm x 5 cm base and was up to 8 cm tall.

The first step in the procedure was to degas the water. In order to do this, a kettle full of distilled water was brought to a boil on a heating element. Once vigorously boiling, the kettle was left to continue to boil for an additional 30 minutes during which time the desired amount of carbon and agar powders were portioned out using the scale. At this point, 100 mL of boiled water was poured into the glass beaker. The kettle was then removed from the heat and replaced by the small pan. The heat was turned down to medium and enough water was added to the pan to ensure that the beaker would float when placed into the pan. The glass beaker was then placed into the small pan. As opposed to placing the beaker directly on the heating element, the purpose of placing the beaker into the small pan containing water was to avoid burning the agar once it was added to the mixture. Finally, a large pot of very cold water was prepared. The exact amount and temperature of this water was not important. This cold water was used to rapidly cool the agar-water-carbon mixture in a later step. Therefore it was only required to have enough volume to partially submerge the mould and be of a low enough temperature to quickly bring down the heat of the mixture.

After the completion of the preceding preliminary steps, the procedure below was followed:

1. Place the beaker on the magnetic stirrer and place the stir rod into the beaker.
2. Turn the stirrer on at a medium stir rate.
3. Slowly add the agar powder to the water. It is essential that the powder is added slowly enough to avoid clumping. It may be necessary to stop pouring and wait for the agar that has already been added to be fully mixed into the solution. In addition, it is important that the temperature of the mixture remains above 65 ºC. The addition of agar must stop and the beaker must be placed back into the small pan on the heating element if the temperature of the mixture becomes too low.
4. Remove the beaker from the stir platform and place it into the small pan on the heater once all of the agar has been added. The temperature of the heater should remain hot enough to ensure that the water in the small pan continues to boil.
5. After about 60 seconds of heating or enough time to bring the temperature of the mixture above 85 ºC the beaker should be placed back onto the stirrer.
6. Stir until the temperature begins to drop to a value near 65 ºC.
7. Continue steps 4-7 until all of the agar has fully dissolved into the water.
8. Slowly add the carbon particles to the mixture while continuing to stir. Again, as in step 3, do so slowly to avoid clumping and stop to re-heat the mixture if the agar begins to solidify.
9. Once all of the carbon has been added and thoroughly stirred, replace the beaker into the pan on the heat for 60 seconds of heating or enough time to bring the temperature of the mixture back above 65 ºC.

10. Remove the beaker from the heat and place it back on the stirrer. Turn down the speed of the stirrer until it is just barely moving. This can be accomplished by turning the stirrer off, and then gradually increasing the stir velocity until the stir rod just begins to rotate smoothly. Leave the mixture on the stirrer at this rate to cool. This step will continue to stir the liquid until it begins to solidify. The end of this step is marked when the liquid becomes viscous enough to stop the stir rod.
11. Pour the mixture into the mould making sure to pour slowly and steadily enough to ensure that no air bubbles are formed. It is necessary to ensure that only the liquid be poured into the mould. Make sure that the stir rod remains behind in the beaker.
12. Place the filled mould immediately into the cold water. The stirring done in step 10 has ensured an even distribution of the carbon particles and rapidly cooling the mould in the water hardens the mixture quickly. This decreases carbon particle settling and will result in a very uniform distribution of particles in the final product.
13. After 3 minutes in the cold bath remove the mould from the water and cover it with saran wrap.
14. Place the saran wrap covered mould into a refrigerator and leave it to set for a minimum of 24 hours.

The steps outlined above comprise the procedure used throughout this thesis to create the phantoms used. Precise numerical calculations of the stiffness of the phantoms were not done in this thesis. However, the stiffness could easily be compared tactilely to that of human tissue. Using this method of comparison, it was found that the useful range for agar powder was between 1% and 3% by weight. It was found experimentally that below 1% agar by weight a solution was created that was in between a solid and liquid state. The solution seemed to be in a form of sludge which proved to be useless as a tissue phantom.

By tactilely comparing a number of created phantoms to various living human tissue it was found that 1 w% agar had a similar stiffness to that of fat whereas 3 w% agar was stiffer and resembled contracted skeletal muscle tissue. A concentration of agar of 2% by weight was found to resemble relaxed muscle tissue. By varying the percent of agar between 1 w% and 3 w% a wide range of human tissue analog phantoms could be created. Although the 1 w% - 3 w% variation in agar affected the stiffness, it did not seem to push the velocity of sound propagation outside the acceptable range. A more detailed characterization of phantoms should be conducted for research in the future.

The created phantoms were kept in a refrigerator wrapped in saran wrap when not in use. Experimentally, it was found that the useful lifetime of an agar phantom was between 10 and 25 days when stored properly. After 25 days, the phantoms dried up and would fall apart when handled during experimental procedures. The phantoms had to be handled with extreme care even when within their useable lifetime. Although the agar provided phantoms with the closest relation to human tissue, they were very fragile. This was most noticed when dealing with the very soft phantoms produced with 1% agar by weight. A photograph taken during measurement of a 1% agar by weight phantom can be seen below in Figure 6.1. The phantom is black in colour due to the carbon powder that was added as ultrasonic scatterers.

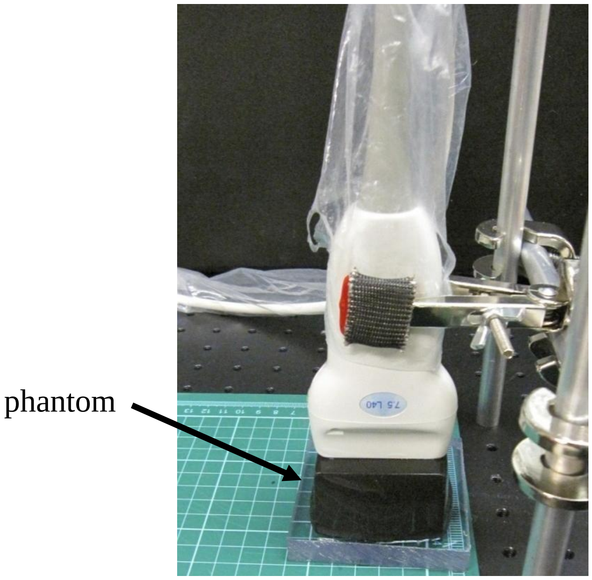

Figure 6.1 Biological tissue phantom made from agar. This phantom was made with 1% agar by weight and was measured on a plexiglas plate with the ultrasonic probe seen above.

6.1.4 Phantom Simulated Skeletal Muscle System

A system to simulate the skeletal muscle environment during in vivo experiments needed to be designed once a method had been developed for producing phantoms of varying stiffness. As mentioned in Chapter 5, it was assumed that during in vivo experiments three physically and categorically different materials would be encountered over depth by an ultrasonic beam. These, in order from shallowest to deepest, are fat, muscle and bone.

Fat is the softest of the three materials. It was represented by a layer of 1% by weight agar phantom. The muscle layer was modeled with either a 2% or 3% by weight agar layer depending on whether the particular experiment required the study of relaxed or contracted muscle. The bone layer was modeled with a layer of plexiglas. Plexiglas is similar to bone in that it is uncompressible and will reflect a sound wave strongly at its boundary due to the acoustic impedance difference between it and the tissue mimicking agar layers.

The overall simulation system was comprised of a thin layer of the fat phantom followed by a thicker layer of the muscle phantom stacked on top of plexiglas used to simulate bone. This simulation system of an in vivo skeletal muscle environment proved to be effective and was to our knowledge the first of its kind used to model ultrasonic muscle measurements. A diagram of the simulation system accompanied by a corresponding acquired RF signal can be seen in Figure 6.2 below. It can be seen that the large peaks in the RF signal correspond to the various interfaces in the simulation environment.

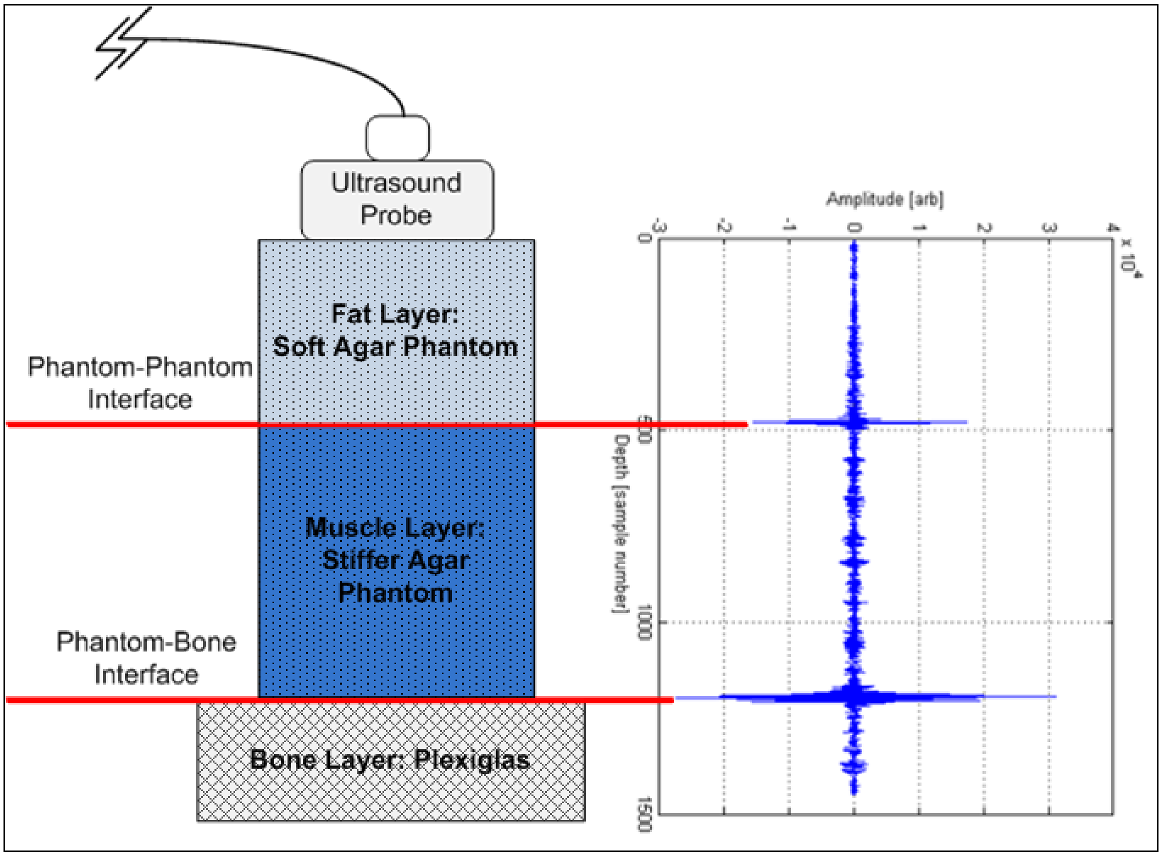

Figure 6.2 Schematic diagram of a phantom simulated skeletal muscle environment with a corresponding acquired RF ultrasound signal.

6.2 Experimental Design and Procedure

An experimental procedure was developed after designing the simulation environment with respect to the phantoms used. Two different experimental procedures were designed. The first was used for experiments having to do with strain estimation. The second had to do with those experiments used to simulate muscle contraction. The following section outlines the experimental design and procedure for both strain estimation and muscle contraction simulation experiments.

6.2.1 Strain Imaging

Strain is a measure of the deformation experienced by a material. It is relevant to muscle measurements as it is possible that injured tissue areas may experience a change in their stiffness. The general method with which strain was calculated is outlined in Chapter 4 and the specific method used for strain measurements in this thesis is described in the following sections. The purpose of this section is to outline the experimental procedure used to obtain data with the purpose of measuring strain.

The concept of calculating strain requires that a change in displacement has occurred. In addition, the technique of quadrature demodulation used to measure displacement from the received ultrasonic signal requires that no phase shift between consecutive temporal samples (i.e. frames) exceeded 2π radians. These two details were the reasoning behind the development of the experimental methodology.

In order to calculate strain, a specific sequence of pressure was applied on the object being imaged during the ultrasonic signal acquisition. Assuming that an object is deformable, any external force applied on the object will result in its deformation. This deformation is the result of a displacement that can be used to calculate a measure of relative strain. Strain can be calculated between any two time instances if a displacement has occurred. However, because of quadrature demodulation there is a limit on the magnitude of the phase change between two temporal samples. In order to make sure that this phase magnitude limit was not exceeded, a procedure of gradual force application was used for the strain measurement experiments.

The procedure was developed such that the first third of the data in time, or about 2 seconds, corresponded to no applied external force. This was actually practically impossible because the application of some force with the ultrasonic probe was required in order to obtain a good coupling between the probe and the object being imaged. The probe was applied to the object with as little force as possible to obtain good coupling and this small force was used as the baseline for all other forces which allowed it to be treated as if it were nonexistent. After the first third, or 2 seconds of data acquisition, a gradual linear increase in force over time was manually applied. Finally, during the remaining third or the last two seconds of data acquisition, a constant force was maintained.

In practice, the first and last thirds of the acquired data were treated as pre and post-stress states and were used for strain calculations. The middle third of the data was practically used to experimentally verify that the phase shift between two consecutive temporal samples remained under the 2π radian limit. A demonstration of the ideal force applied by the transducer on the object being imaged can be seen in Figure 6.3 below.

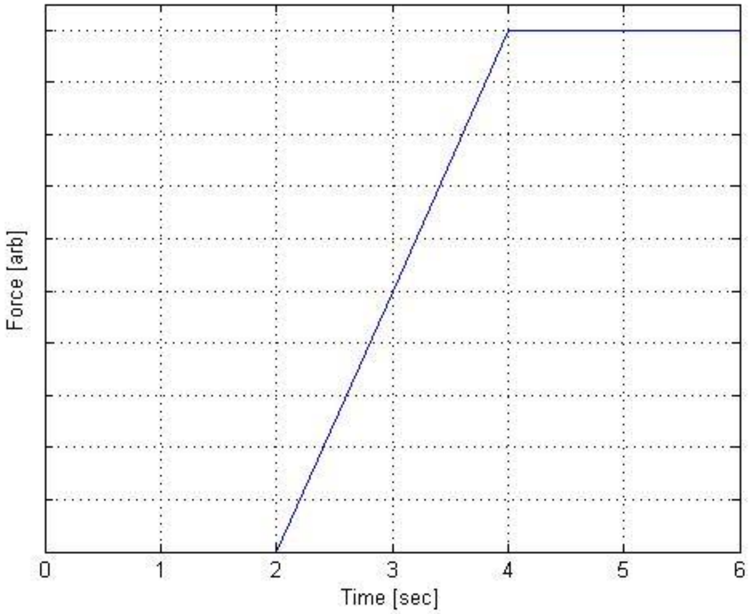

Figure 6.3 Force applied by probe during strain measurement experimental procedure.

6.2.2 Muscle Contraction Simulation

The second type of experiments that needed to be simulated had to do with measuring muscle contractions. This environment needed to simulate an electrical muscle stimulator (EMS) applied to a skeletal muscle. The EMS allowed for the direct stimulation of a muscle with variable pulse repetition frequency and voltage. A simulation system was, therefore, designed to allow variation of simulated stimulation frequency and amplitude. The following section outlines the design of the hardware and experimental procedure followed to collect simulated muscle stimulation data using phantoms.

6.2.2.1 Hardware Development

A number of in vivo experiments were done in order to study actual muscle contractions so that a realistic simulation system could be designed. Some of the in vivo experiments done are explained in the following chapter. In all experiments done, muscle contractions forced by the EMS appeared to look like pulses in the demodulated phase or displacement as calculated from the received RF signal. This observation allowed for the design of a hardware system that is outlined below.

Aside from the shape of the displacement waveform it was also necessary to ensure that the simulator was comparable to the properties of actual muscle contraction. The muscle layer is located between a fat layer and a bone layer. Therefore, it was important when designing the simulation environment, to take the location of the source of the simulated muscle contraction into account. The overall concept of the hardware set-up was to use a motor and cam to press against the phantom periodically. In order to decrease wear on the phantoms themselves, a sheet of thin flexible plastic was placed in between the phantom and the rotating cam. The cam would then strike the flexible plastic, pushing it into the phantom which caused a pulsatile deformation of the phantom.

A block diagram and a photograph of the simulation system with and without a phantom present can be seen in Figure 6.4 and Figure 6.5, respectively. A gear motor provided the mechanical motion used to simulate muscle contraction. The motor itself supplied about 0.4 N·m of torque at a rate of 58.8 rpm when supplied a voltage of 6V. To vary the simulated pulse frequency, various attachments or cams were placed on the output shaft of the motor. These cams, each having a different number and size of contact points, would come into contact with the flexible plastic causing the phantom to deform. Increasing the number of contact points increased the pulse repetition frequency. The magnitude of the force applied was varied by adjusting the distance of the cam from the flexible plastic being displaced. The magnitude of the simulated muscle contractions increased as the distance between the cam and the flexible plastic was decreased.

A rig of wood and aluminum was used to hold both the ultrasonic probe and the phantoms in place. This was done to fix as many of the experimental variables as possible. The aluminum pieces of the rig were joined together with metal clamps. These clamps provided the most significant source of error with respect to the hardware configuration. This was due to the fact that the nature of their construction allowed for a few millimetres of motion to occur between the clamps and their supporting rods. Future work on a more stable support system should be done to eliminate this source of error. One solution could be to employ a set of computer controlled mechanical stages.

In order to avoid lateral movement of the object being imaged, the bottom plexiglas section of the phantom simulating bone was adhered to the rig. In addition, another piece of plexiglas was used to hold the agar phantom layers against the flexible plastic wall. The ultrasonic probe was held in place by a rubber tipped nickel clamp. The entire rig was bolted onto a large metal work table. The legs of the table were placed on rubber pads in order to decrease any external vibration or environmental noise that could have interfered with experiments.

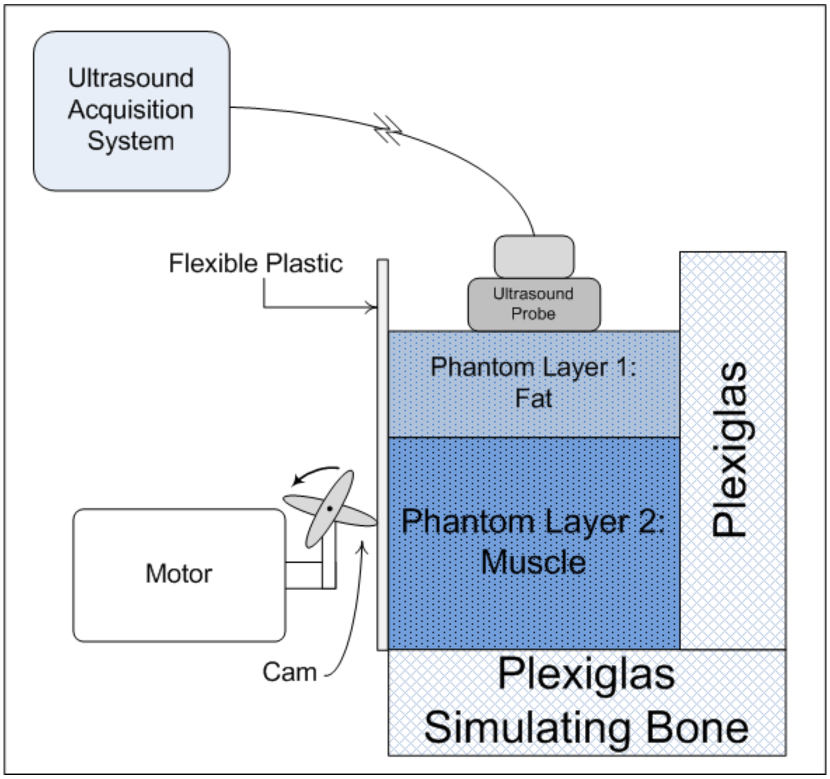

Figure 6.4 Hardware block diagram.

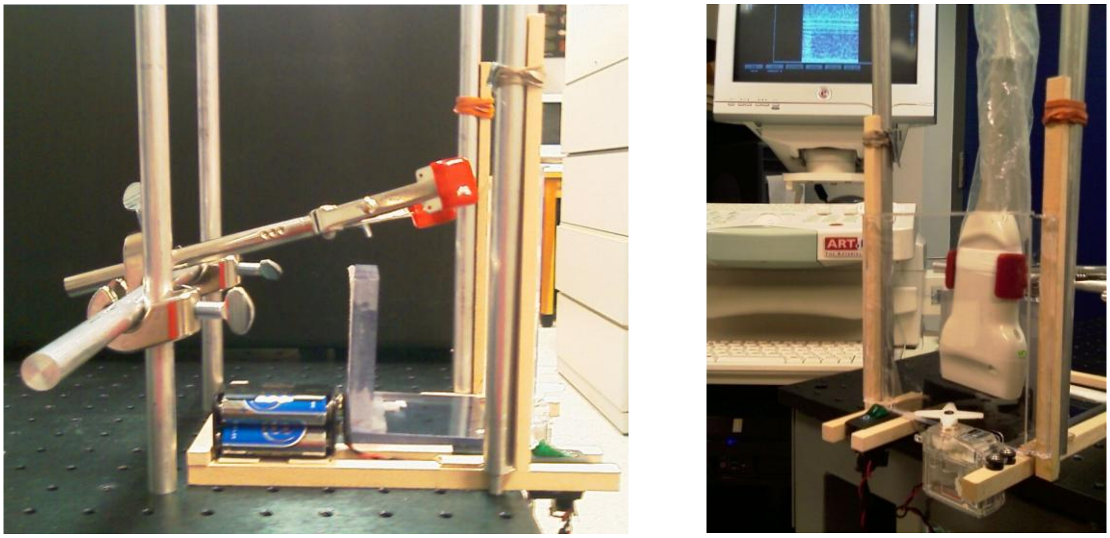

(a) (b)

Figure 6.5 Photograph of simulated muscle stimulation hardware. It can be seen: (a) with no phantom present and (b) during an experiment with a phantom present. The ultrasound machine can be seen in the background.

6.2.2.2 Experimental Procedure

The goal of the simulation environment was to provide experimental results similar to those seen in vivo experiments described in Chapter 7. For this reason, the experimental procedure had to also mimic the one used during in vivo experiments. Therefore, the experimental procedure used with this system was similar to the methods described in Chapter 5 and the in vivo procedure used that will be discussed in the following chapter.

A reference section of data was collected and used for the depth scaling required by the motion artefact removal algorithm. This was practically done by pushing down on the aluminum rod holding the clamped ultrasonic probe so that it applied a force on the object being imaged. Then, after a brief period of inactivity, the motor was turned on and the muscle pulse simulations began. For all tests mentioned to follow a four pronged cam was used. This attachment had a distance of 3.7 cm between any two directly opposite contact points. It resembled a symmetrical ‘plus sign’ shape. Attaching this particular cam to the output shaft of the motor rotating at 58.8 rpm resulted in a simulated stimulation pulse rate of 3.92 Hz which is referred to as the 4 Hz vibration or mechanical stimulation for the remainder of this chapter.

6.3 Experimental Results

The completion of a hardware simulation system allowed for a large number of simulation experiments to be done. Each experiment brought more insight into the physical properties seen and methods used to analyze acquired data. The simulation environment was also used to test constructed phantoms in order to ensure that they met all requirements necessary for experimental use. The following section discusses and displays strain imaging and muscle contraction simulation concepts and results. In addition, an accuracy evaluation applied to phantom studies analyzing many performance related aspects of signal acquisition and processing is presented.

6.3.1 Strain Imaging

Strain estimations can be acquired with some data processing whenever a displacement has occurred. Therefore, when measuring internal motion, it is possible to obtain a strain estimate. However, it should be noted that obtaining accurate strain estimations is not the overall goal of this thesis. Rather, the following section serves as an introduction of how simple strain images can be obtained from displacement signals. These images demonstrate the validity of including strain imaging modalities in a muscle motion system and as such, identify a need for future research. The concepts of strain estimation and calculation are detailed in Chapter 4. However, specific details as they relate to the actual experimental methods used will be outlined in the following section.

For the purposes of this research, strain images were created such that their results would demonstrate the concepts of strain while at the same time negate the effects of phase jumping. Phase jumping was the major problem faced during this thesis research. It caused unexpected jumps in phase resulting in discontinuous displacement profiles that appeared as if they should have been successive. This phenomenon occurred only with respect to the axial direction (fast time). Phase jumping is described in more detail and a possible cause and proposed solution to the issues it causes are detailed in Section 4.6.2. This phase jumping problem could not be entirely solved and was the limiting factor on the accuracy of the strain measurements. The method used to estimate strain is explained below.

As stated previously, displacement magnitude varies with respect to depth. The manner with which the displacement magnitude varied with respect to depth was used to determine information about the strain experienced within an object. Using the experimental procedure described in Section 6.2.1, a displacement was created. This displacement could be plotted for a specific depth location (axial sample) over all time (in the temporal direction) which resulted in information about the amount of displacement occurring at that specific depth.

The displacement could also be plotted for a specific instant in time (temporal sample), over all depths. This representation showed the displacement magnitude as it varied over depth at that particular instant in time. Due to the fact that the displacement was entirely generated by application of force on the surface of the object, the variation of displacement magnitude with respect to depth demonstrated how different areas of the object deformed with respect to one another. This concept can be converted into strain.

The results of displacement obtained from an M-mode experiment with a single layer agar phantom having a thickness of 20 mm placed on a plexiglas plate are shown in Figure 6.6 below. Figure 6.6 (a) shows the displacement with respect to the temporal direction whereas Figure 6.6 (b) provides displacement with respect to depth. Notice how in Figure 6.6 (b) the displacement magnitude increases with respect to depth up until about 20 mm. This location corresponds to the interface between compressible phantom and incompressible plexiglas. The reason the displacements shown are negative is because the probe was pushed down into the phantom. This resulted in a shrinking of the phantom which corresponds to motion of the scatterers towards the probe. As defined in Section 4.1, motion in this direction has been denoted with a negative displacement whereas motion in the opposite direction is represented by positive displacement. Therefore, the sign of the displacement represents direction and has nothing to do with the quantity of motion.

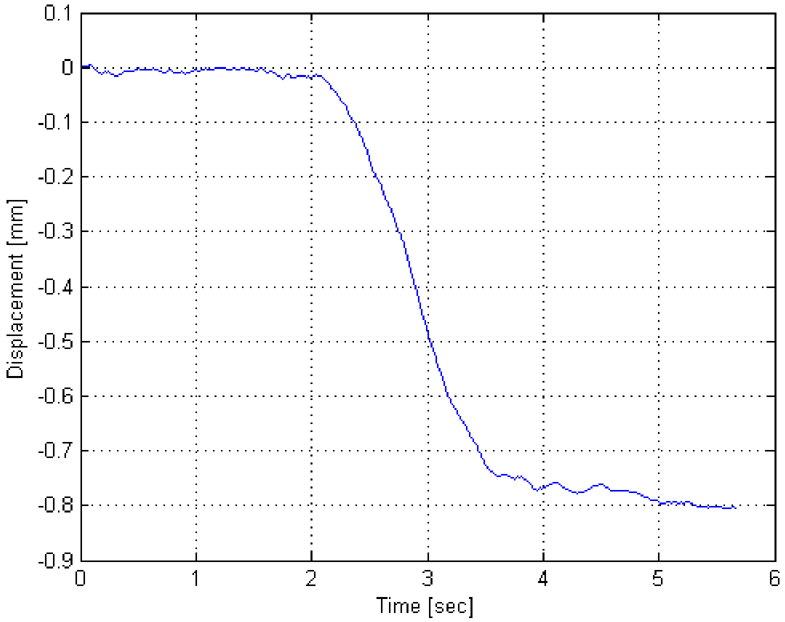

(a)

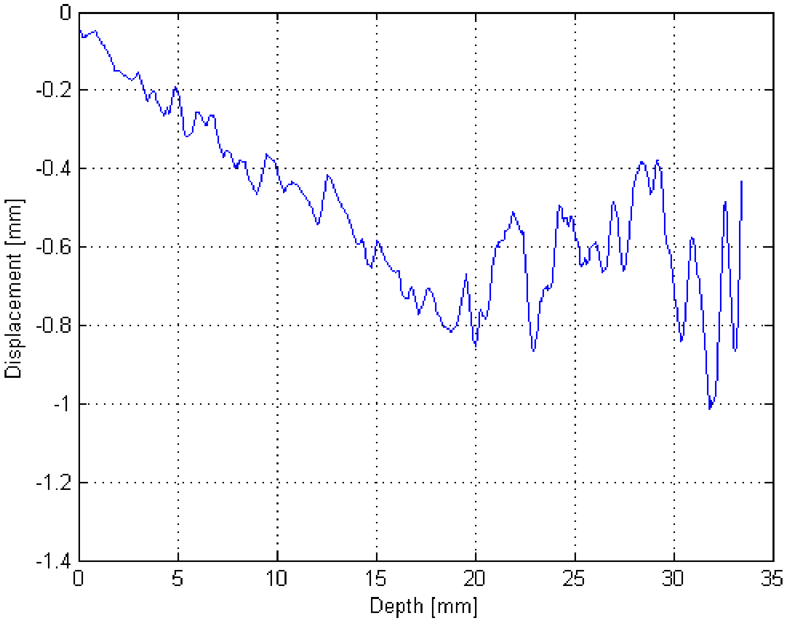

(b)

Figure 6.6 Displacement measured during single agar layer phantom strain experiment. The displacement is shown: (a) vs. time at an observation depth of about 18.5 mm and (b) vs. depth at a time instant of about 5.67 seconds.

In order to obtain strain measurements, estimated values of the slope of the displacement vs. depth signal were required. As stated in Section 4.5 an estimation of the slope within an axial region from points a to b defined by $n_{ab} = [a, b]$ is equivalent to the axial strain, $\varepsilon_z(n_{ab}, m)$, in that region as

$$\varepsilon_z(n_{ab}, m) = \frac{\Delta L_{ab}}{L_{ab}} \tag{6.1}$$

where L_{ab} is the original distance between points a and b and ΔL_{ab} is the resultant distance between them as caused by the displacement of the points a and b after the application of stress.

This equation provided the reasoning behind estimating the slope of the displacement vs. depth plot in order to estimate strain. The method of quadrature demodulation ensured that measurements of displacements occurred with respect to a fixed depth. This meant that there was a fixed distance between the ultrasonic probe and any depth sample throughout all time. Therefore, the distance from the probe surface to any given depth sample corresponded to the denominator of Eq. 6.1 and the numerator of Eq. 6.1 was equal to the magnitude of the displacement that had occurred at this depth. These two quantities are equivalent to the independent and dependent axes of a displacement vs. depth waveform, respectively. An estimation of the slope of this signal is, therefore, analogous to an estimation of the strain versus depth. A large slope corresponds to a high strain which represents a relatively soft material. Conversely, a small slope represents a low amount of strain which corresponds to a relatively stiff material. This concept is displayed in Figure 6.7 and Figure 6.8 below.

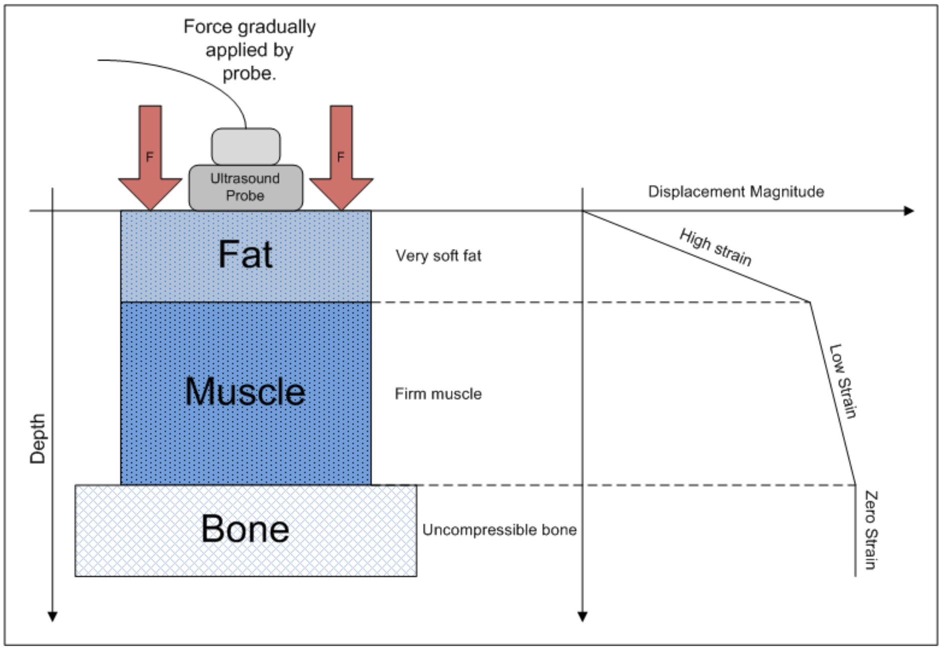

Figure 6.7 Displacement measured vs. depth corresponding to strain.

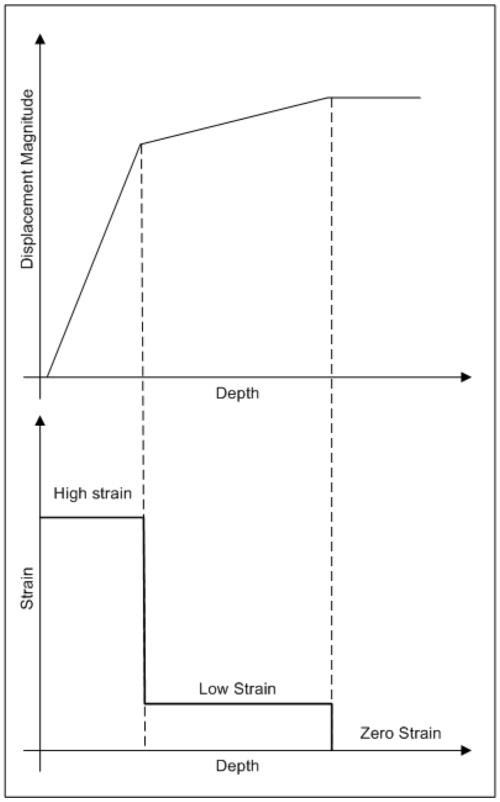

Figure 6.8 Ideal relationship between slope of displacement vs. depth profile and strain.

The process used to practically determine the above and all other strain related results was as follows. Firstly, the demodulated phase was averaged two-dimensionally in both time and depth to lessen the effect of phase jumping and other noise. An averaging window with a size of 21 sample points or about 0.5 mm in depth and 11 sample points or 0.01 seconds in time was used. Strain was then calculated based on a comparison of the slope of the displacement versus depth estimation.

The slope comparison was done based on boundary echo tracking and a least squares linear fitting estimation. The windowed peak tracking algorithm used to track interface boundaries was similar to the echo tracking used by the bone boundary algorithm presented in Section 5.6. However, in the strain imaging algorithm both the interface between different phantom layers as well as between phantom and plexiglas layers were tracked as peaks in the baseband envelope signal. These tracked peaks corresponded to the boundaries between different materials and defined the endpoints of the various regions present in any given imaged area such as fat, muscle or bone.

The value of strain within any given region was then equated to the least squares estimated value of the slope within that region. A flowchart outlining the described strain estimation procedure can be seen below in Figure 6.9. In this way, an image could be created showing the average strain within the detected regions of an object. An example of an M-mode strain image can be seen in Figure 6.10 below.

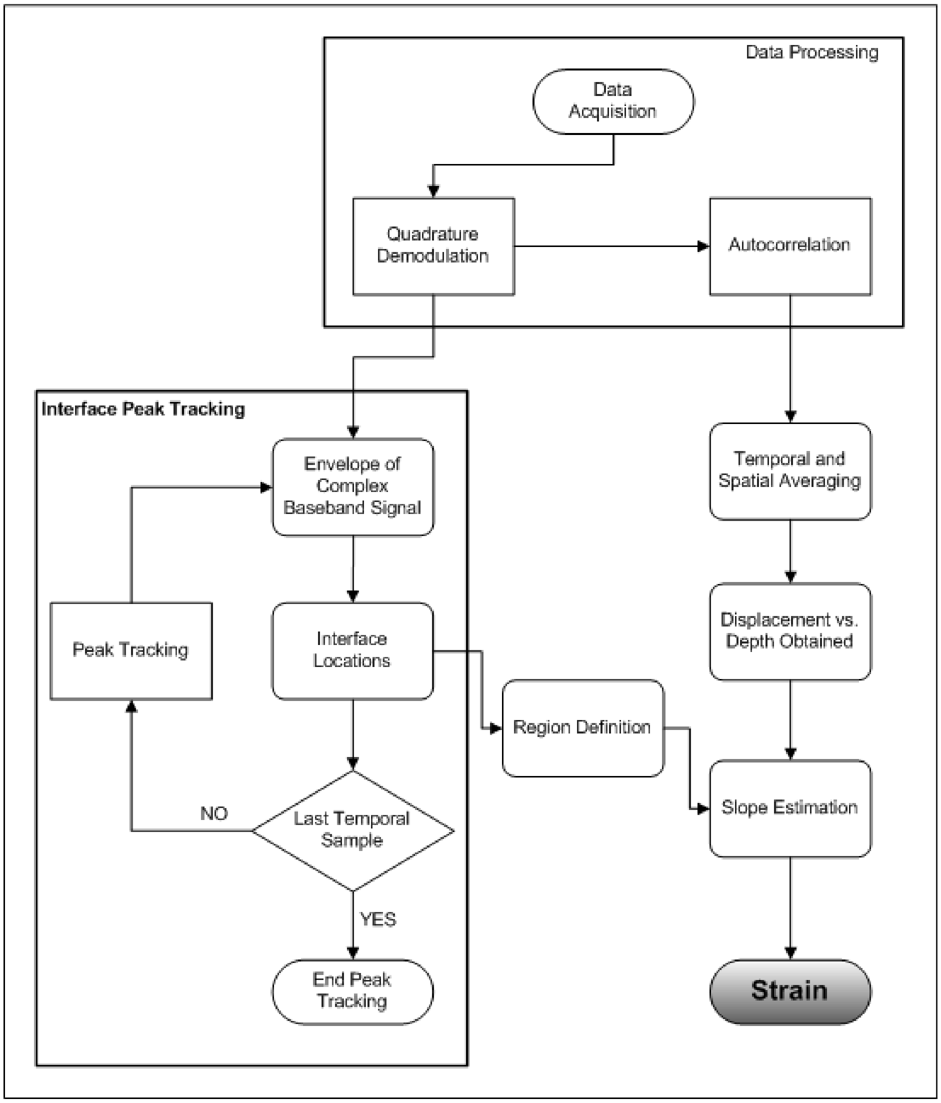

Figure 6.9 Flowchart of strain estimation procedure.

Once the strain estimation procedure had been defined, strain images and estimations could be obtained using the phantom simulation environment described above. A number of similar experiments were done with a number of different phantoms and configurations. The following are results of both M-mode and B-mode strain images and their accompanying strain and displacement profiles. It should be noted here that strain is expressed as a percentage. It is a relative measure based on the material being imaged and the amount of displacement occurring. It is used to analyze the relative differences between areas imaged during the same experiments or under similar experimental conditions. A quantitative measure of stiffness such as elastic modulus can be obtained from the percentage strain. Its calculation has been left as future work.

6.3.1.1 Single Agar Layer Phantom Simulations

The first results shown are for a phantom environment containing an approximately 20 mm thick sample of 3 w% agar phantom on top of a thick plexiglas plate. The imaging modality used was M-mode and the estimated displacement signals can be seen above in Figure 6.6. The following figure shows the corresponding strain image. It should be noted that because the strain image was generated based on M-mode data, it is dependent on time (temporal direction). The strain imaging experimental procedure explained above in which force is gradually applied was used to generate these experimental results. Therefore, in the first portion of the image no strain is present because no force and therefore no displacement occurred. As time progressed, more force was applied which caused more displacement and as a result higher strain levels were observed later in time in Figure 6.10.

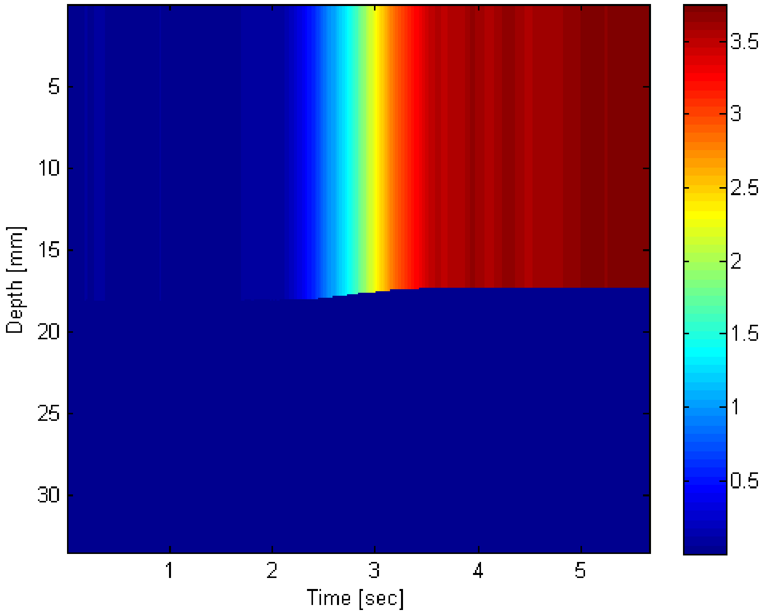

Figure 6.10 M-mode strain image of single layer 3 w% agar phantom. The colour scale corresponds to percentage of strain. The phantom is about 20 mm thick and the phantom-bone interface can be seen after compression at an approximate depth of 18 mm.

The following results shown in Figure 6.11 and Figure 6.12 were obtained from an experiment on an approximately 11 mm thick phantom with 1 w% agar. The imaging modality used was M-mode. Due to the fact that similar forces were applied in both the 3 w% and 1 w% agar experiments, a comparison of their strains is warranted. As such, it can be seen that the 1 w% agar phantom experienced significantly more strain than the 3 w% phantom. This particular 1 w% phantom experienced over double the strain of the 3 w% phantom under similar stresses and therefore it can be assumed that the 1 w% phantom is significantly less stiff than the 3 w% phantom.

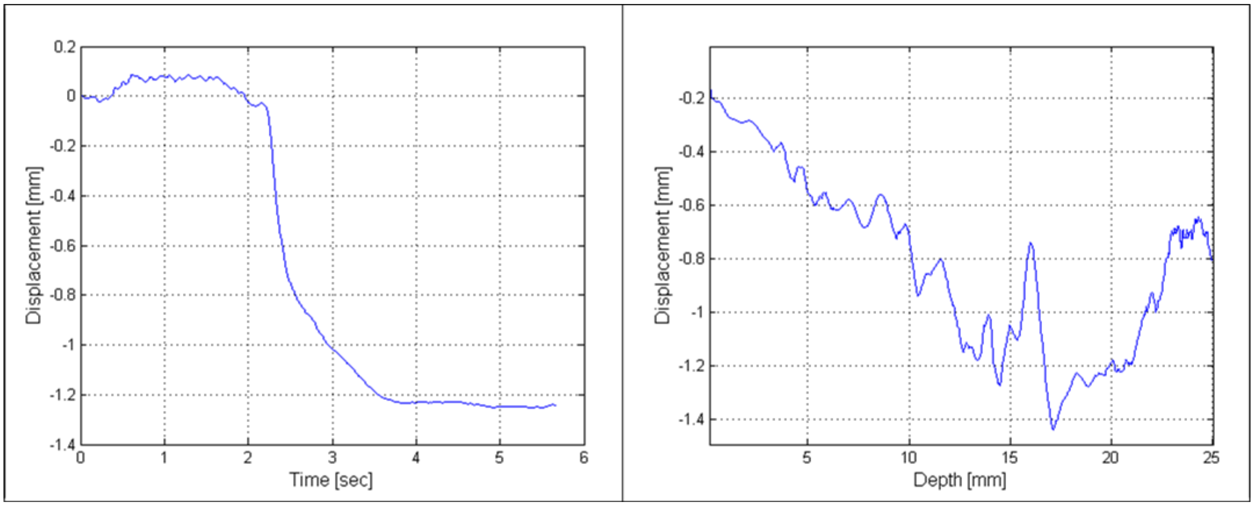

(a) **(b)**

Figure 6.11 Displacement profiles from single layer 1 w% agar phantom. The displacement is shown: (a) vs. time at an observation depth of about 5 mm and (b) vs. depth at a time instant of about 5.7 seconds.

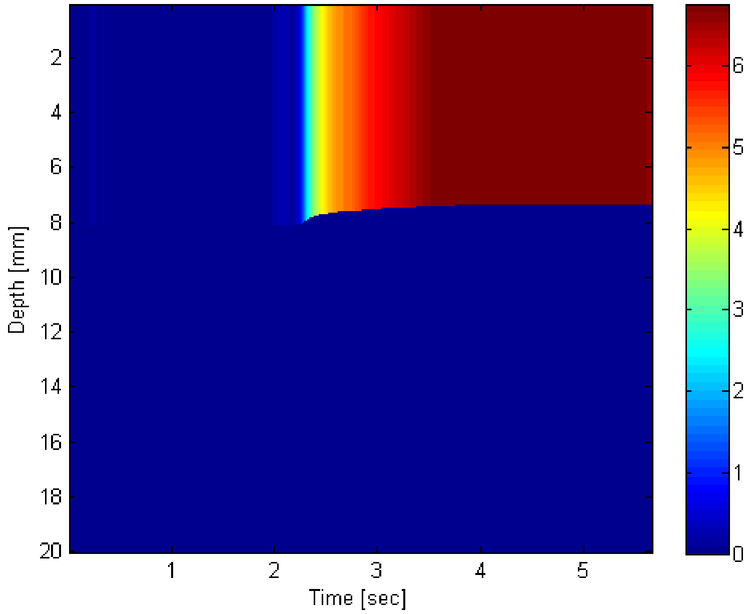

Figure 6.12 Strain image of single 11 mm thick, 1 w% agar phantom. The colour scale corresponds to percentage of strain.

6.3.1.2 Phantom Simulated Skeletal Muscle Simulations

The following phantom simulations were done using three layer phantoms involving different combinations of two layer agar phantoms placed on top of the plexiglas base used to represent bone. The results below in Figure 6.13 (a) and (b) were obtained using a simulation environment with an approximately 10 mm thick top layer of 1 w% agar followed by about a 15 mm thick sample of 2 w% agar. The base was a thick piece of plexiglas. The imaging modality used was M-mode.

It can be seen in Figure 6.13 (b) that the slope appears to be fairly constant throughout the phantom layers. This suggests that the two phantoms have similar stiffness with the top 1 w% agar layer being slightly softer than the bottom 2 w% agar layer. This can be verified with the strain image from Figure 6.14 and the strain profile in Figure 6.15 (b) as more strain is observed in the softer 1 w% agar upper layer than in the more stiff 2 w% agar layer. It can also be seen in the strain image that the bone layer appears to have some stiffness. It is known that the plexiglas used to represent bone is uncompressible. Therefore, this apparent stiffness is an example of the error most likely caused by phase jumping. Figure 6.15 (a) is a standard M-mode image of the phantom in which the interfaces between different materials can be seen. Multiple echoes from the plexiglas can be seen deeper than 22 mm.

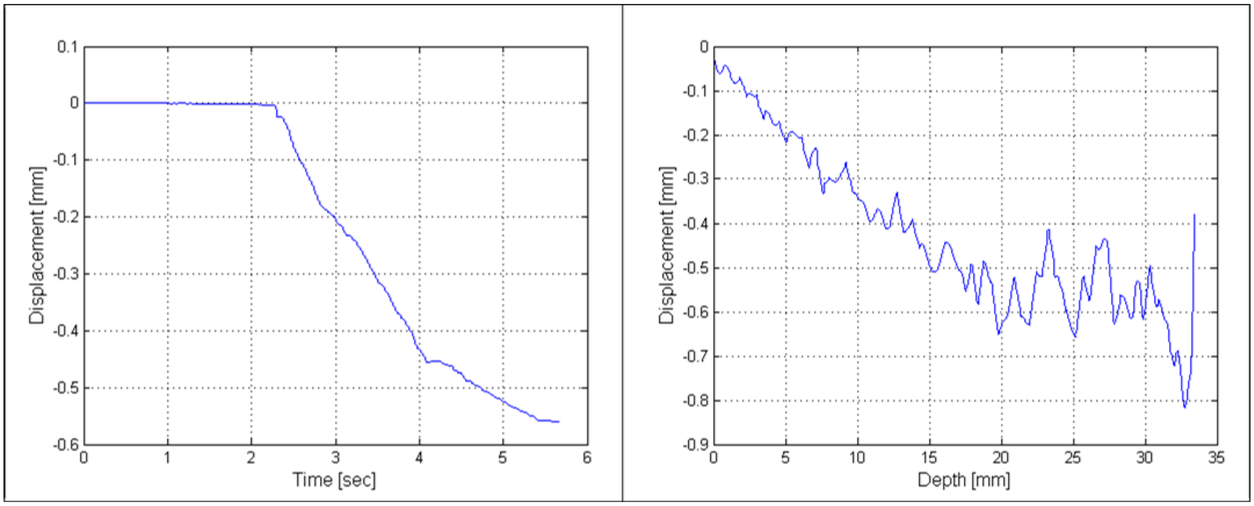

(a) **(b)**

Figure 6.13 Displacement profiles for 1 w% and 2 w% two layer agar phantom. The approximate thickness of the layers was 10 mm and 15 mm respectively. The displacement is shown: (a) vs. time at an observation depth of about 18.5 mm and (b) vs. depth at a time instant of about 5.7 seconds.

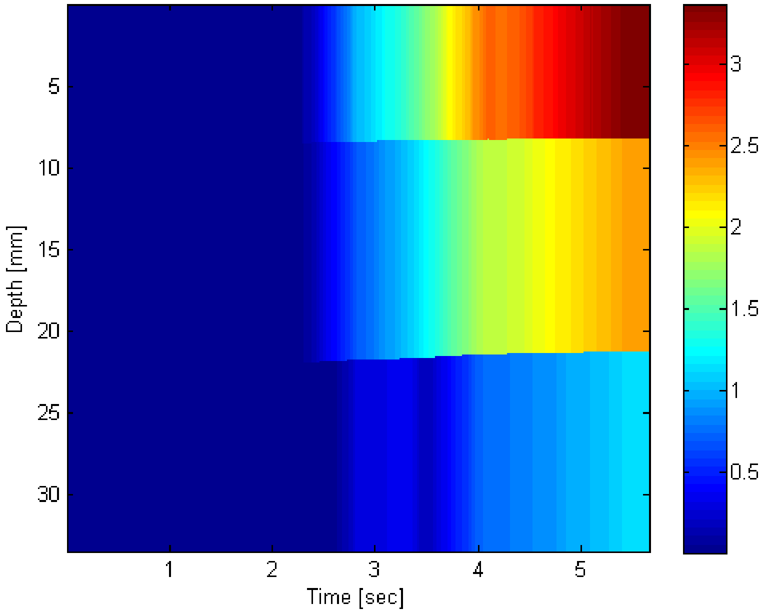

Figure 6.14 M-mode strain image of 1 w% and 2 w% two layer agar phantom. The approximate thickness of the agar layers was 10 mm and 15 mm respectively. The colour scale corresponds to percentage of strain.

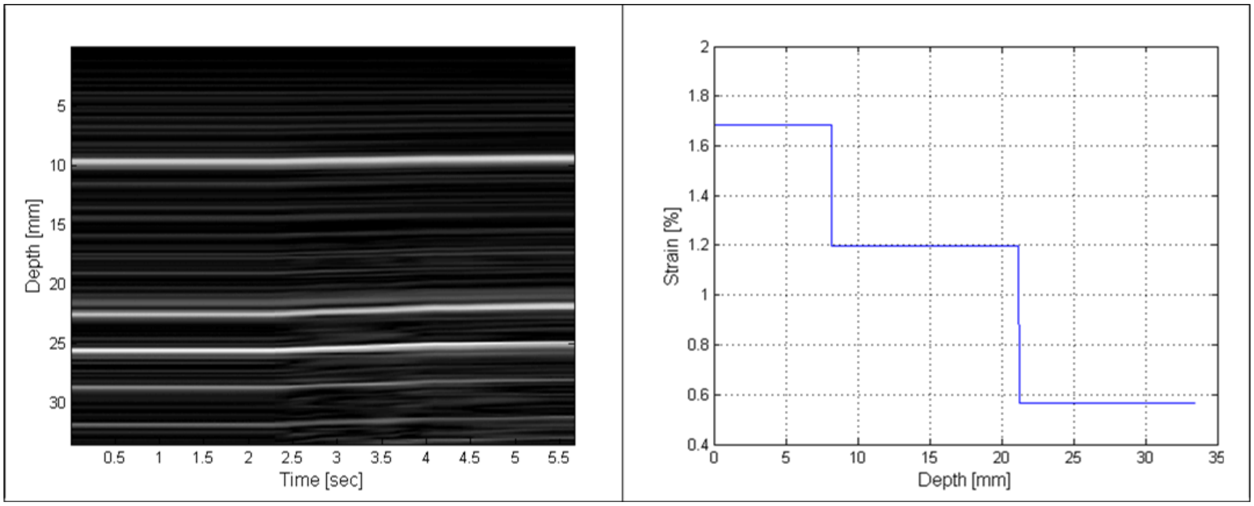

(a) **(b)**

Figure 6.15 M-mode image and strain estimation for 1 w% and 2 w% two layer agar phantom. The approximate thickness of the agar layers was 10 mm and 15 mm respectively. The agar-plexiglas interface is seen in (a) around 22 mm with deeper regions corresponding to multiple echoes. The strain profile is provided in (b) at a time instant of about 5.7 seconds and shows boundaries corresponding to the image in (a).

The next simulation was done in a similar manner to the above simulations. However, the phantom system used had layers that were comprised of 1 w% and 3 w% agar phantoms with approximate thicknesses of about 12 mm and 15 mm respectively. The imaging modality used was M-mode. In the displacement profiles of Figure 6.16 it can be seen that there is a drastic difference between the slope from the 1 w% agar layer and the slope from the 3 w% agar layer. This suggests a large difference between the stiffness of the 1 w% agar and 3 w% agar layers. This difference was verified by the strain image and strain profile plot of Figure 6.17 Figure 6.18 (b). The strain experienced in the 1 w% agar layer is about 18 times larger than the strain experienced in the 3 w% agar layer which suggests that the 1 w% agar layer is a lot less stiff (softer) than the 3 w% agar layer.

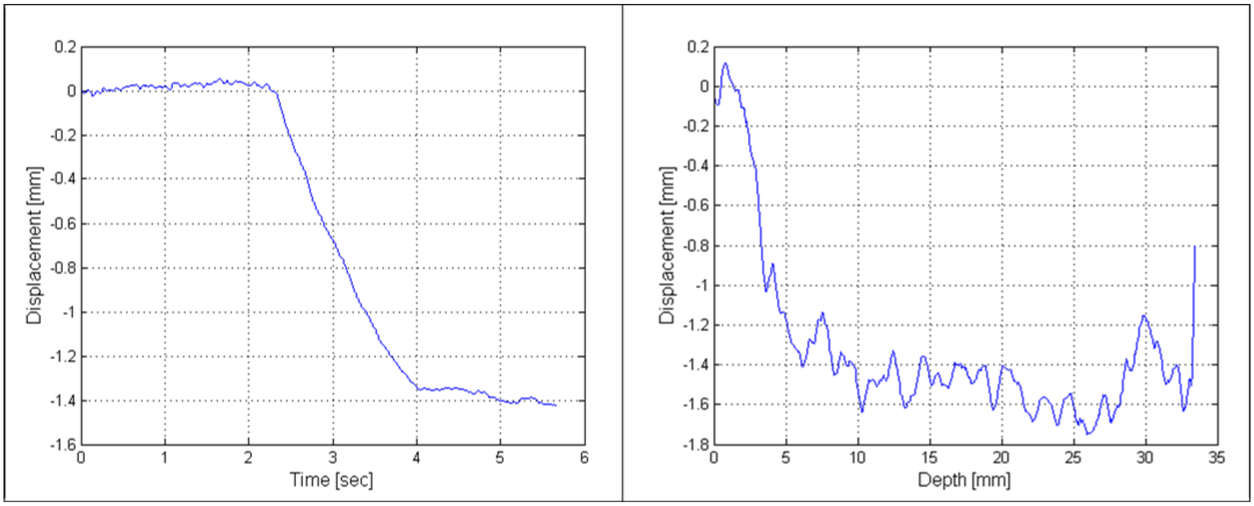

(a) **(b)**

Figure 6.16 Displacement profiles for 1 w% and 3 w% two layer agar phantom. The approximate thickness of the layers was 12 mm and 15 mm respectively. The displacement is shown: (a) vs. time at an observation depth of about 18.5 mm and (b) vs. depth at a time instant of about 5.7 seconds.

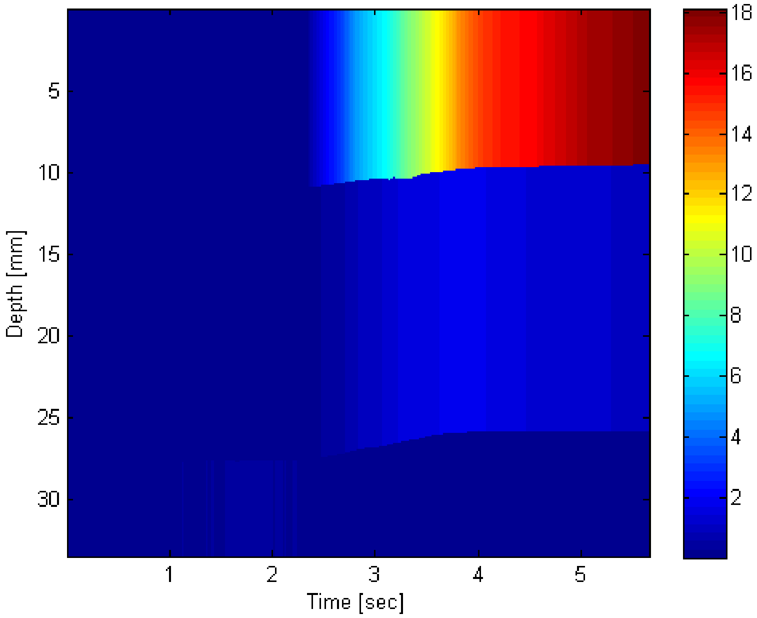

Figure 6.17 M-mode strain image of 1 w% and 3 w% two layer agar phantom. The approximate thickness of the agar layers was 12 mm and 15 mm respectively. The colour scale corresponds to percentage of strain.

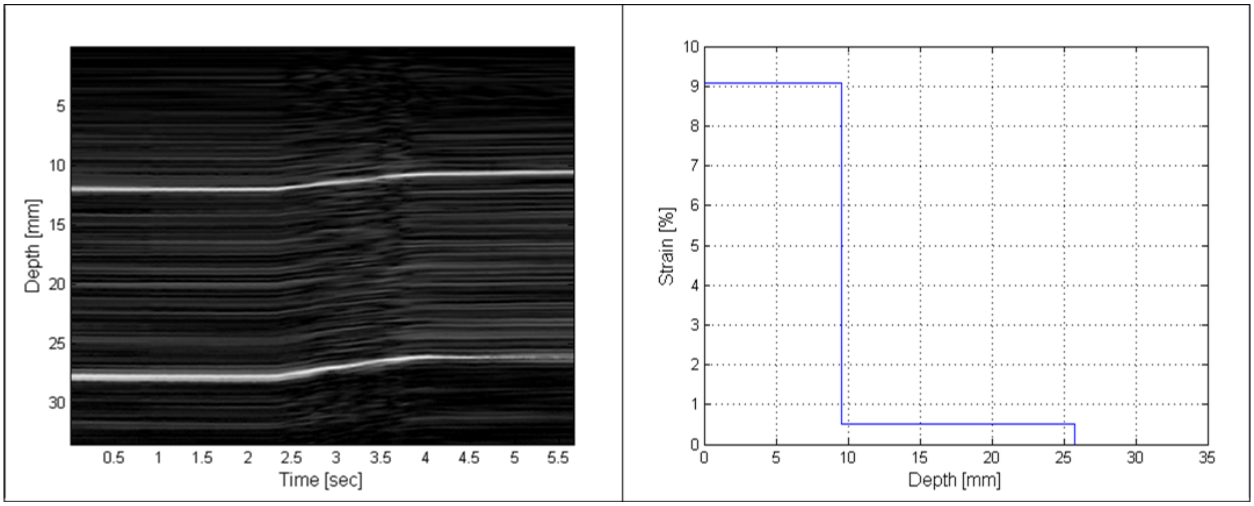

(a) **(b)**

Figure 6.18 M-mode image and strain estimation for 1 w% and 3 w% two layer agar phantom. The approximate thickness of the agar layers was 12 mm and 15 mm respectively. The 1 w%-3 w% agar interface can be seen around 12 mm and the 3 w% agar-plexiglas interface can be seen around 27 mm. The strain profile is shown in (b) at a time instant of about 5.7 seconds and shows boundaries corresponding to the image in (a).

The remaining experimental results shown were obtained using B-mode imaging. In these cases, the x-axis represents lateral position instead of time as in the M-mode images. Therefore, a B-mode strain image produces a cross sectional view of the object being imaged. However, due to the lack of enough memory of the computer used for data analysis, the sampling rate during strain image production had to be reduced by a factor of four. This resulted in a larger phase variation from noise and phase jumping between frames which, in turn, affected the results of the strain estimations.

Future work should be conducted in this area to increase the accuracy in B-mode measurements. However, the results shown still provide a good representation of strain imaging and strain estimation. The following figures are an example of B-mode measurements taken of a simulation system with about a 12 mm thick, 1 w% agar top layer and a 15 mm, 3 w% agar middle layer with a bottom layer of plexiglas.

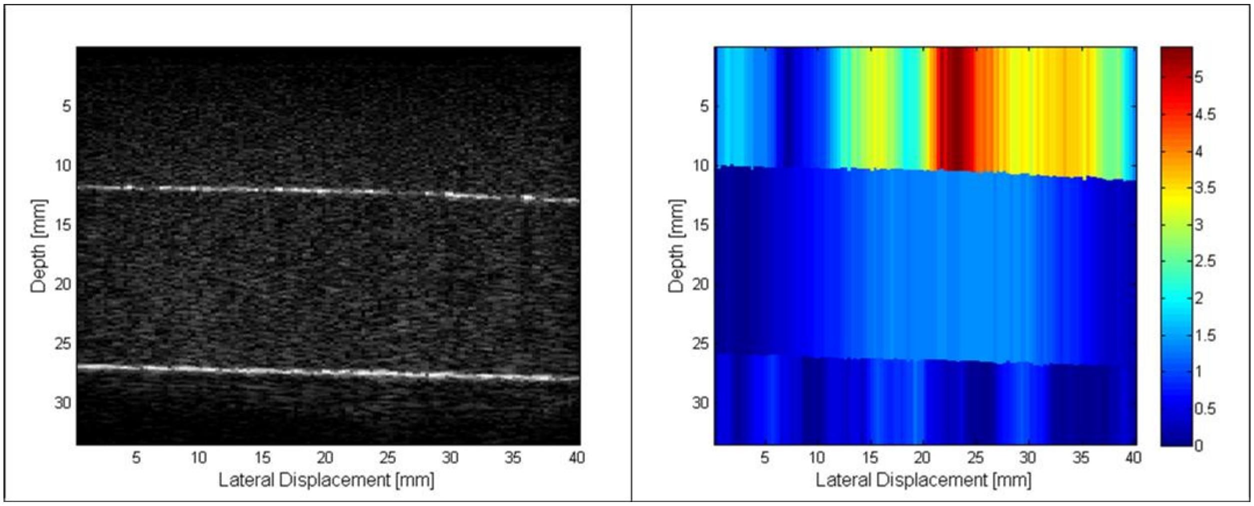

(a) **(b)**

Figure 6.19 B-mode image and B-mode strain image for 1 w% and 3 w% two layer agar phantom. The thickness of the layers was about 12 mm and 15 mm respectively. The colour scale in (b) corresponds to percentage of strain.

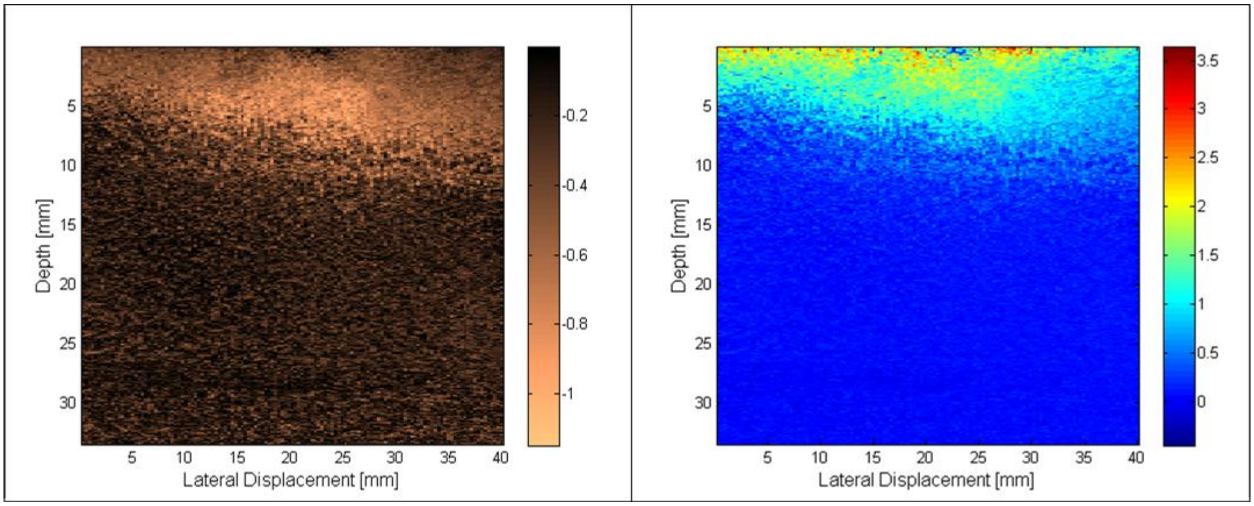

(a) **(b)**

Figure 6.20 B-mode displacement image and instantaneous strain image for 1 w% and 3 w% two layer agar phantom. The thickness of the layers was about 12 mm and 15 mm respectively. The colour scales in (a) and (b) correspond to displacement in mm and percentage of strain, respectively.

Figure 6.19 above provides results very similar to those seen in M-mode strain images such as in Figure 6.14 and Figure 6.17. It shows average strain as calculated with the same methods as previously mentioned. It can clearly be seen that during B-mode experiments, this method results in a much more noisy image. This additional noise is most likely due to the peak tracking algorithm finding slightly different interface locations for each of the lateral samples (scan lines).

Figure 6.20 (a) shows the displacement and Figure 6.20 (b) shows instantaneous strain inside the phantom. The instantaneous calculations were done by estimating the displacement at every depth location instead of the using a line of best fit in a region of depth. Due to the fact that both of these images represent instantaneous quantities, they were more susceptible to error. However, they do provide an idea of the capabilities of B-mode strain estimation. Figure 6.21 below demonstrates a more clear strain image and is the result of averaging the displacement signal over 0.21 mm axially and 0.28 mm laterally before calculating instantaneous strain. This spatial averaging helped to overcome the effects of noise. This strain image seems to show a noticeable transition in stiffness around 11 mm in depth which corresponds with the approximate location of the boundary between the 1 w% and the 3 w% agar phantoms.

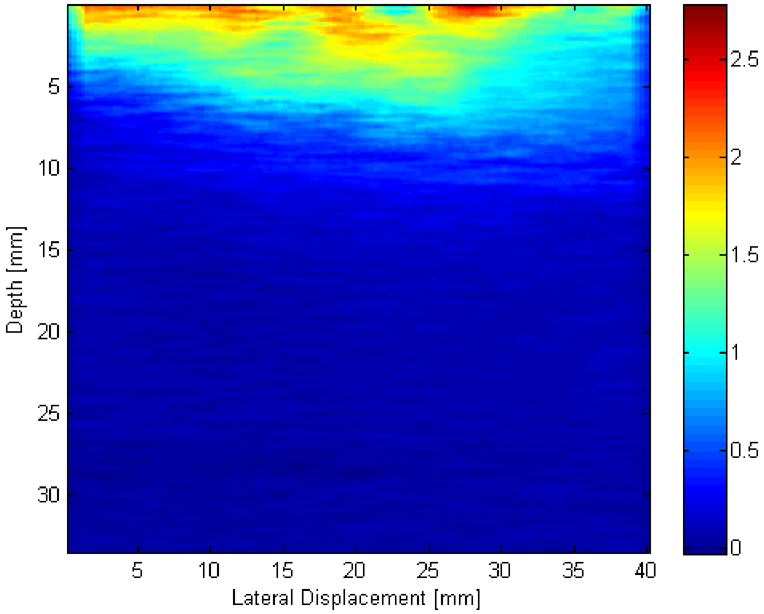

Figure 6.21 Averaged B-mode strain image of two layer 1 w% and 3 w% agar phantom. An averaging window of a size equivalent to about 0.28 mm laterally and 0.21 mm axially was used.

In general, the above results show how stiffness information can be obtained when displacement measurements are available. Although they are only a small sample of what is possible with strain estimation, these results do provide verification and examples of just how useful this type of information can be. These results reinforce that future research should most definitely be done in the area of strain estimation in order to provide a complete tool for analysis of muscle characteristics with ultrasound.

6.3.2 Muscle Contraction Simulation

The next set of simulations were done to analyze muscle motion and used the hardware and procedure described in Section 6.2.2 with both one and two layer phantoms. The following section gives experimental results and analysis of some of the data that was collected. In addition, a demonstration of the use and effectiveness of the bone boundary method for motion artefact removal is provided. It should be noted that motion velocity estimations were obtained by taking the first derivative of the displacement signals with respect to slow time (temporal direction). It can be assumed that the modality used for all displayed results was M-mode unless stated otherwise.

6.3.2.1 Single Agar Layer Phantom Simulations

The first experiment done to demonstrate the muscle contraction hardware simulation involved a single layer of 3 w% agar phantom with an approximate thickness of 19 mm. The agar phantom was placed on top of a piece of plexiglas which was then positioned into the muscle contraction simulating hardware. This was done in such a way that the cam made contact with the phantom about 5 mm from the top of the phantom. The experimental procedure detailed in Section 6.2.2 was employed and a time dependent set of data showing the reference and experimental contraction simulation data can be seen below in Figure 6.22.

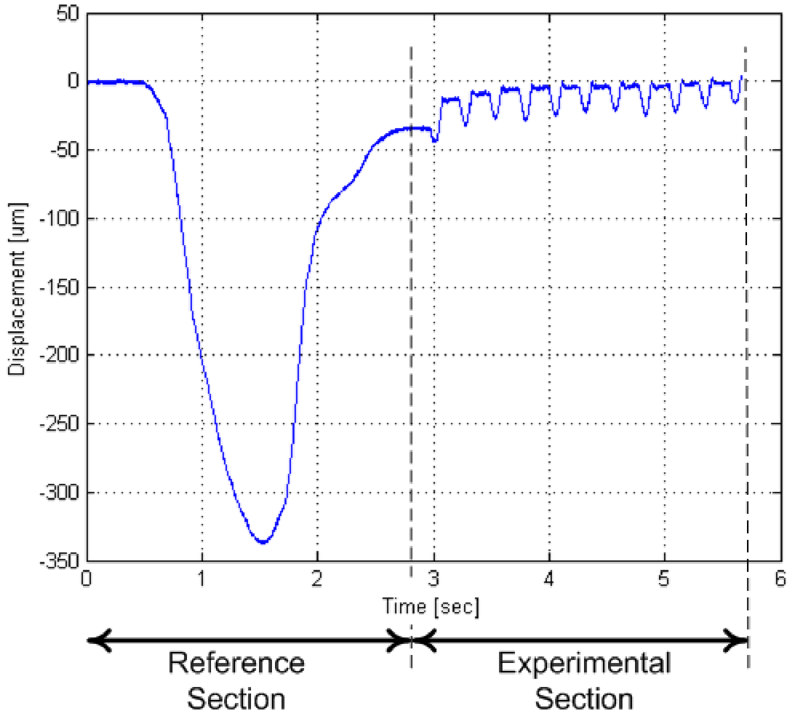

Figure 6.22 Single layer 3 w% agar phantom muscle contraction simulation results showing displacement vs. time. Results observed at a depth of about 6.93 mm.

The results shown below are examples of collected displacement and velocity data of the simulated muscle pulses at a depth of about 6.93 mm. Figure 6.23 below shows the displacement and velocity before the bone boundary motion artefact removal algorithm was applied. Figure 6.24 shows the same results after motion artefact removal has been applied. Care was taken to minimize the probe motion during data acquisition, but it can be seen from these results that some motion did occur. This motion was most likely due to inefficiencies of the clamping system used to secure the probe.

It can be seen from these figures that the magnitude of the displacement of adjacent pulses is not constant. This was an interesting discovery and shows that although each arm of the cam appeared to be the same length as measured with a digital calliper they do in fact differ slightly from one another. This could either indicate that the arms of the cam are different sizes or that the axis of the motor may not be exactly centered on the cam. This difference is easily observed due to the precision of displacement measurements capable using our ultrasonic method. In both cases of before and after motion artefact removal, the 4 Hz vibration is clearly shown in the displacement and velocity profiles.

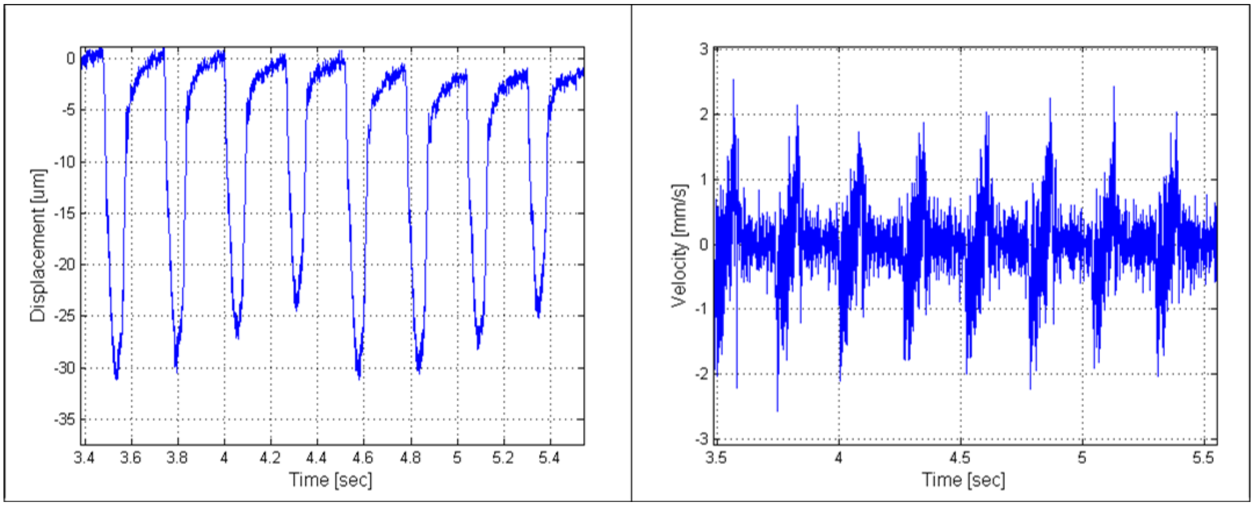

(a) **(b)**

Figure 6.23 Single layer 3 w% agar phantom simulation results showing pre motion artefact removal displacement and velocity vs. time. Observed at a depth of about 6.93 mm.

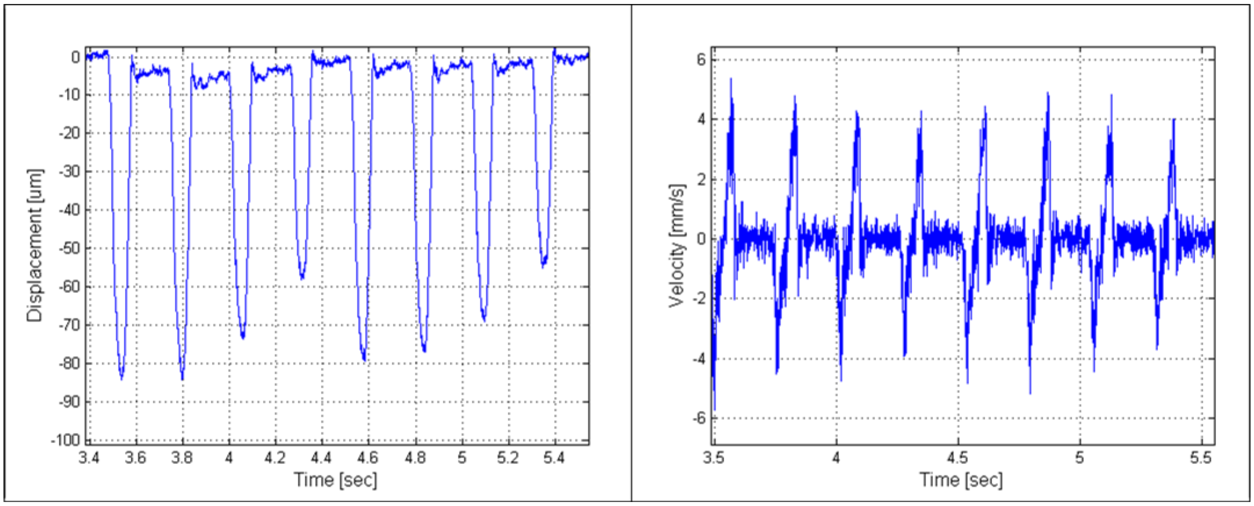

(a) **(b)**

Figure 6.24 Single layer 3 w% agar phantom simulation results showing displacement and velocity vs. time after motion artefact removal. Observed at a depth of about 6.93 mm.

The final result for this experiment can be seen below in Figure 6.25 below which shows a three dimensional representation of the displacement over time for a depth ranging from 0 to 19 mm as measured from the surface of the probe. This depth range was chosen as it corresponded to an area from the surface of the phantom to the phantom-plexiglas interface. This figure shows how the magnitude of the displacement is largest at the location of the pulse origin and decreases in either direction away from this location. Analysis of this graph places the peak displacement magnitude at a depth of 4.83 mm which is consistent with the measured value of the pulse origin at 5 mm as mentioned above.

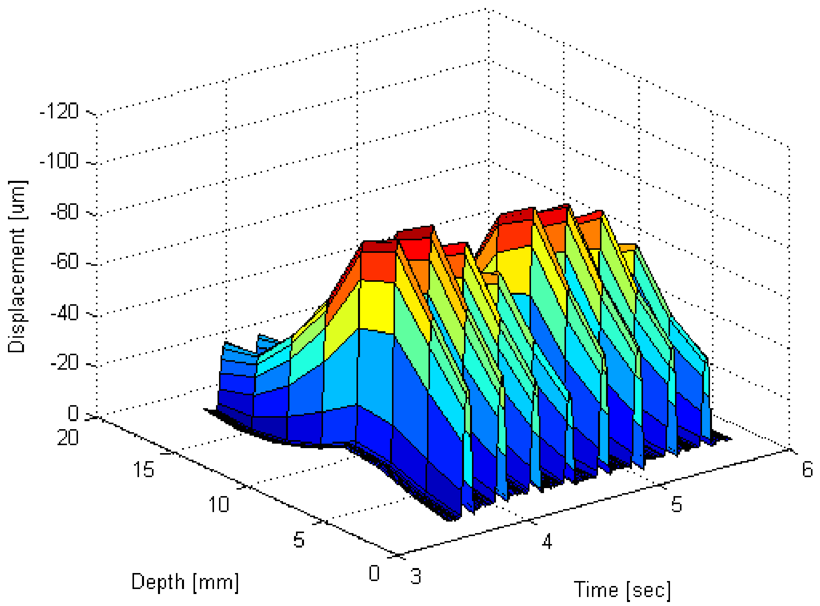

Figure 6.25 Single layer 3 w% agar phantom simulation results showing displacement after motion artefact removal. Observed over a depth range from about 0 to 19 mm and during a time duration from about 3 seconds to 5.66 seconds.

In order to demonstrate the usefulness of the bone boundary method of motion artefact removal, it was applied to experiment data in which probe motion was intentionally induced throughout the experiment. This was done by first obtaining a reference section of data containing only external motion which was then followed by a section of data containing both the 4 Hz vibration and external probe motion. The probe motion was induced by physically pushing on the probe at a varying force and rate. For this experiment, an approximately 19 mm thick, 1 w% agar phantom was placed on top of a piece of plexiglas. Figure 6.26 below shows the resulting displacement before applying the motion artefact removal algorithm along with the scaled bone boundary reference signal used at that depth to remove the external motion. The results in Figure

6.27 and Figure 6.28 demonstrate the displacement obtained before and after motion artefact removal and Figure 6.29 shows the velocity before and after motion artefact removal.

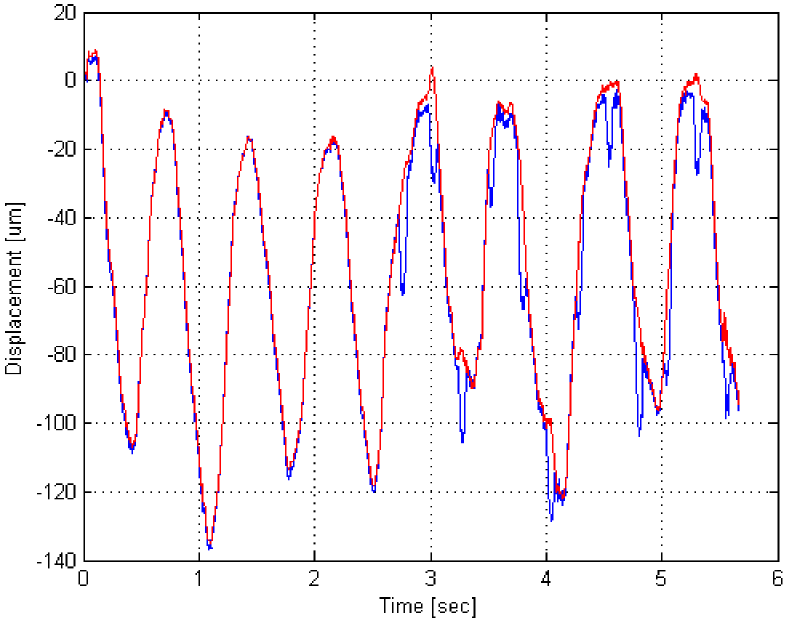

Figure 6.26 Single layer 1 w% agar phantom simulation results showing displacement (blue) and bone boundary signal (red). Observed at a depth of about 15.02 mm.

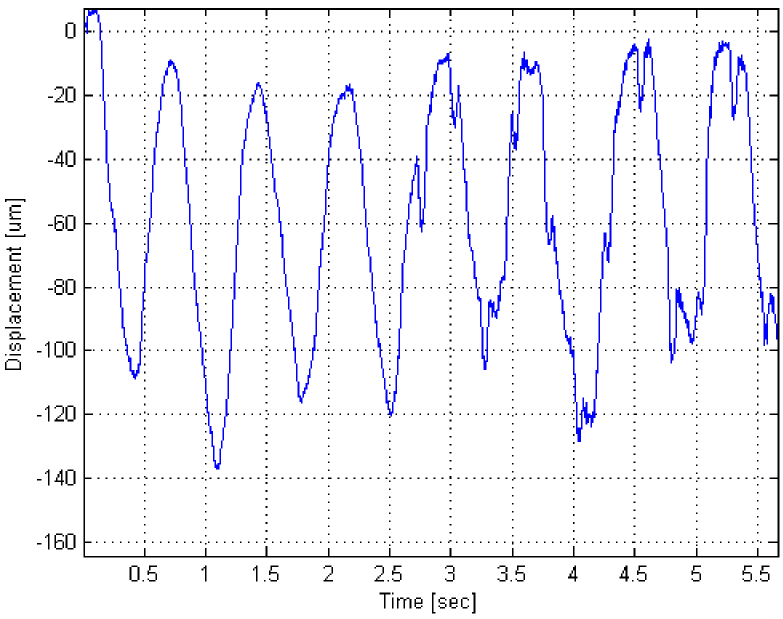

Figure 6.27 Single layer 1 w% agar phantom simulation results showing displacement before motion artefact removal. Observed at a depth of about 15.02 mm.

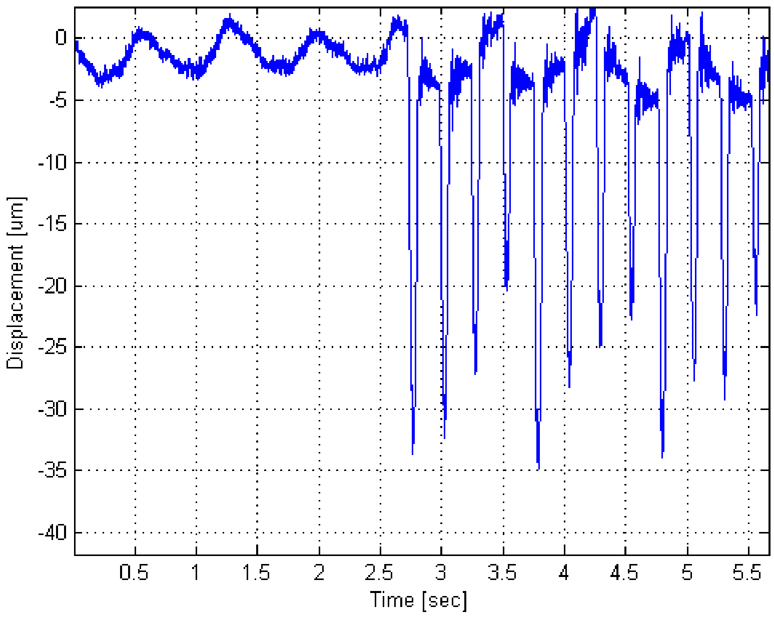

Figure 6.28 Single layer 1 w% agar phantom simulation results showing displacement after motion artefact removal. Observed at a depth of about 15.02 mm.

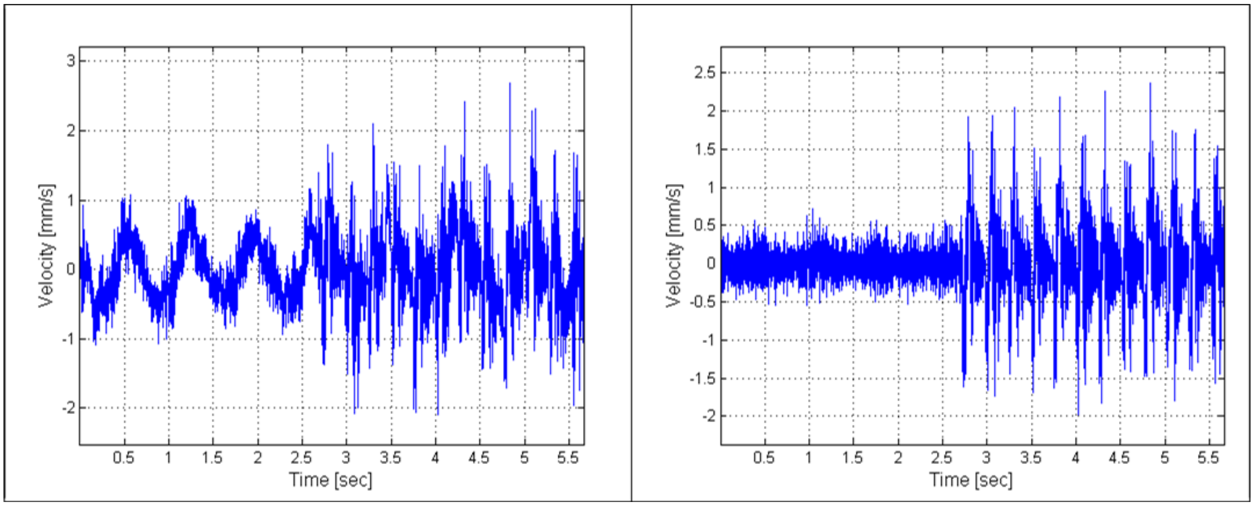

(a) **(b)**

Figure 6.29 Single layer 1 w% agar phantom simulation results showing velocity before (a) and after (b) motion artefact removal. Observed at a depth of about 15.02 mm.

It can be seen from the results above that the bone boundary algorithm has removed a large amount of external probe motion. In addition, the velocity images of Figure 6.30 and Figure 6.31 below show that although noisy, the velocity profile after motion artefact removal clearly shows the 4 Hz vibration whereas it is almost entirely lost in the external motion before it was removed.

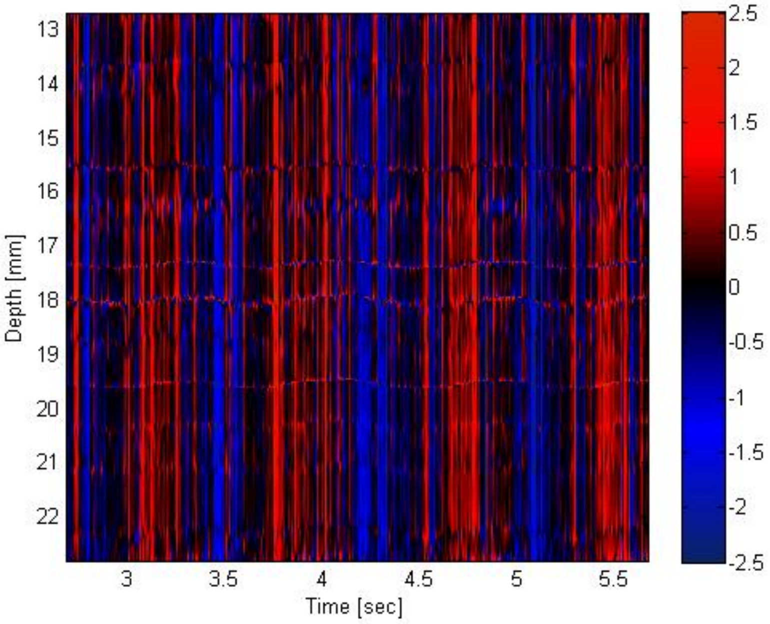

Figure 6.30 Single layer 1 w% agar phantom simulation results showing velocity image profile before motion artefact removal. The colour scale corresponds to velocity in mm/s.

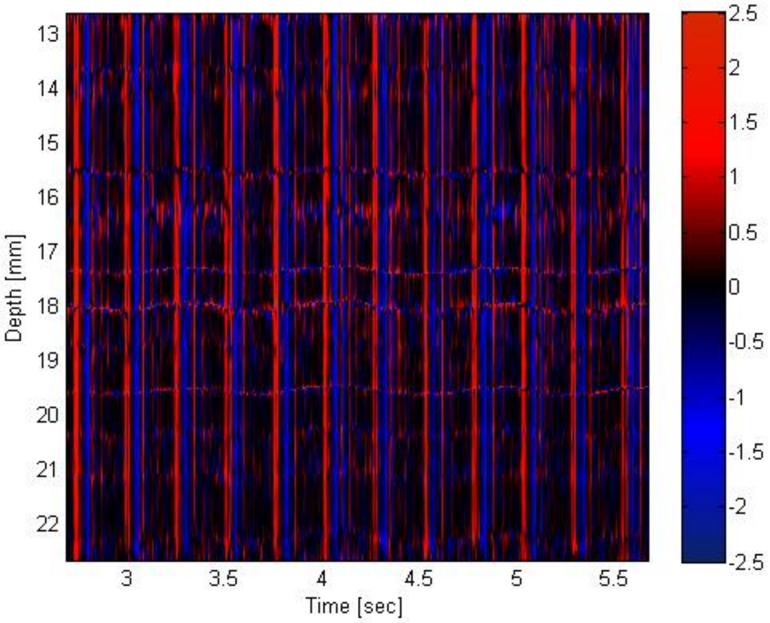

Figure 6.31 Single layer 1 w% agar phantom simulation results showing velocity image profile after motion artefact removal. The colour scale corresponds to velocity in mm/s.

6.3.2.2 Phantom Simulated Skeletal Muscle System Experiments

The following set of experiments were done using the phantom simulated skeletal muscle environment created with two layers of agar phantoms on top of a plexiglas plate. These results were important for the verification of the entire experimental process because they were acquired during simulations that most resembled in vivo experiments. This simulated skeletal muscle system involved two layers of agar followed by a layer of plexiglas to simulate fat, muscle and bone respectively. For this experiment, the fat layer was modeled by about 14 mm thick, 1 w% agar and the muscle layer was represented by about 20 mm thick, 3 w% agar. The mechanical stimulation origin was located in the simulated muscle layer at about 20 mm from the top surface of the fat layer. The following results were gathered with a fixed probe and without intentionally adding external motion. The results of this experiment are given below.

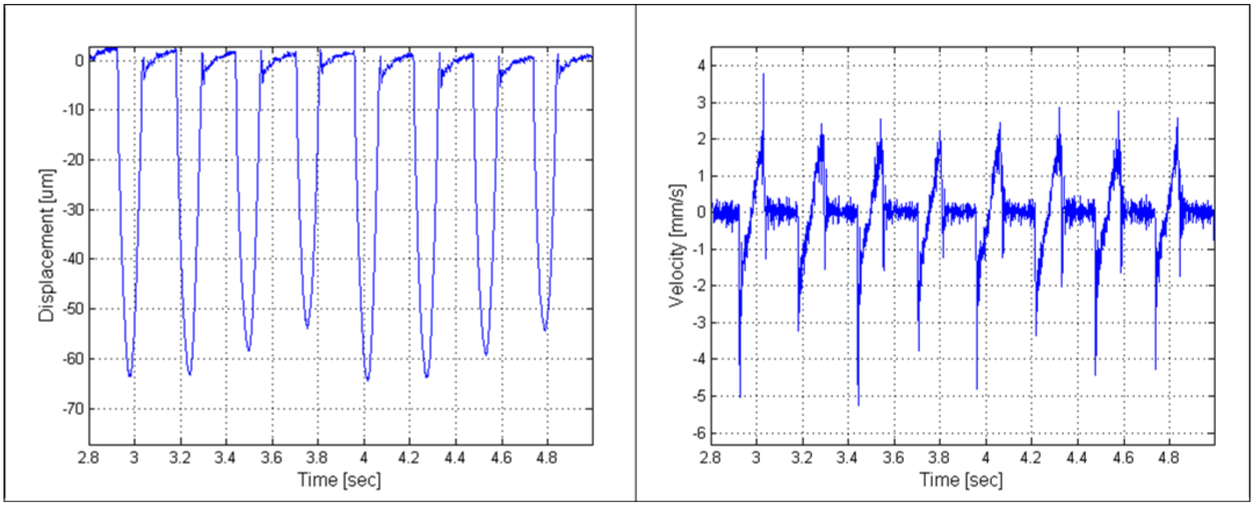

(a) **(b)**

Figure 6.32 Two layer 1 w% agar and 3 w% agar phantom simulation results showing displacement (a) and velocity (b) before motion artefact removal. Observed at a depth of about 18.48 mm.

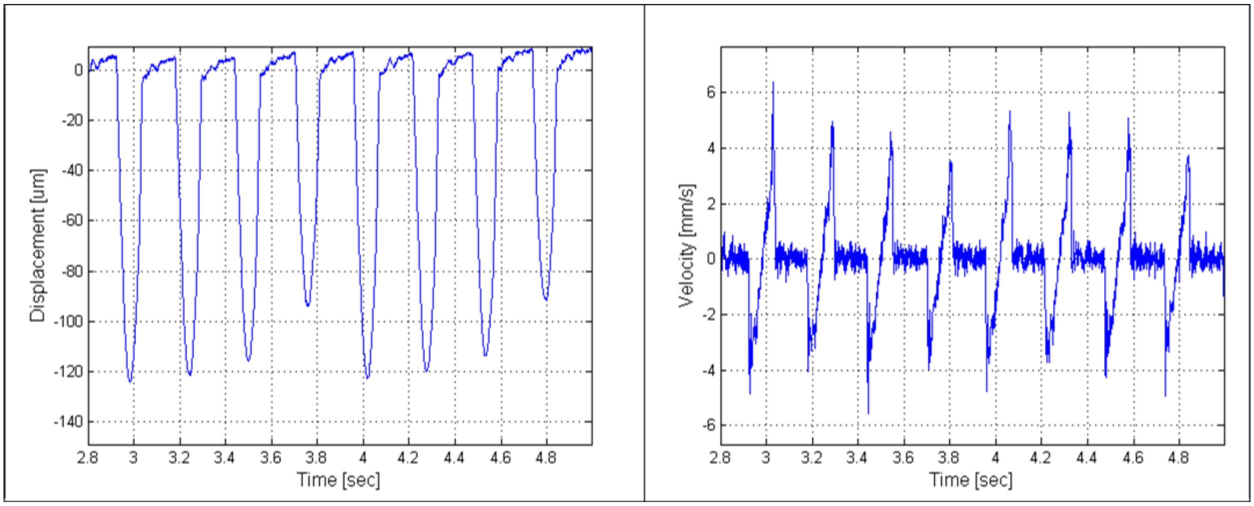

(a) **(b)**

Figure 6.33 Two layer 1 w% agar and 3 w% agar phantom simulation results showing displacement (a) and velocity (b) after motion artefact removal. Observed at a depth of about 18.48 mm.

It can again be seen in the above figures that, as in the single phantom results, the 4 Hz pulse can clearly be observed both before and after motion artefact removal. In this particular experiment no external motion was purposely applied and therefore, the observed motion artefact is most likely due to probe motion within the clamping system.

In Figure 6.34 below, the displacement can be seen over the depth range of both agar layers of the phantom for about 2.5 seconds. This figure shows a local minimum displacement magnitude at a depth of about 13.88 mm which corresponds to the interface between the 1 w% and 3 w% agar phantoms. In addition, local maxima displacement magnitudes are present at depths of 2.98 mm and 18.92 mm. The maximum at 18.92 mm most likely corresponds to the mechanical stimulation origin and is located in the stiffer 3 w% agar phantom layer. The maximum at 2.98 mm is located within the 1 w% agar layer and is probably due to the relative stiffness differences between the 1 w% and 3 w% agar layers as well as the force applied by the probe during measurement.

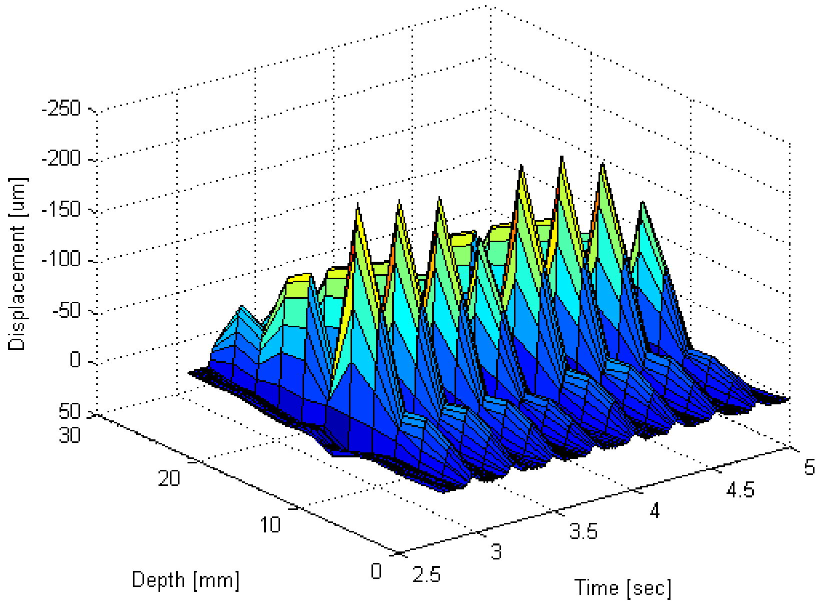

Figure 6.34 Two layer 1 w% agar and 3 w% agar phantom simulation results showing displacement. Observed at a depth range from 0 to 30 mm and during a time duration from 2.5 seconds to 5.66 seconds.

The above experiments were completed with no purposely induced motion artefact present. Therefore, in order to demonstrate the effectiveness of the motion artefact removal algorithm, motion artefacts were purposely added and new results were obtained and are displayed below. The motion artefacts were induced by physically pushing on the probe at a varying force and rate. The same phantom as described above was used having a fat layer modeled with about 14 mm of 1 w% agar and a muscle layer represented by about 20 mm of 3 w% agar. The mechanical stimulation origin was located at about 20 mm from the top surface of the fat layer.

Figure 6.35 below shows a displacement waveform before motion artefact removal was applied along with the scaled bone boundary reference signal used to remove the motion artefact at that depth. Figure 6.36 to Figure 6.39 show displacement and velocity profiles both before and after the motion artefact removal algorithm was applied. It can be seen in these figures that the motion artefact removal algorithm has removed a large amount of the external motion. This allows for the observation of just the internal displacement within the phantom.

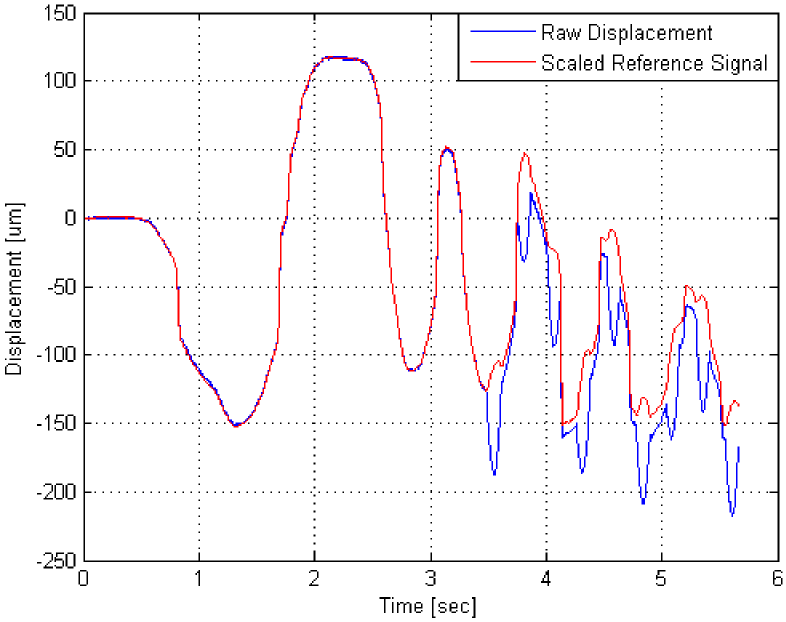

Figure 6.35 Two layer 1 w% agar and 3 w% agar phantom simulation results showing displacement (blue) and bone boundary signal (red). Observed at a depth of about 18.48 mm.

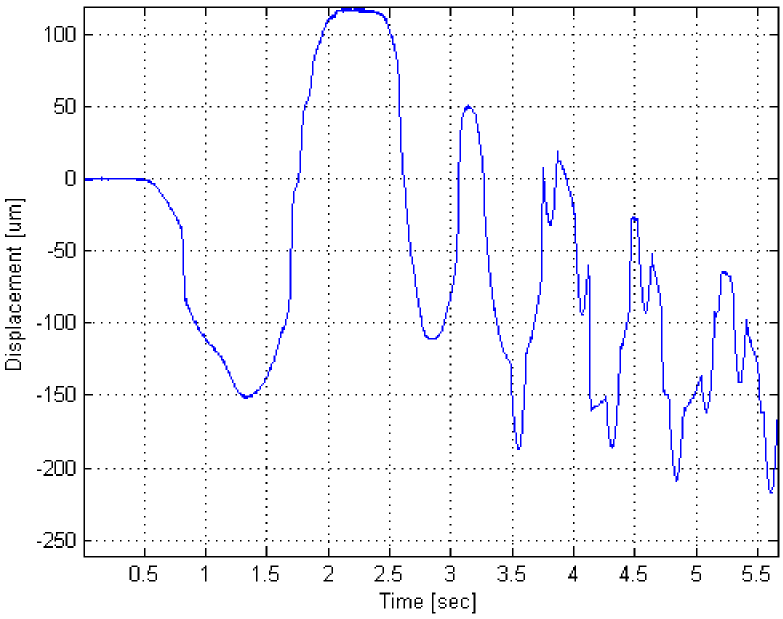

Figure 6.36 Two layer 1 w% agar and 3 w% agar phantom simulation results showing displacement before motion artefact removal. Observed at a depth of about 18.48 mm.

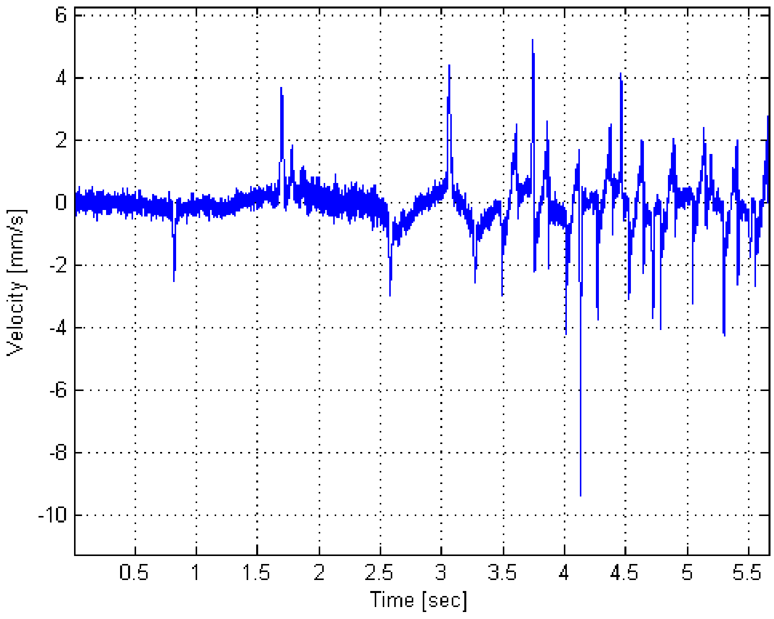

Figure 6.37 Two layer 1 w% agar and 3 w% agar phantom simulation results showing velocity before motion artefact removal. Observed at a depth of about 18.48 mm.

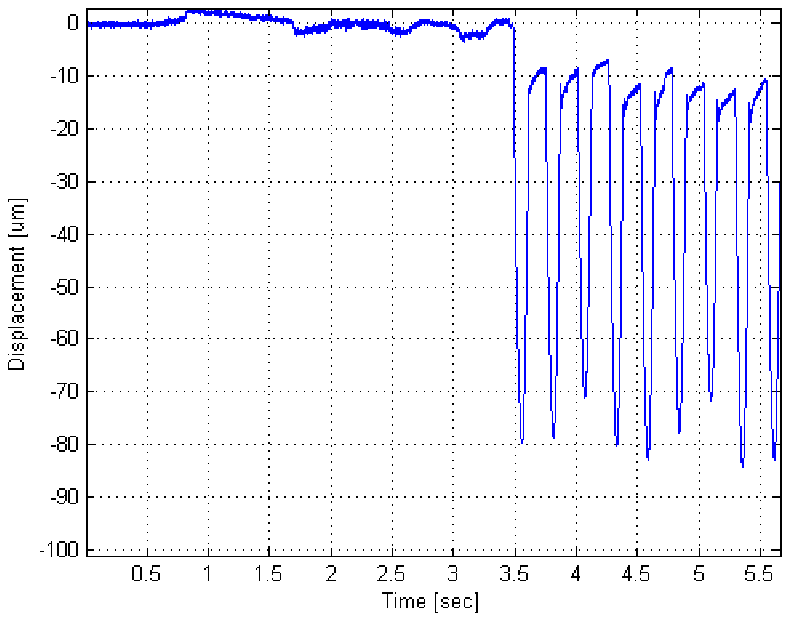

Figure 6.38 Two layer 1 w% agar and 3 w% agar phantom simulation results showing displacement after motion artefact removal. Observed at a depth of about 18.48 mm.

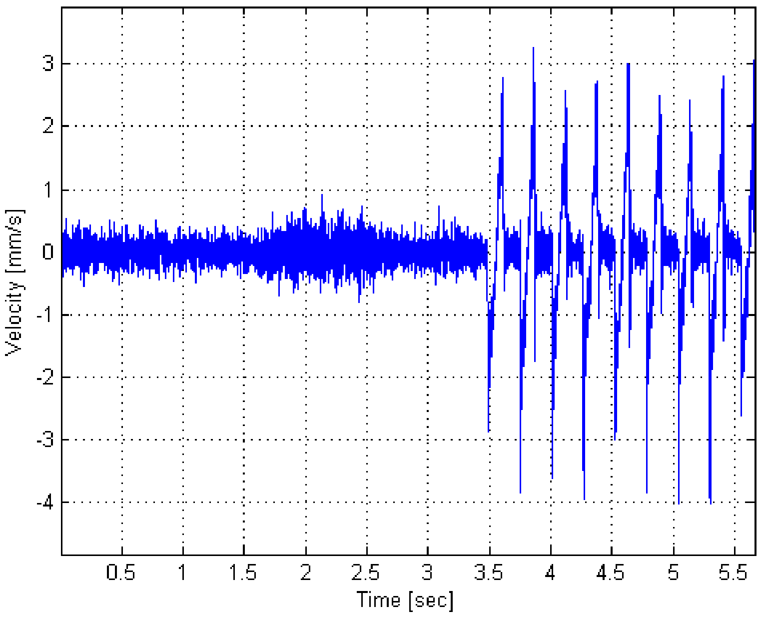

Figure 6.39 Two layer 1 w% agar and 3 w% agar phantom simulation results showing velocity after motion artefact removal. Observed at a depth of about 18.48 mm.

The following results have been provided in order to give a more global picture of the results of the algorithm over all depths within the agar phantoms. In Figure 6.40 and Figure 6.41, showing a displacement profile over all depths, it can be seen how the algorithm correctly removes much of the external motion artefact. Figure 6.42 and Figure 6.43 display velocity profiles before and after motion artefact removal. Although the images are somewhat noisy, the 4 Hz vibration can clearly be seen after the bone boundary algorithm was applied whereas it is difficult to differentiate it from the various other motions that occurred before removing motion artefacts.

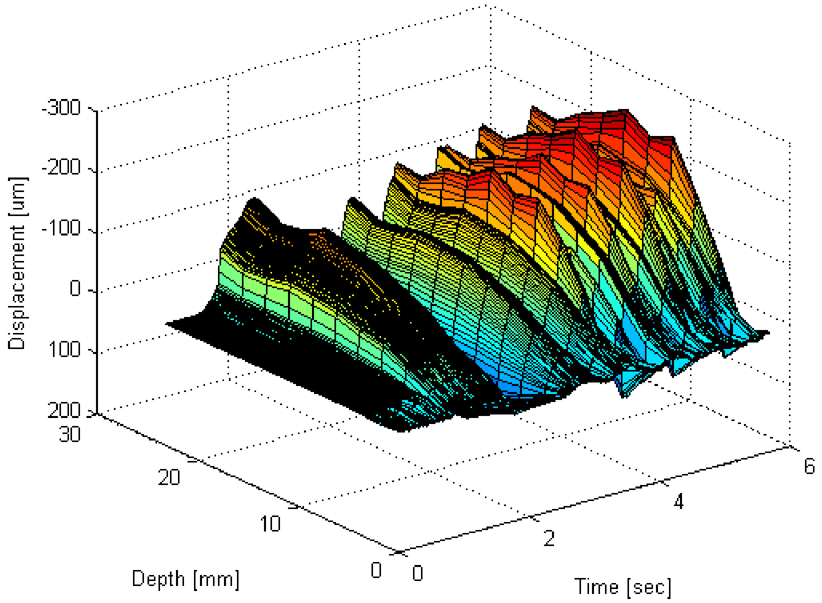

Figure 6.40 Two layer 1 w% agar and 3 w% agar phantom simulation results showing displacement over all depth and time before motion artefact removal.

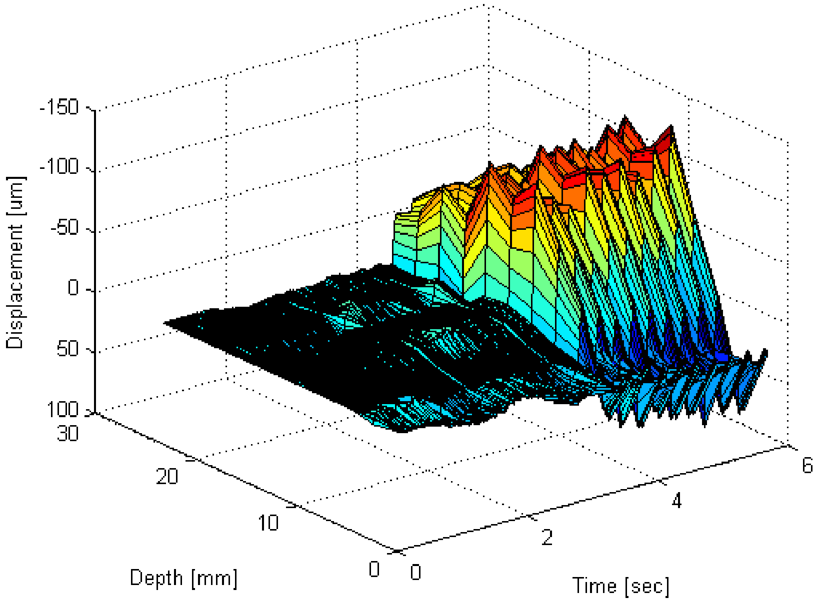

Figure 6.41 Two layer 1 w% agar and 3 w% agar phantom simulation results of displacement over all depth and time after motion artefact removal.

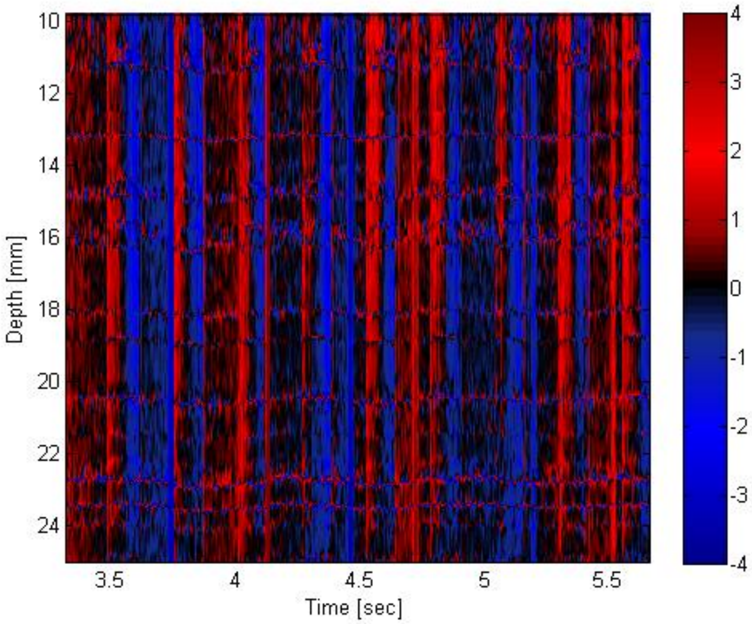

Figure 6.42 Two layer 1 w% agar and 3 w% agar phantom simulation results showing velocity profile image before motion artefact removal. The colour scale represents tissue velocity in mm/s.

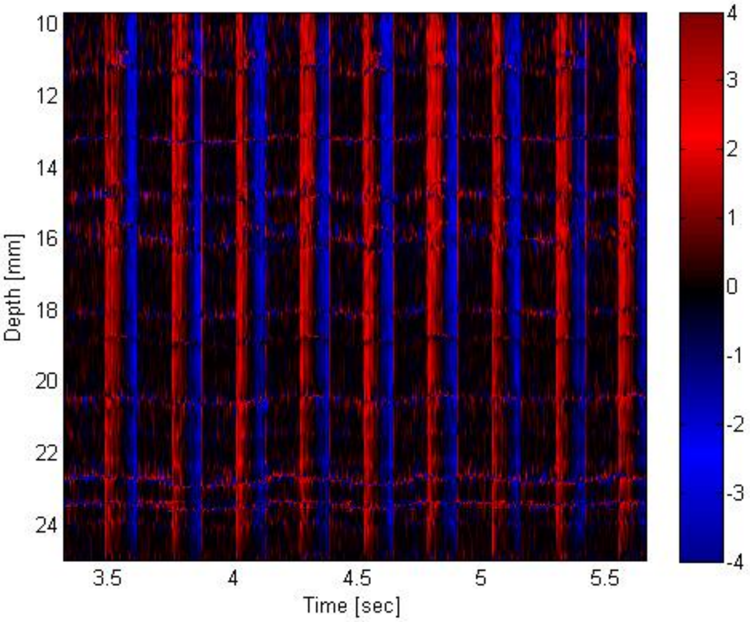

Figure 6.43 Two layer 1 w% agar and 3 w% agar phantom simulation results showing velocity profile image after motion artefact removal. The colour scale represents tissue velocity in mm/s.

The above results show both that the hardware set-up was a good analog to in vivo experimental conditions and that the bone boundary algorithm is a viable solution to removing motion artefacts. The generated 4 Hz mechanical stimulation is similar in both size and shape to what can be expected during in vivo muscle contraction experiments. In addition, it can be seen that the bone boundary algorithm is capable of removing motion artefacts effectively.

The 4 Hz pulse-like motion was clearly recovered in the estimated displacement even with the addition of intentional external motion artefacts. The 4 Hz motion was still visible in the velocity signals after motion artefact removal, but seemed to contain more noise. This noise was most likely due to the method of velocity calculation which was based on taking the derivate of the displacement. It is likely that the noise in the velocity signals had more to do with SNR than the performance of the bone boundary algorithm.

6.4 Accuracy Evaluation

Analyzing simulation and other experimental data can give an idea about the accuracy of the methodology and system used as a whole. Although an exact quantity of error or accuracy cannot be provided due to measurement restrictions, results can be obtained that represent qualities related to accuracy. The following section gives a demonstration of the effectiveness of the bone boundary referencing method for motion artefact removal. In addition, by using the lens echo experiments described in Chapter 3 a relationship demonstrating system measurement error is presented.

6.4.1 Motion Artefact Removal Accuracy

In order to analyze the accuracy of the bone boundary algorithm for removing motion artefacts, strain experimental data was used. This data was used because it is known that all displacement observed in these experiments was due to external probe motion. Therefore, all displacement should be removed as artefact motion. The bone boundary algorithm was applied to strain data taken from a single layer 3 w% agar phantom having a thickness of about 20 mm. The results displayed below show displacement as measured before and after motion artefact removal.

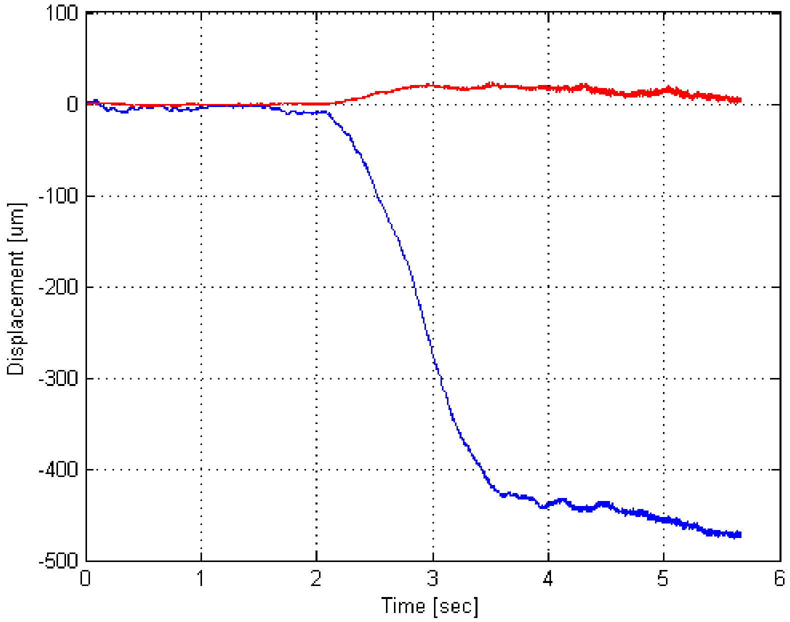

Figure 6.44 Single layer 3 w% agar phantom simulation results showing displacement before (blue) and after (red) motion artefact removal. Observed at a depth of about 11.6 mm.

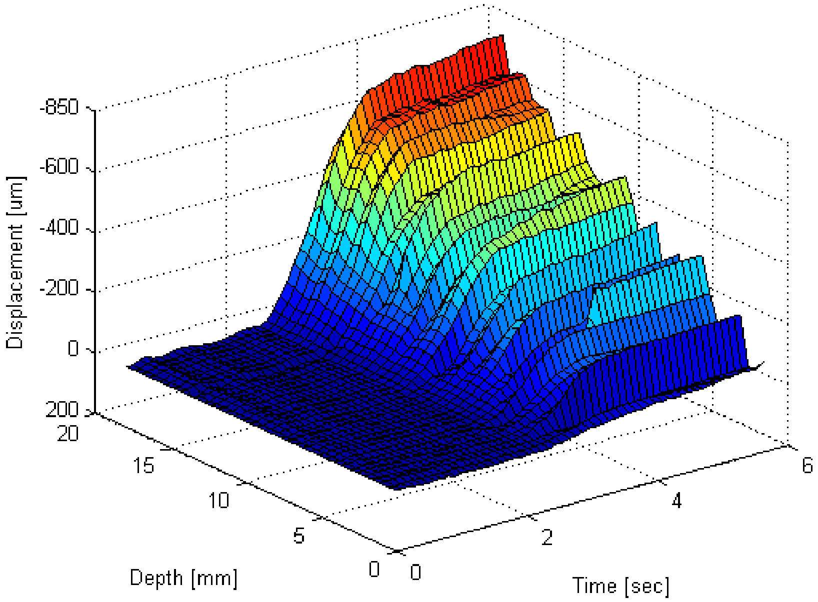

Figure 6.45 Single layer 3 w% agar phantom simulation results showing displacement before motion artefact removal. Observed over all depth and time.

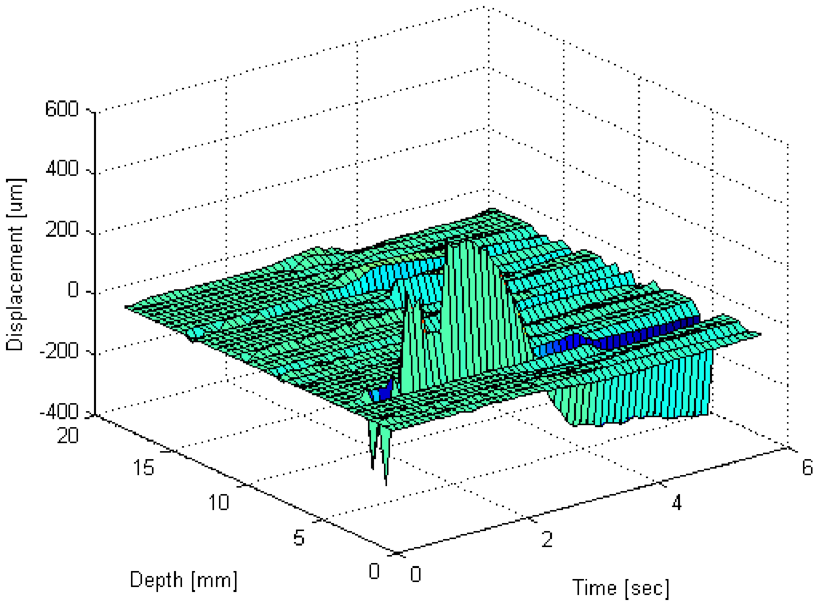

Figure 6.46 Single layer 3 w% agar phantom simulation results showing displacement after motion artefact removal. Observed over all depth and time.

It can be seen from the figures above that the bone boundary algorithm greatly reduces the effect of probe motion. It is known that no motion occurred during approximately the first two seconds of the data. Therefore, this section of the data can be used as a reference value of the signal. The error in this section is due to SNR and hardware measurement constraints and should be unrelated to probe motion. By comparing this reference area to the data after motion had been removed, the bone boundary method in phantom experiments was estimated to be accurate to within about 2 µm.

This value demonstrates that the error present after applying the bone boundary algorithm is likely due more to factors other than the method itself, such as phase jumping. This can be experimentally verified by analysis of Figure 6.45 and Figure 6.46. In Figure 6.45 we can see the displacement before motion artefact removal has occurred. Upon close analysis, it can be seen that the large, fairly obvious errors in Figure 6.46 (after motion artefact removal) are also present in Figure 6.45 (before motion artefact removal). This would suggest that rather than being introduced by the motion artefact removal algorithm, this error is from some other source such as measurement error or phase jumping.

6.4.2 System Measurement Accuracy

In order to estimate system accuracy, data from the lens echo experiments were analyzed. This was done due to the assumption that the echo inside the acoustic lens was stable without a specimen attached. This is a useful property because when dealing with in vivo or phantom measurements there are many variables that effect accuracy which will not be present within the lens. The following simulation both evaluates accuracy, and the effect of temporal averaging. The envelope of the baseband signal was obtained and averaged over all scan lines and can be seen in Figure 6.47 below. This average RF amplitude signal was then compared to the standard deviation of the displacement difference between consecutive frames. The phase difference standard deviation can be seen in Figure 6.48 below. Due to the nature of the experiment, no displacement occurred and therefore this phase difference standard deviation represents phase measurement error.

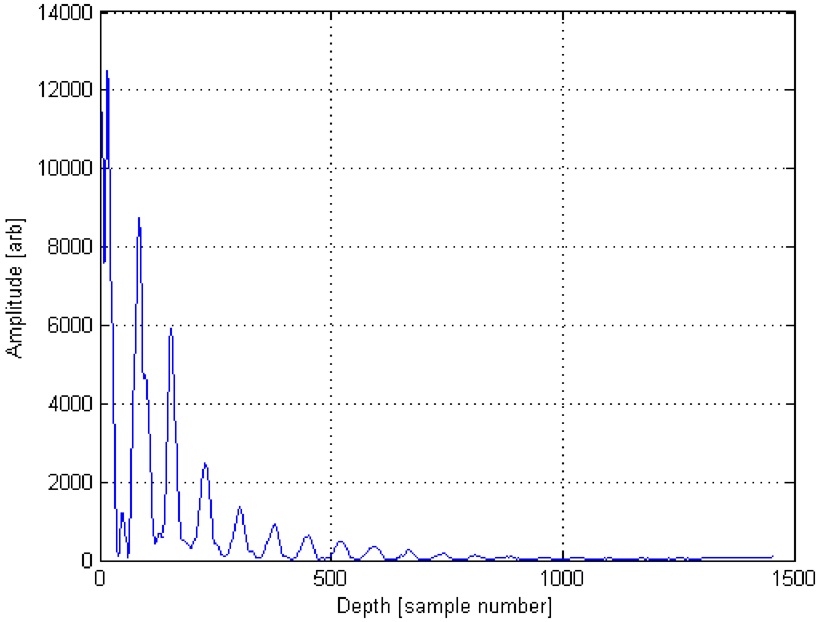

Figure 6.47 Average RF envelope signal during lens echo experiment.

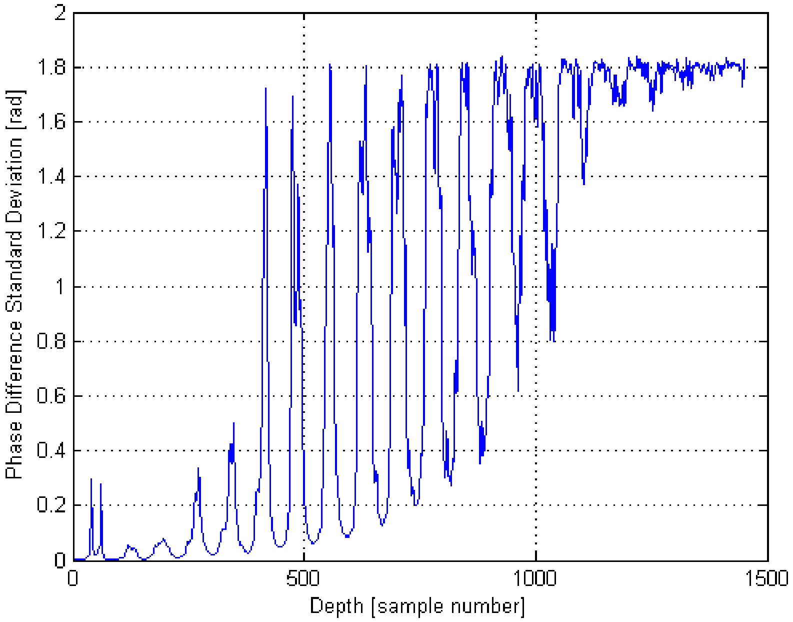

Figure 6.48 Standard deviation of phase difference between consecutive frames for all depth during lens echo experiment.

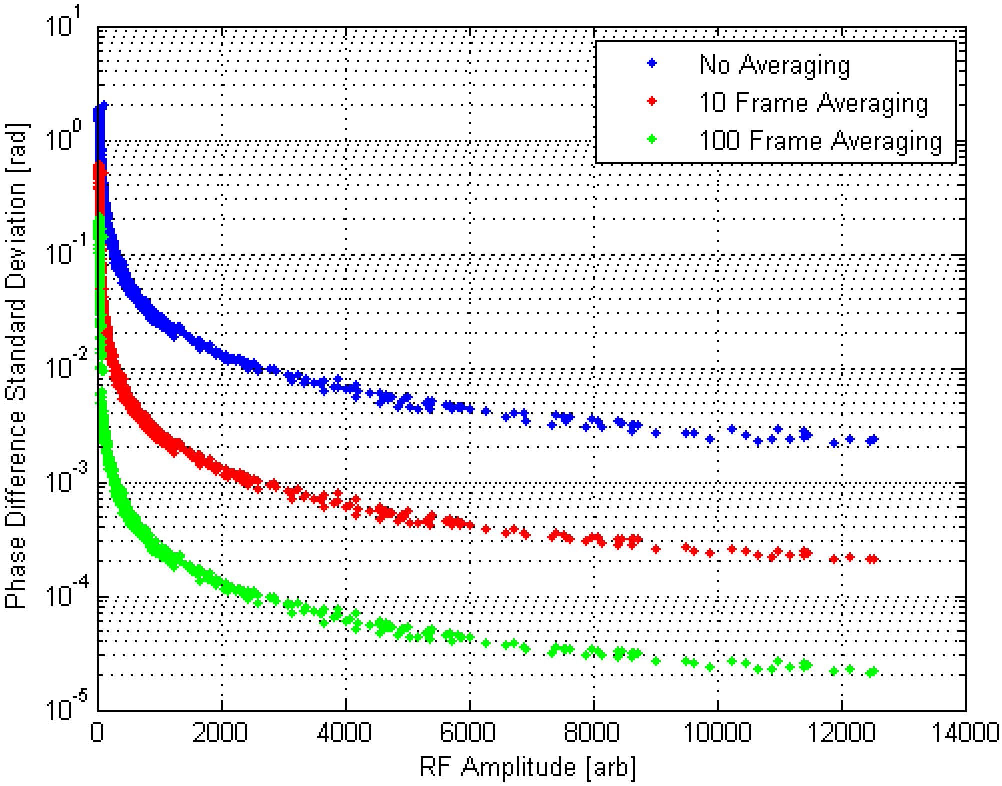

Figure 6.49 Phase difference standard deviation vs. received RF amplitude during lens echo experiment. The averaging was done in the temporal direction.

Figure 6.49 above demonstrates two qualities of measurement accuracy. Firstly, it shows that the phase measurement accuracy increases as the received RF amplitude increases. Secondly, the figure shows that increasing the size of the temporal averaging window decreases the phase measurement error. However, this apparent increased phase measurement accuracy comes at the cost of a loss in temporal resolution. If too large a window is used to average the signal, the temporal resolution will decrease which will in turn decrease the effectiveness of the measurement system.

Chapter 7:

In Vivo Experiments

The eventual goal of our research involves application in human skeletal muscle. Although the majority of work was done in simulation environments to develop and verify algorithms and methodologies, some preliminary work was done on in vivo experiments. These experiments demonstrate the effectiveness of the methods used throughout this research during actual human skeletal muscle trials. The following chapter provides an outline of some experiments done as well as some experimental results. These results both show the usefulness of the methodology developed in this thesis and provide some insight into the internal motion of certain human skeletal muscles.

7.1 Experimental Design

The purpose of the in vivo experiments was to analyze the motion of skeletal muscles under controlled conditions. Firstly, the specific muscle group to be analyzed had to be chosen. In order to use the bone boundary referencing method it was necessary that a signal from the boundary of the bone was obtained. Due to this fact and hardware constraints, a muscle group with a relatively shallow bone location would be ideal for our experiments. For this reason, the muscle group comprised of the Extensor carpi ulnaris, Extensor digitorum, Extensor brevis and Extensor digiti minimi located on the top of the forearm (when the palm is facing down) above the Radius and Ulnar bones were targeted and can be seen in Figure 7.1 and Figure 7.2 below.

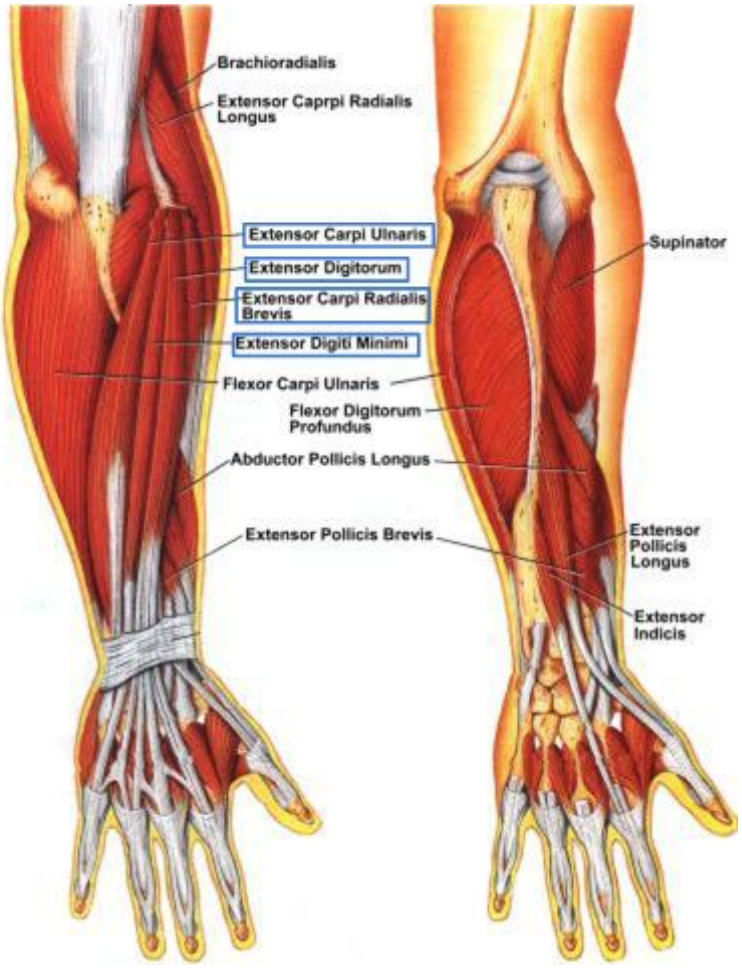

Figure 7.1 Forearm muscle physiology. Reproduced from [97].

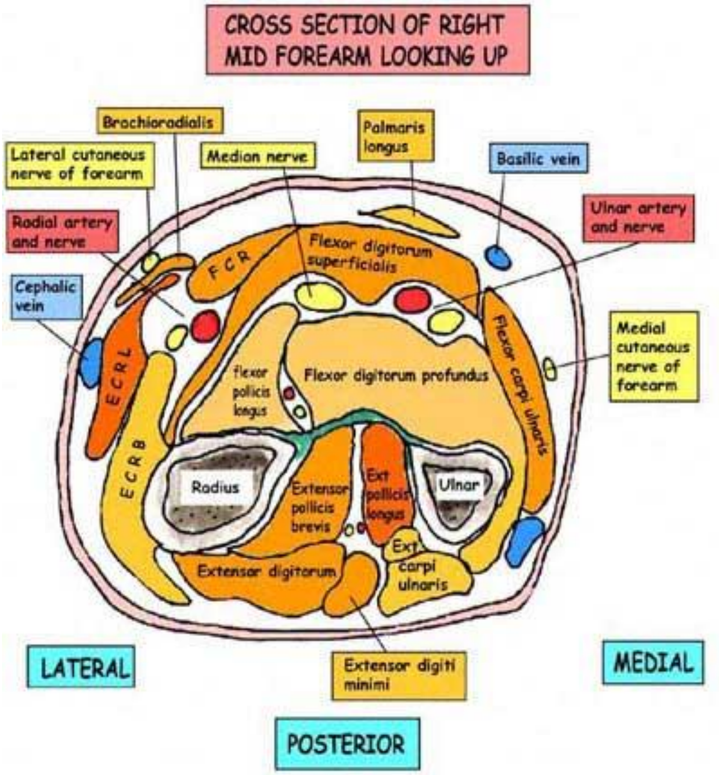

Figure 7.2 Cross section of forearm muscle physiology. Reproduced from [99].

An electrical muscle stimulator (EMS) was used to stimulate these muscles in a repeatable way. The specific stimulator used was the EMS 7500 and can be seen in Figure 7.3(a) below. The probe allowed for an electric pulse with variable voltage, duration and repetition rate to be applied to a subject. A sample of a pulse captured from the EMS electrode leads with an oscilloscope can be seen below in Figure 7.3 (b).

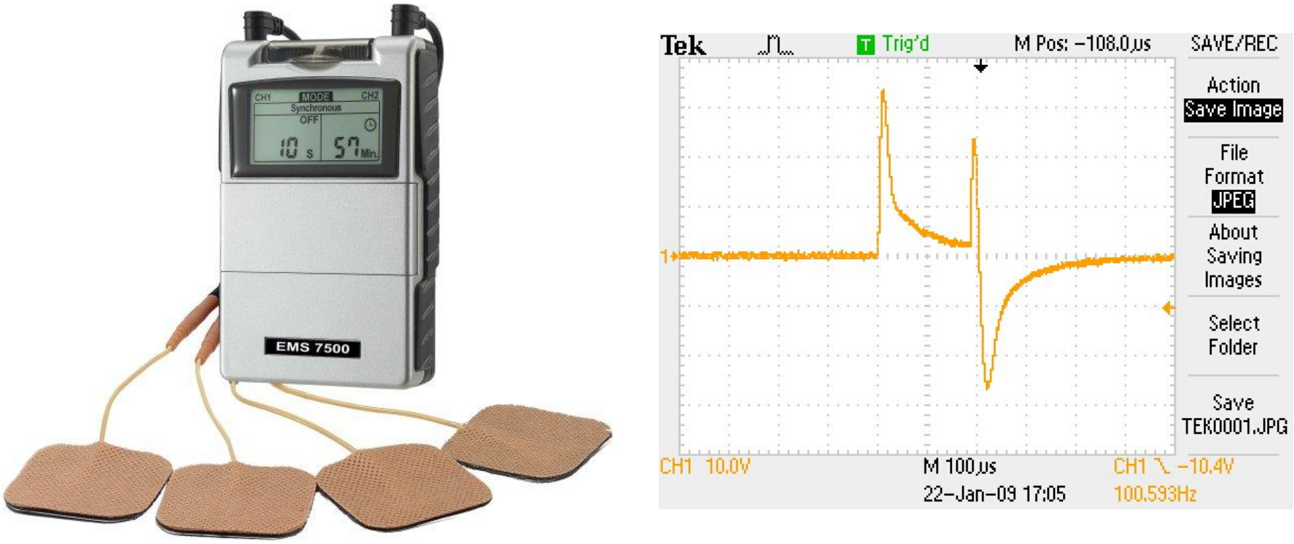

(a) **(b)**

Figure 7.3 Electrical muscle stimulator (a) and stimulation pulse (b). The EMS was set to a pulse width of 200 µs during measurement by an oscilloscope. Figure (a) reproduced from [98].

During experimental procedure, a subject would place their arm palm down onto a table. Two EMS electrodes would be applied to their upper and lower forearm and the probe would be fixed in the middle. The probe was fixed in place using aluminum bars that fastened into the table and nickel plated, rubber tipped clamps. In addition, ultrasonic couplant gel was placed between the probe and the subject’s arm. A photograph of the experimental set up as can be seen in Figure 7.4 and schematic diagrams can be seen in Figure 7.5(a) and Figure 7.6 (a).

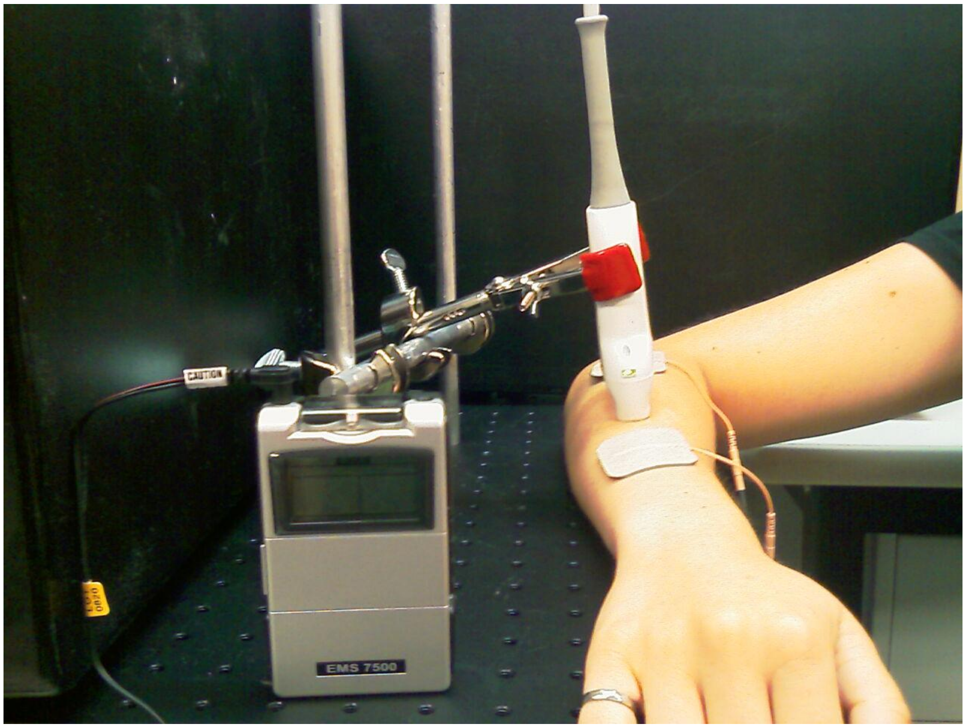

Figure 7.4 In vivo experimental set up.

7.2 Experimental Procedure

The in vivo experimental procedure used was the same as the procedure mentioned in Chapter 6. Specifically, a section of reference data containing only external motion was first recorded. After about two seconds the EMS was switched on and experimental data containing internal tissue and muscle motion was obtained. Due to the nature of the experiments, there was always the possibility of the presence of motion artefacts during data acquisition. However, the reference section of the data could be used by the bone boundary method to remove any motion artefacts that may have occurred. In addition, it was possible to obtain strain images at any point in time assuming that a displacement had occurred.

7.3 Experimental Results

The probe was fixed in place onto the top of a subject's forearm which was itself placed onto a table. The probe was placed both parallel and perpendicular to the muscle fibers of the arm and schematic diagrams with their accompanying obtained B-mode images can be seen below in Figure 7.5 and Figure 7.6. The parallel configuration was primarily used for orientation and B-mode strain images whereas the perpendicular configuration was used mostly to obtain the EMS motion results. A sample of the RF scan line used for the M-mode experiments can be seen Figure 7.6 (c) and is marked with a purple line in the B-mode image of Figure 7.6 (b).

Motion data was obtained during forced muscle contraction by the EMS in the experimental section of the data. In addition, M-mode strain data was obtained during both the reference and experimental sections of the acquired data set and was used to give stiffness information both before and during muscle contraction. The results of various experiments are provided below along with a demonstration of the effectiveness of the bone boundary method for motion artefact removal.

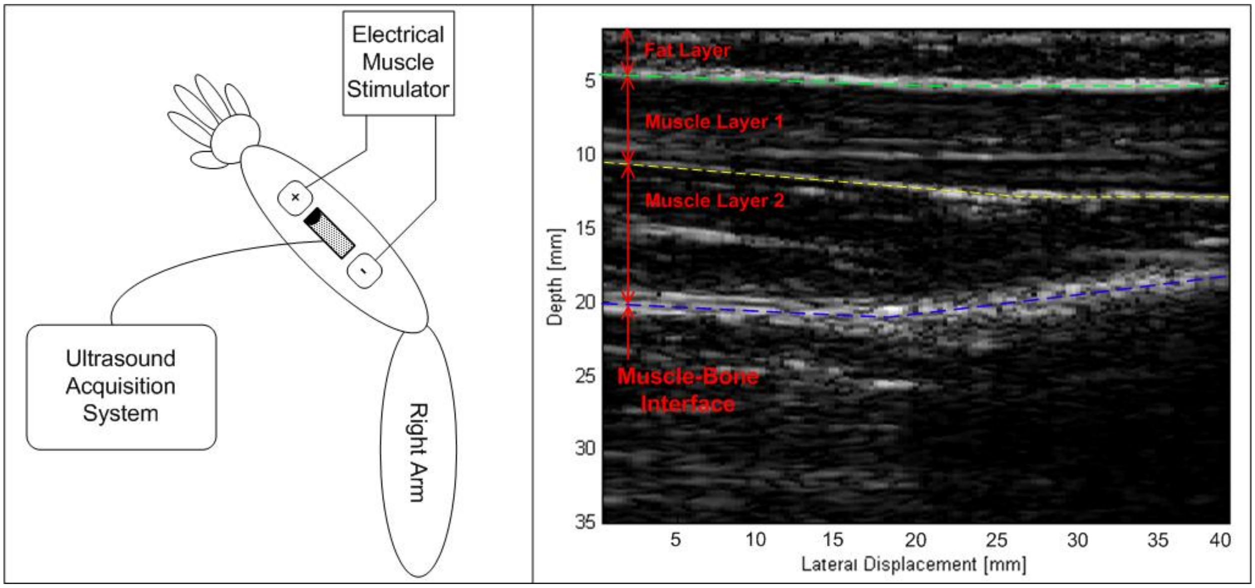

(a) (b)

Figure 7.5 Parallel to muscle experimental design. The set up is shown as a schematic diagram (a) and a corresponding B-mode image (b) demonstrating a configuration with the probe fixed parallel to the muscle fibers.

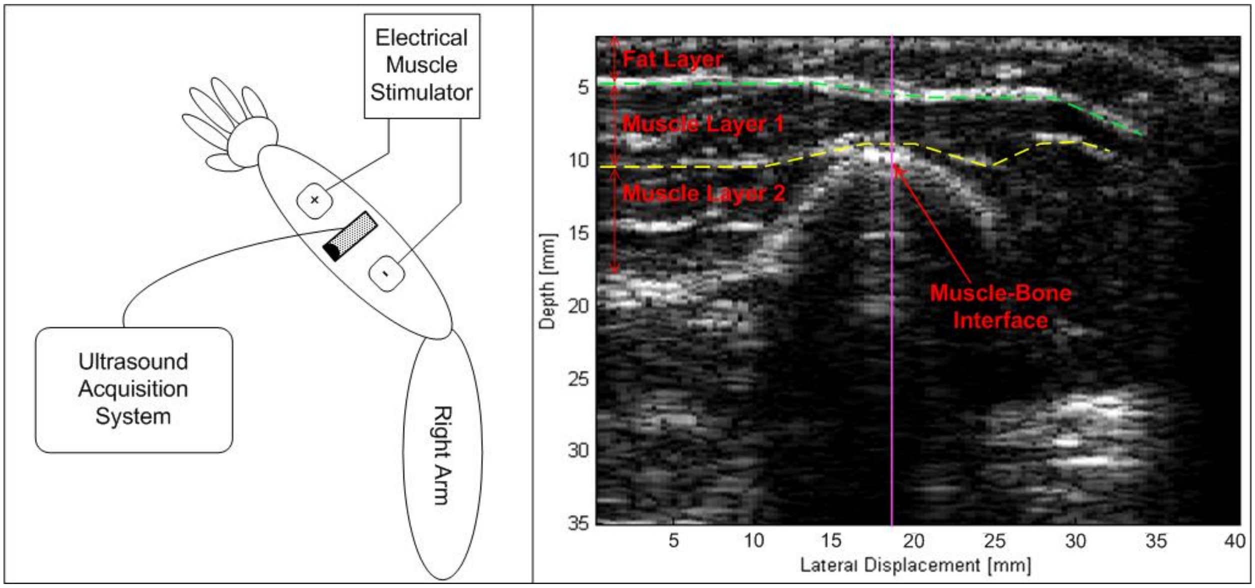

(a) (b)

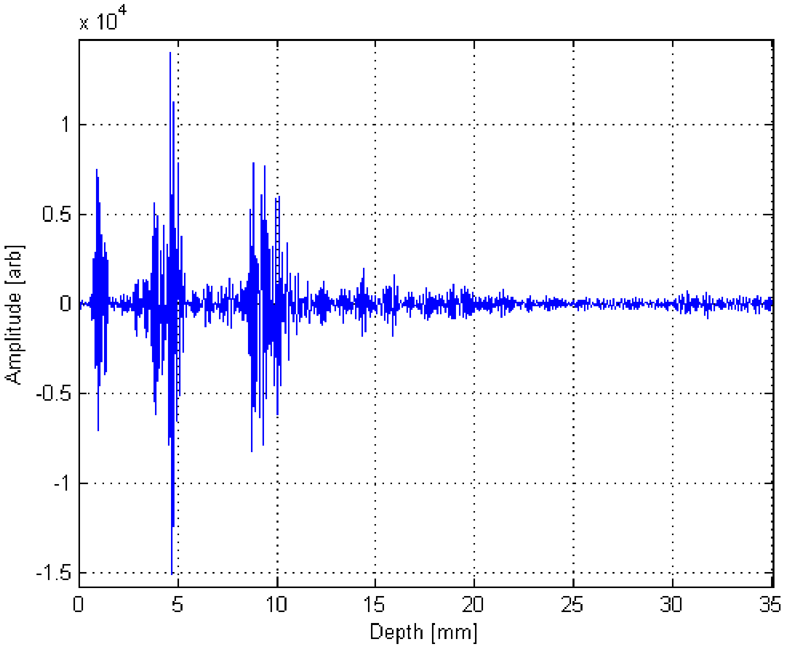

(c)

Figure 7.6 Perpendicular to muscle experimental design. The set up is shown as a schematic diagram (a) and a corresponding B-mode image (b) demonstrating a configuration with the probe fixed perpendicular to the muscle fibers. The RF scan line corresponding to the location marked by the purple line in (b) can be seen in (c).

7.3.1 Muscle Motion

Data was collected during forced muscle contraction by EMS over a range of pulse repetition rates from 2 Hz to 12 Hz with an interval of 1 Hz. The location of the M-mode scan line used can be seen as marked by the purple line in Figure 7.5 (b). Due to the large amount of data acquired during all of these experiments, selected results from the 2 Hz, 4 Hz and 6 Hz experiments are provided to follow. The goal of this research was more to develop a methodology that could be used to analyze muscle characteristics and less to interpret acquired in vivo data. Due to this fact, the following results are provided to demonstrate the viability of the developed method for analyzing in vivo data. However, an interpretation of the data is provided in this section after the results have been provided. The verification of this interpretation is left as future work.

7.3.1.1 Experimental Results from 2 Hz Stimulation

The following results were obtained from an experiment in which the EMS was set to a repetition rate of 2 Hz. The results to follow were obtained from an observation depth of about 7.16 mm which should correspond to a location within a layer of muscle.

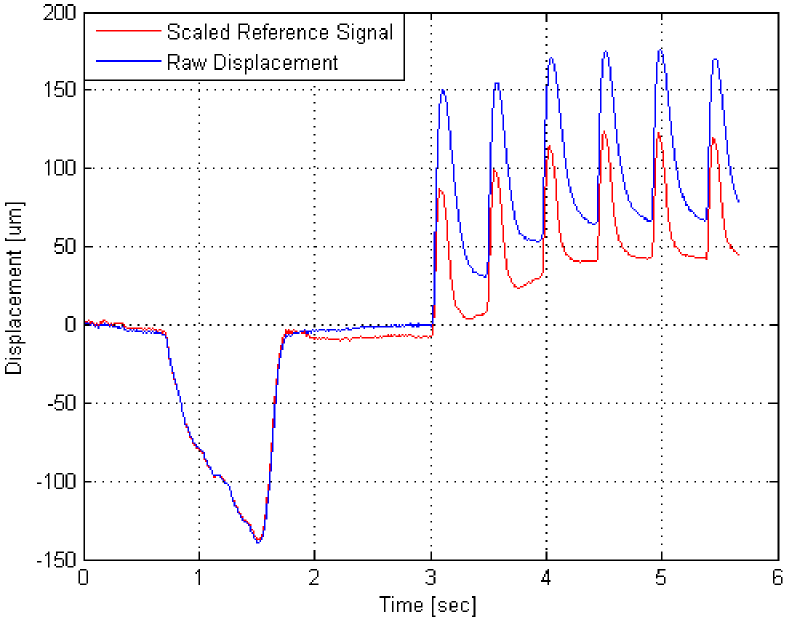

Figure 7.7 In vivo tissue displacement during 2 Hz EMS before motion artefact removal. The scaled bone boundary reference signal (red) was subtracted from the raw measured displacement (blue) in order to obtain the motion corrected signal. Observed at a depth of about 7.16 mm.

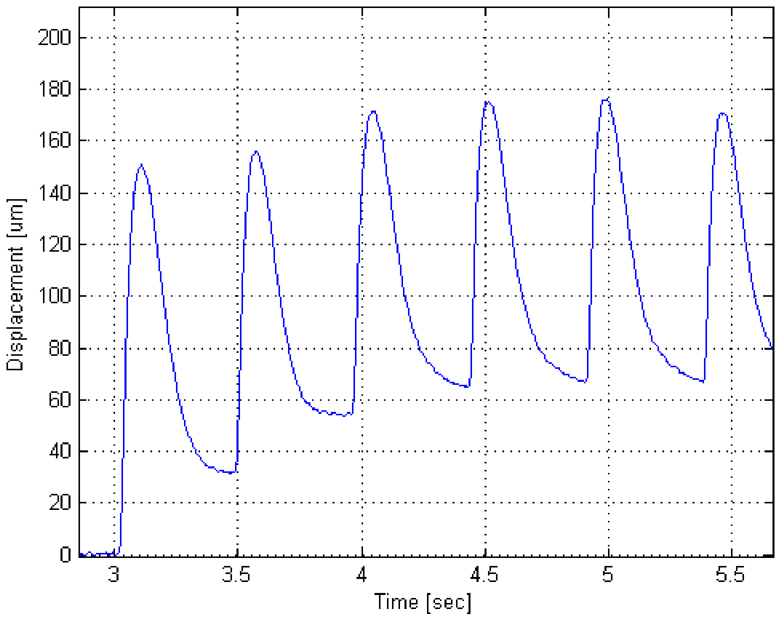

Figure 7.8 In vivo tissue displacement during 2 Hz EMS before motion artefact removal. Observed at a depth of about 7.16 mm.

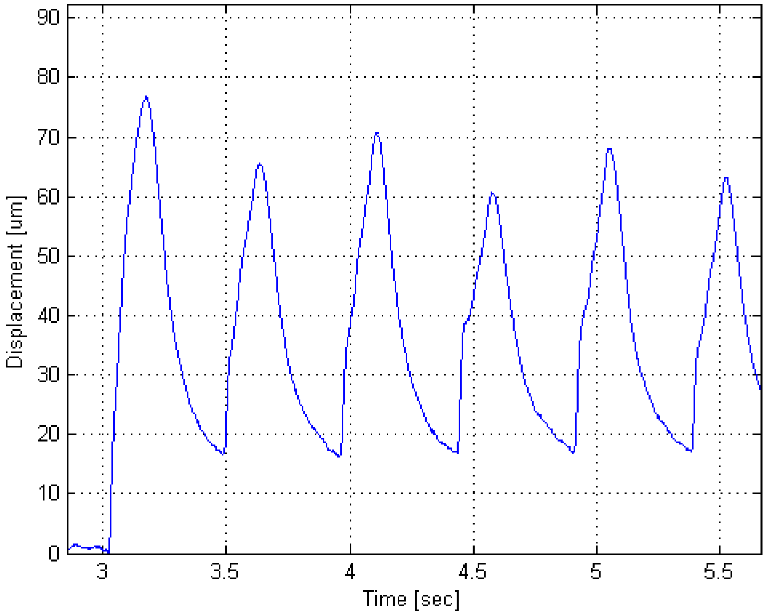

Figure 7.9 In vivo tissue displacement during 2 Hz EMS after motion artefact removal. Observed at a depth of about 7.16 mm.

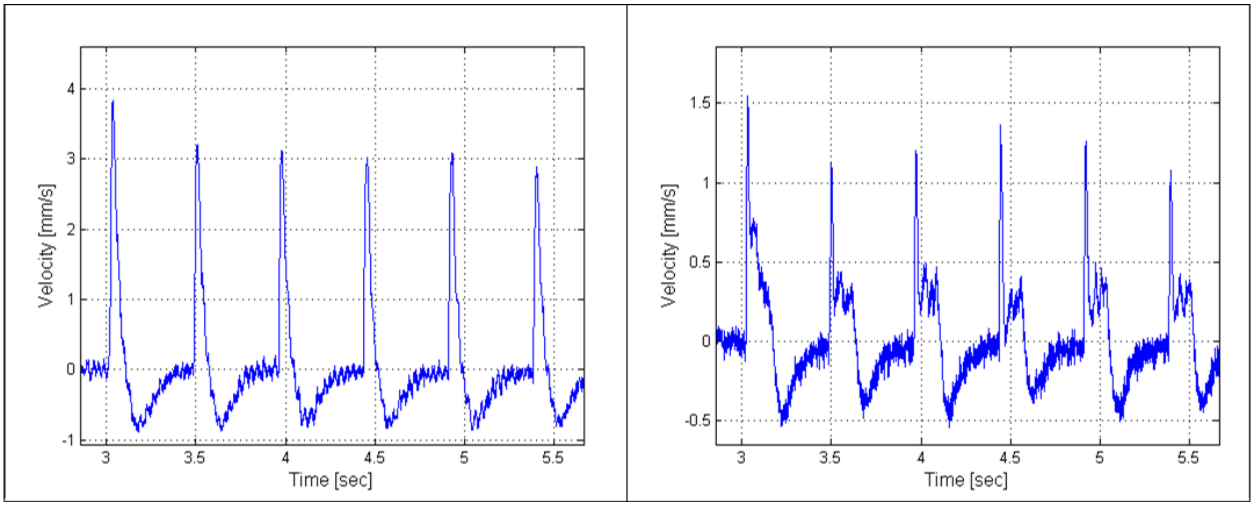

(a) **(b)**

Figure 7.10 In vivo tissue velocity during 2 Hz EMS. The velocity is shown before and after motion artefact removal in (a) and (b) respectively and observed at a depth of about 7.16 mm.

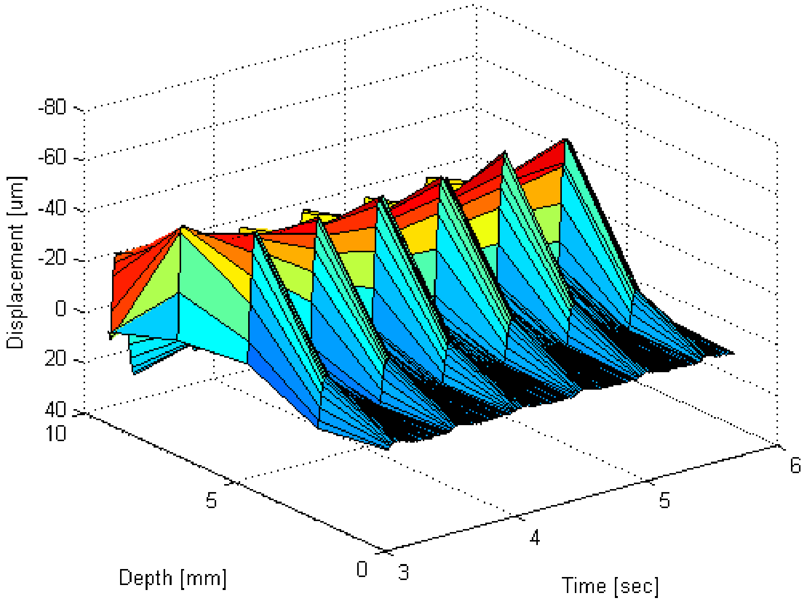

Figure 7.11 In vivo tissue displacement over all depth after motion artefact removal during 2 Hz EMS.

7.3.1.2 Experimental Results from 4 Hz Stimulation

The following results were obtained from an experiment in which the EMS was set to a repetition rate of 4 Hz. The results to follow were obtained from an observation depth of about 6.93 mm and should correspond to a location within a layer of muscle.

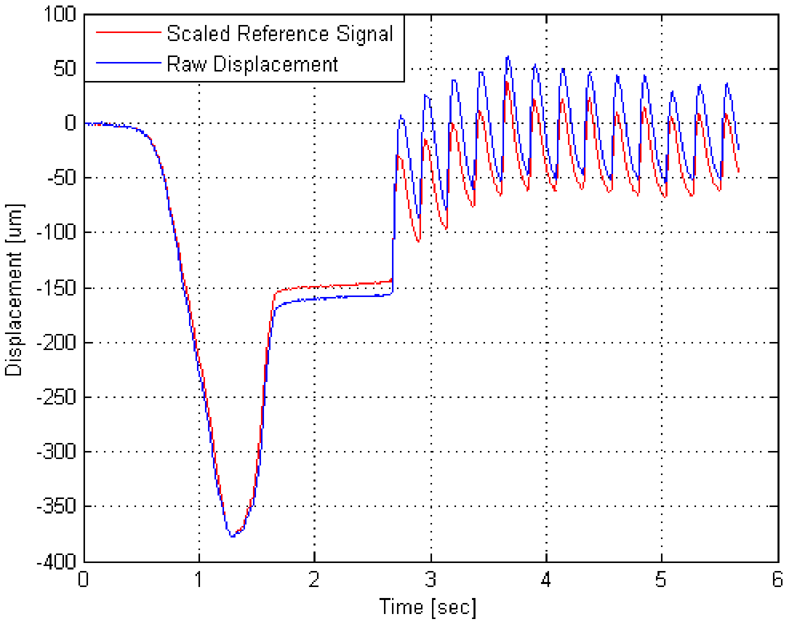

Figure 7.12 In vivo tissue displacement during 4 Hz EMS before motion artefact removal. The scaled bone reference signal (red) was subtracted from the raw measured displacement (blue) in order to obtain the motion corrected signal. Observed at a depth of about 6.93 mm.

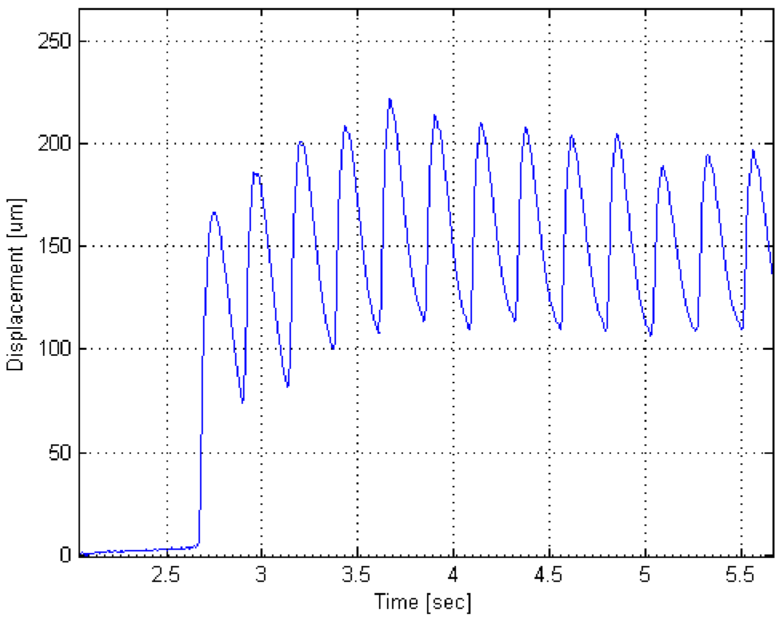

Figure 7.13 In vivo tissue displacement during 4 Hz EMS before motion artefact removal. Observed at a depth of about 6.93 mm.

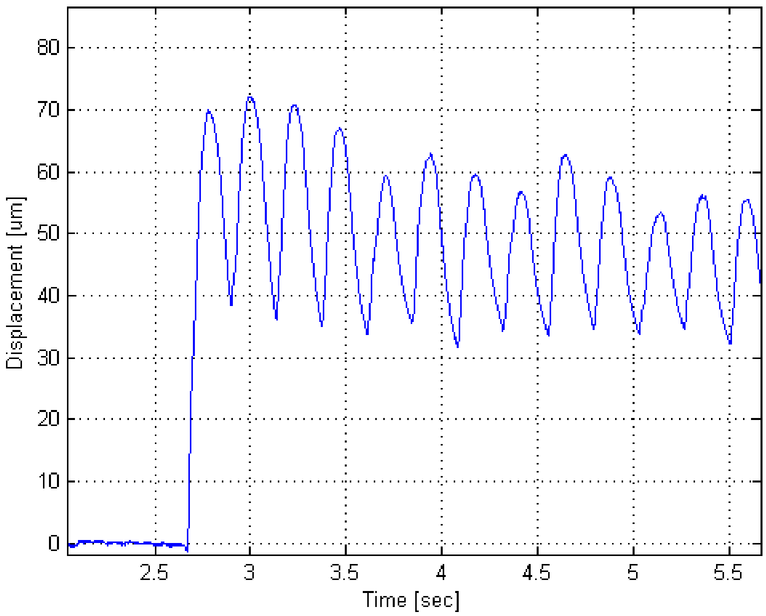

Figure 7.14 In vivo tissue displacement during 4 Hz EMS after motion artefact removal. Observed at a depth of about 6.93 mm.

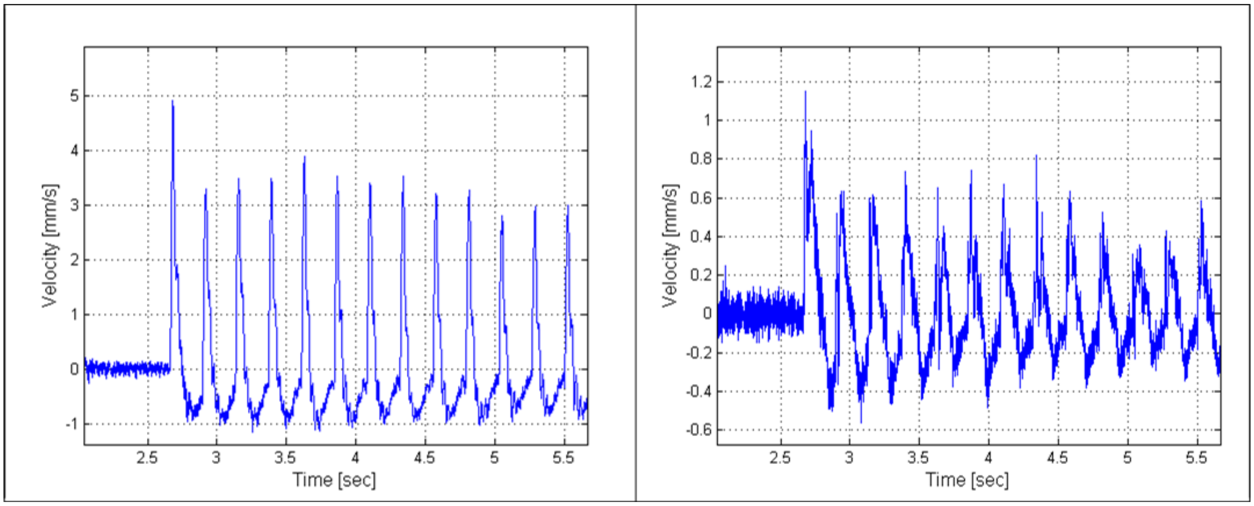

(a) **(b)**

Figure 7.15 In vivo tissue velocity during 4 Hz EMS. The velocity is shown before and after motion artefact removal in (a) and (b) respectively and observed at a depth of about 6.93 mm.

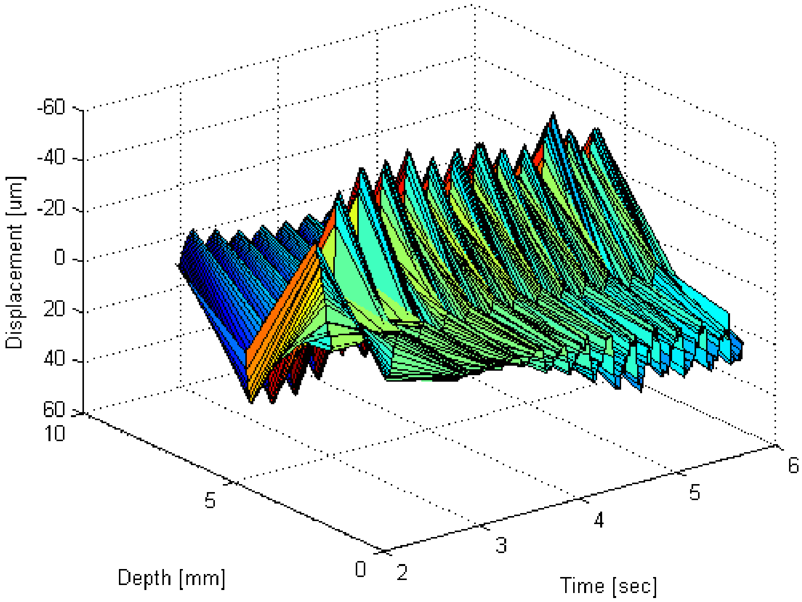

Figure 7.16 In vivo tissue displacement over all depth after motion artefact removal during 4 Hz EMS.

7.3.1.2 Experimental Results from 6 Hz Stimulation

The following results were obtained from an experiment in which the EMS was set to a repetition rate of 6 Hz. The results to follow were obtained from an observation depth of about 6.93 mm and should correspond to a location within a layer of muscle.

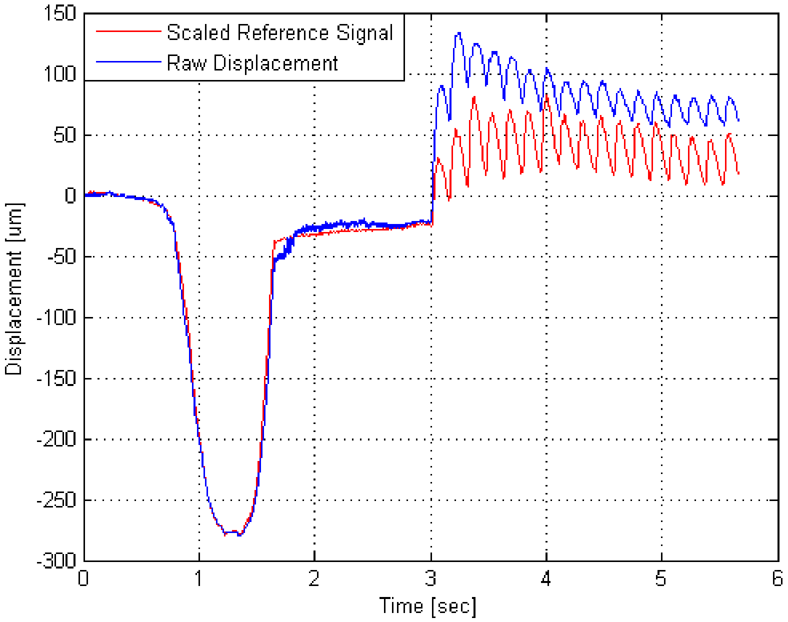

Figure 7.17 In vivo tissue displacement during 6 Hz EMS before motion artefact removal. The scaled bone reference signal (red) was subtracted from the raw measured displacement (blue) in order to obtain the motion corrected signal. Observed at a depth of about 6.93 mm.

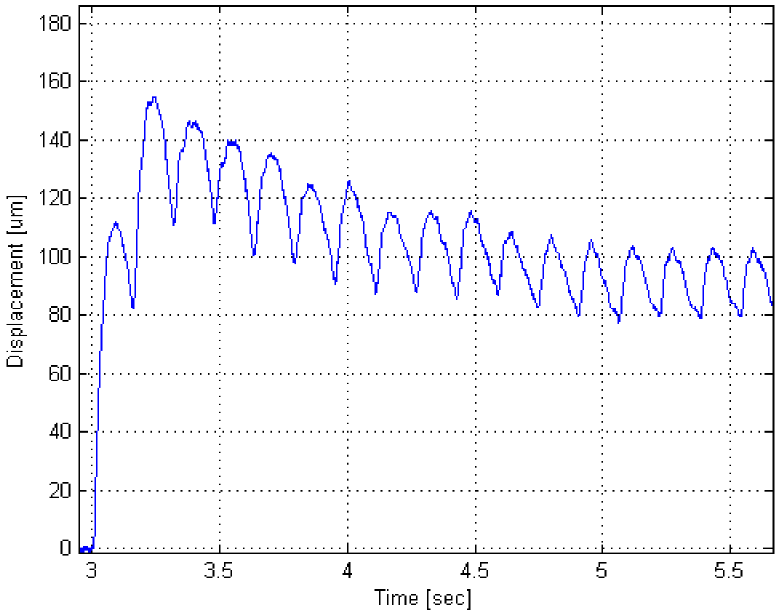

Figure 7.18 In vivo tissue displacement during 6 Hz EMS before motion artefact removal. Observed at a depth of about 6.93 mm.

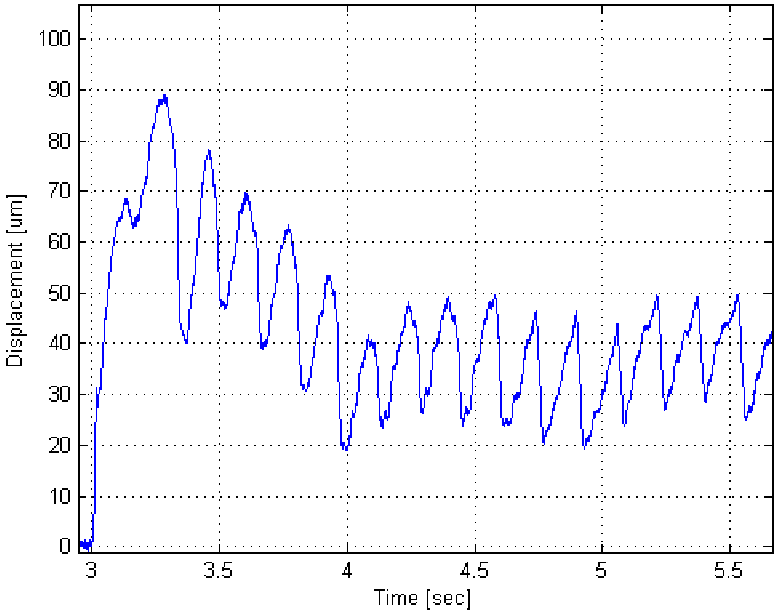

Figure 7.19 In vivo displacement during 6 Hz EMS after motion artefact removal. Observed at a depth of about 6.93 mm.

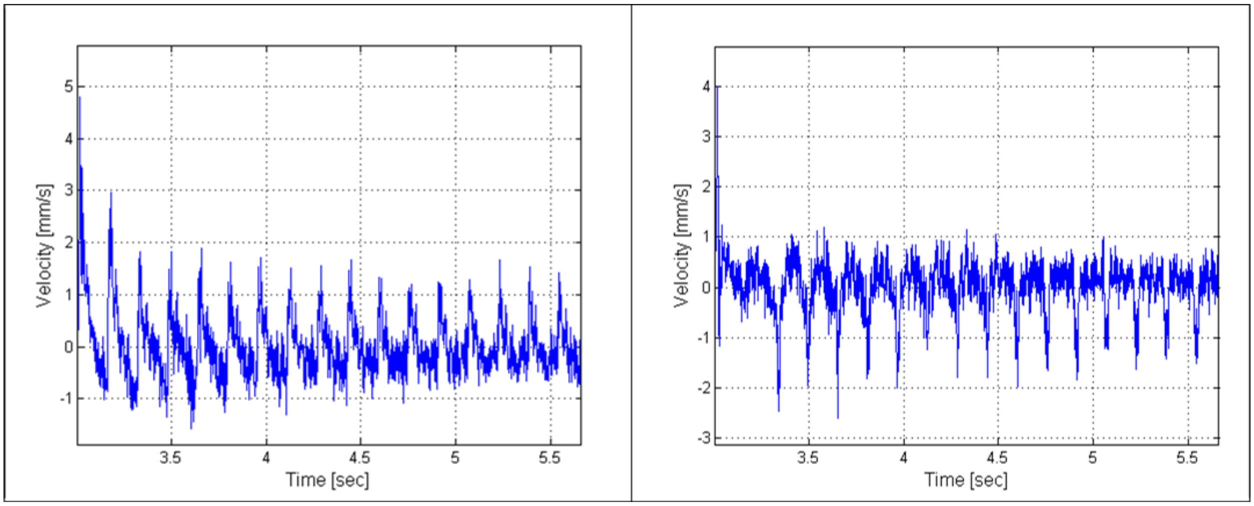

(a) **(b)**

Figure 7.20 In vivo tissue velocity during 6 Hz EMS. The velocity is shown before and after motion artefact removal in (a) and (b) respectively and observed at a depth of about 6.93 mm.

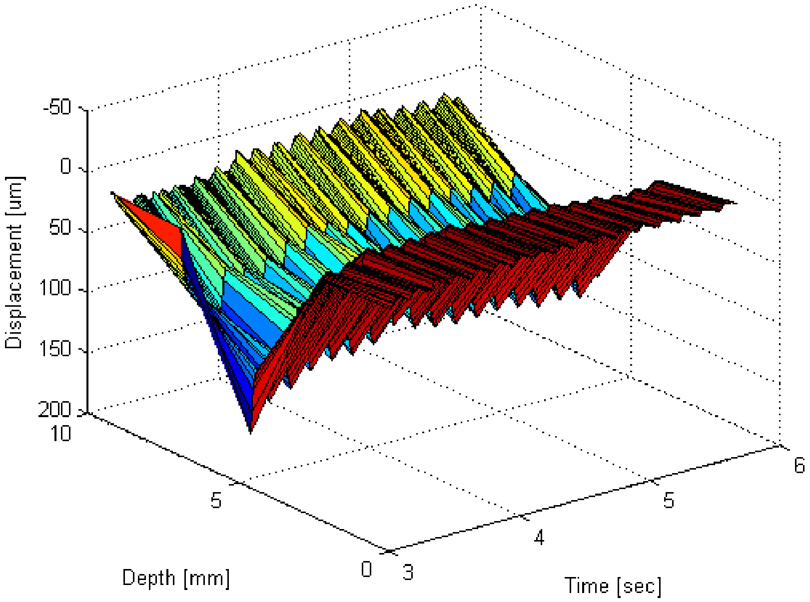

Figure 7.21 In vivo tissue displacement over all depth after motion artefact removal during 6 Hz EMS.

7.3.2 Discussion

The above results show how the designed methodology results in both displacement and velocity estimation of muscle motion. In addition, it can be seen that the motion artefact removal algorithm has been applied in order to give information about the internal motion of the tissue. Although it will be necessary to do much future work analyzing this and other in vivo data, it is possible to provide a brief interpretation of the above data.

It can be seen that displacement is observed in a direction both towards and away from the probe in the three dimensional surface plots of Figure 7.11, Figure 7.16 and Figure 7.21. It is possible that this phenomenon is simply caused by noise or error. However, upon analyzing the results carefully, it was seen that similar areas in all experimental data collected displayed similar displacements in terms of direction at similar depths. This would suggest that a physical property of the tissue is being observed, rather than the effect of noise or error.

All of the above results obtained with different stimulation pulse repetition rates indicate positive displacement due to muscle stimulation as they were all gathered from a similar depth location. It will be seen in Figure 7.22 to follow that at a shallower region the displacement is all in a direction towards the transducer. Aside from direction, it can be seen that there is a peak in the displacement magnitude located both in the presumed muscle area and the fat area. This observation is similar to results seen during multi-layer phantom studies. This similarity to phantom studies along with known muscle physiology could suggest that the peak displacement magnitude found in the muscle layer could correspond to the location of the muscle contraction origin. Again, as in phantom studies, the peak displacement magnitude in the fat area could suggest some property due to the relative stiffness differences between the muscle and fat layers. Although these observations cannot be entirely verified, they do demonstrate the usefulness of the designed muscle measurement system and identify a need for future in vivo work.

Finally, the results from a number of experiments have been combined together and are shown in Figure 7.22. This figure shows displacement waveforms during EMS for a range of stimulation repetition rates from 2 Hz to 12 Hz. The displacements shown correspond to an observation depth of 6.47 mm. It can be seen that the displacements resulting from muscle contraction are all in a direction towards the probe. These displacements are in the opposite direction from the results observed at a deeper location in the muscle as shown above. In addition, this figure demonstrates how the muscle reacts to an increase in stimulation pulse repetition rate and the concept of tetanus as described in Chapter 2. It can be seen that as the stimulation rate increases, the muscle is unable to fully relax and a state of forced constant contraction is observed.

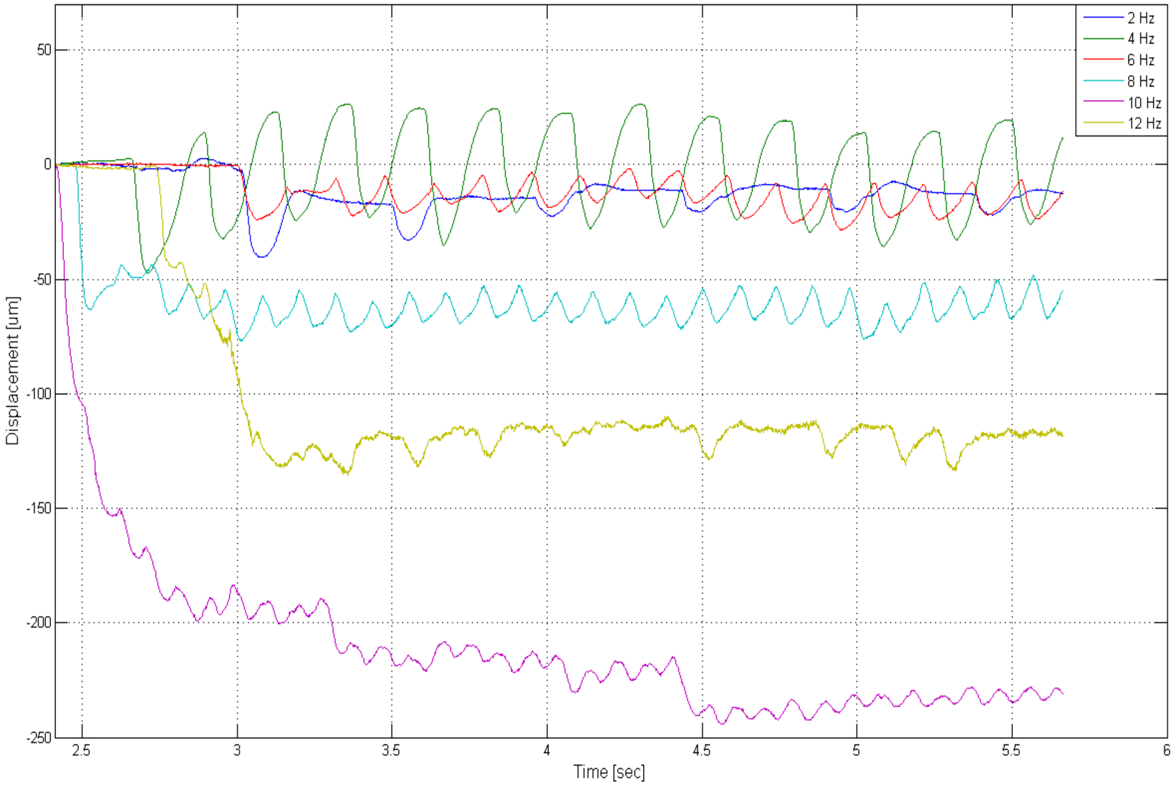

Figure 7.22 In vivo tissue displacement during 2 Hz to 12 Hz EMS. The depth of observation is about 6.47 mm.

It can be seen from the above figure that the magnitude of the displacement during 12 Hz stimulation is less than that from 10 Hz stimulation. This could possibly be due to muscle fatigue experienced during other tests done before the 12 Hz experiment. In addition, the 12 Hz stimulation signal seems to contain a pulse signal on the order of 3 Hz. It is a curious phenomenon that could either be caused by some form of measurement error, or an actual physiological effect. These observations again demonstrate a need for future in vivo studies to be conducted.

7.3.3 Strain Images

In order to demonstrate strain imaging, two different types of experiments were done. The first were those of the above section in which muscle stimulation was recorded using M-mode. However, instead of only analyzing displacement and velocity measurements, the results obtained were also used to estimate strain information. In this way, a time varying strain image could be created from the same data that was used to measure muscle motion.

In addition to making strain estimations during EMS contraction, specific strain experiments were also done using B-mode imaging and the experimental procedure from Section 6.2.1. From these results, a cross sectional image representing strain was obtained. In the case of in vivo measurements, specific boundaries were difficult to track due to the complexity of the received signals. For this reason, results provided in the following section are estimations of instantaneous strain rather than the average strain in a region as was often estimated in Chapter 6.

7.3.2.1 M-Mode Strain Imaging During Muscle Motion Experiments

The following results were obtained during an experiment in which a 3 Hz electrical stimulation was applied to the right forearm. The strain measurement data in this section were obtained with the same experimental procedure used in Section 7.3.1 to analyze muscle motion. Figure 7.23 below shows the strain over all time and from a depth at the surface of the probe to the approximate location of the bone.

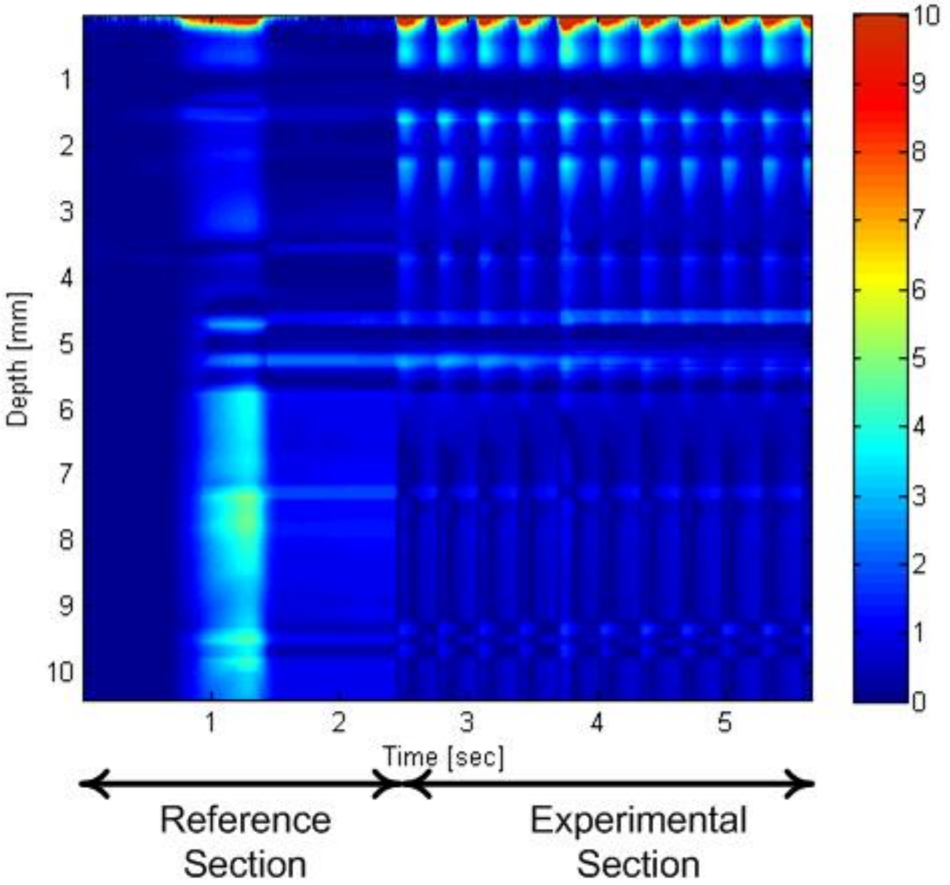

Figure 7.23 In vivo M-mode strain image. The colour scale represents percentage of strain.

This figure demonstrates the relative strain differences between the muscle and fat layers during external compression and internal muscle contraction. Recall that during muscle motion experiments a reference section of data was first acquired containing displacement due only to external compression and was followed by an experimental section containing motion due to internal muscle contraction. These two sections can be seen from 0 to about 2.5 seconds and from about 2.5 seconds to about 5.7 seconds in Figure 7.23, respectively. It is known from Figure 7.6 that there is an interface between fat and muscle at an approximate depth of 5 mm which can also be observed in the strain image above.

A clear difference in strain can be seen between the region of the forearm before and after the approximately 5 mm boundary. It can be seen that in the reference section of the data, due to external compression of the tissue with the probe, the muscle layer appears to experience a strain of about 4% whereas the fat layer experiences only about 2% strain. This suggests that the relaxed muscle layer is less stiff than the fat layer. This is contrary to the expectation that muscle is stiffer than fat. One possible explanation for this could be that during imaging, the probe was pressed down into the tissue such that the fat layer was entirely compressed at the beginning of data acquisition. This pre-compression of the fat layer could explain why the muscle appears to be less stiff than the fat layer.

In the experimental data section of Figure 7.23 it can be seen that deeper than 5 mm, in the muscle layer, less than 1% strain is experienced whereas about 4% strain is experienced in the fat layer. This suggests that during this time period the muscle layer is stiffer than the fat layer. This coincides with expectation as during this section of the data the muscle was being stimulated with the EMS. This observation logically suggests that muscle during contraction is even stiffer than compressed fat. The above M-mode strain image demonstrates how strain information can be obtained from the same experiments used to estimate muscle motion and can give information about tissue stiffness over time.

7.3.2.2 B-Mode Strain Imaging Experimental Results

In order to obtain B-mode strain imaging results, the strain estimation experimental procedure of Section 6.2.1 was used. The probe was oriented parallel to the muscle fibers as described in Figure 7.5 above. In order to lessen the effects of noise, an averaging window of about 0.1617 mm axially and 3.4646 mm laterally was applied to the displacement estimations before estimating strain. The standard B-mode image along with the corresponding strain image after compression can be seen in Figure 7.24 below. The B-mode strain image differs from the M-mode strain image seen above in that the B-mode strain image provides both axial and lateral information.

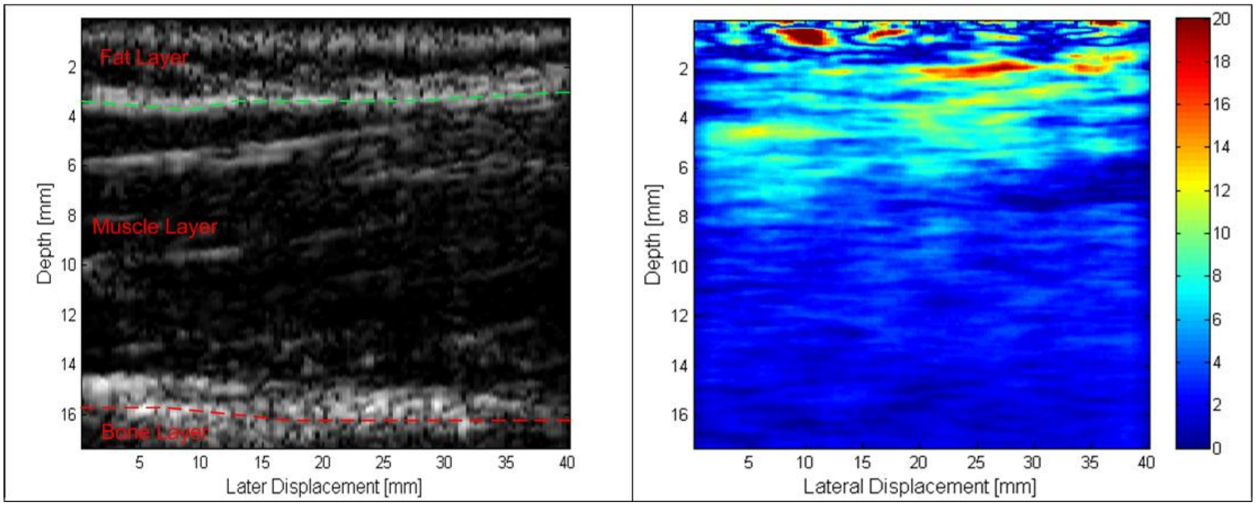

(a) **(b)**

Figure 7.24 In vivo B-mode and strain images. A standard B-mode image after compression is seen in (a) with its corresponding strain image shown in (b).

The above figure demonstrates how the fat layer experiences a greater strain and is therefore softer than the muscle layer. It can be seen from the B-mode image in Figure 7.24 (a) that the boundary between the fat and muscle layer is located at a depth of about

4 mm. The strain image shows a change in stiffness at approximately the same location indicating the fat-muscle interface. It also appears that the fat layer is not entirely uniform as the strain differs throughout this region. In contrast, however, the muscle layer seems to have a much more uniform strain distribution. For this experiment, it was ensured that the fat layer was not compressed before data acquisition. This fact could explain why the B-mode strain image demonstrates the more intuitive result that during external compression the relaxed muscle layer appears to be stiffer than fat.

7.4 Accuracy Evaluation

Experiments done on actual human subjects are inherently noisy and experience far from the more ideal conditions present during phantom studies. For this reason, it was again hard to quantify an exact measure of accuracy for the measurement system described. However, it is possible to display results that give an idea of the effectiveness of the discussed concepts. The following section provides results of an experiment in which external artefact motion was purposely induced throughout data acquisition. A qualitative idea of the usefulness of the bone boundary method for motion artefact removal can be demonstrated by applying the motion removal algorithm to this data.

Due to the larger amounts of noise occurring during in vivo measurements compared to the simulation environment, the complex baseband signal was averaged with a window of 21 points axially and 10 points laterally. For all the results shown below, the probe was moved up and down into the forearm for the duration of the test. In addition, the EMS system was turned on sometime after two seconds and was set to a repetition rate of 4 Hz. The observation depth for the following figures was about 6.93 mm.

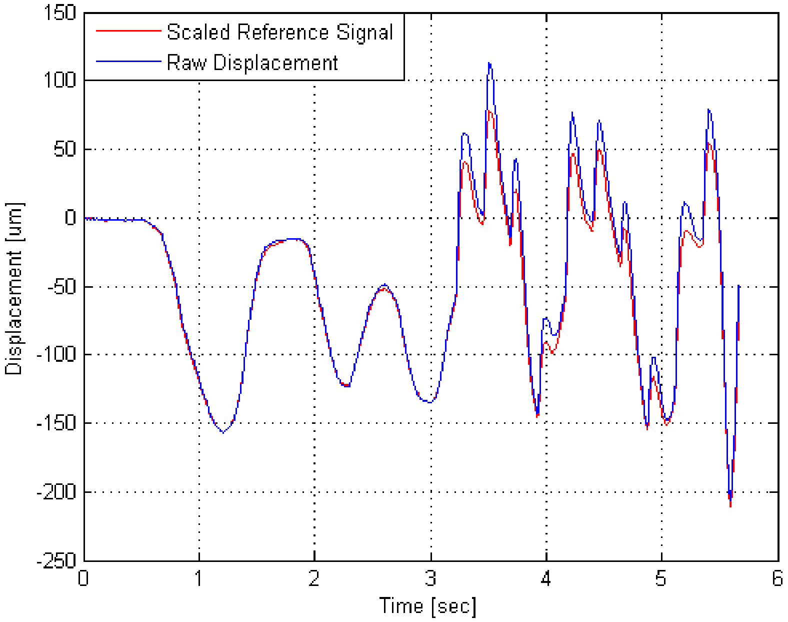

Figure 7.25 In vivo tissue displacement during 4 Hz EMS before motion artefact removal. The scaled bone reference signal (red) was subtracted from the raw measured displacement (blue) in order to obtain the motion corrected signal. Observed at a depth of about 6.93 mm.

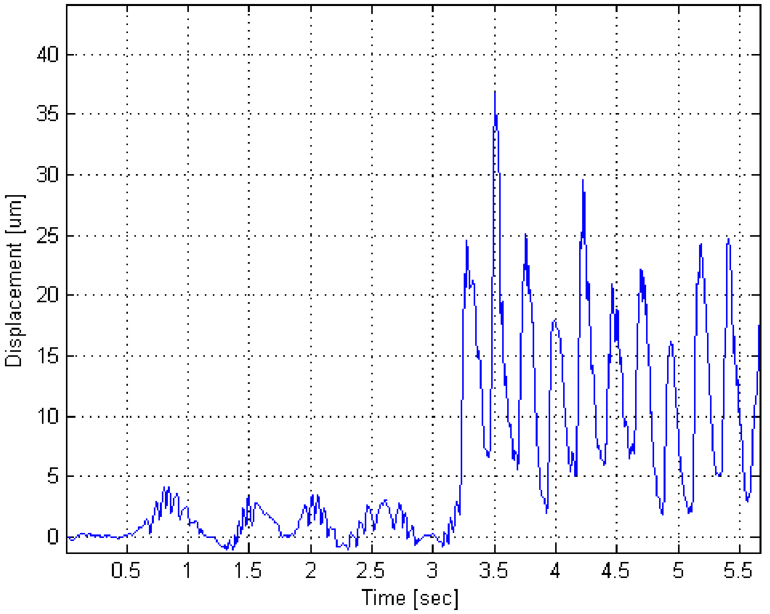

Figure 7.26 In vivo tissue displacement during 4 Hz EMS after motion artefact removal. Observed at a depth of about 6.93 mm.

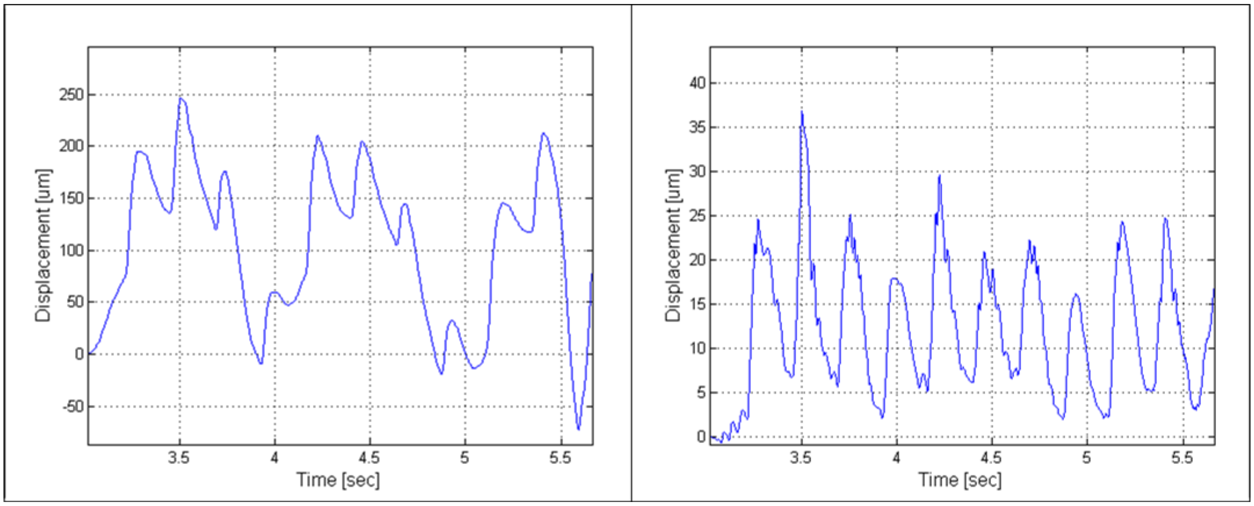

(a) (b)

Figure 7.27 In vivo tissue displacement during 4 Hz EMS. The displacement is shown before and after motion artefact removal in (a) and (b) respectively. Observed at a depth of about 6.93 mm.

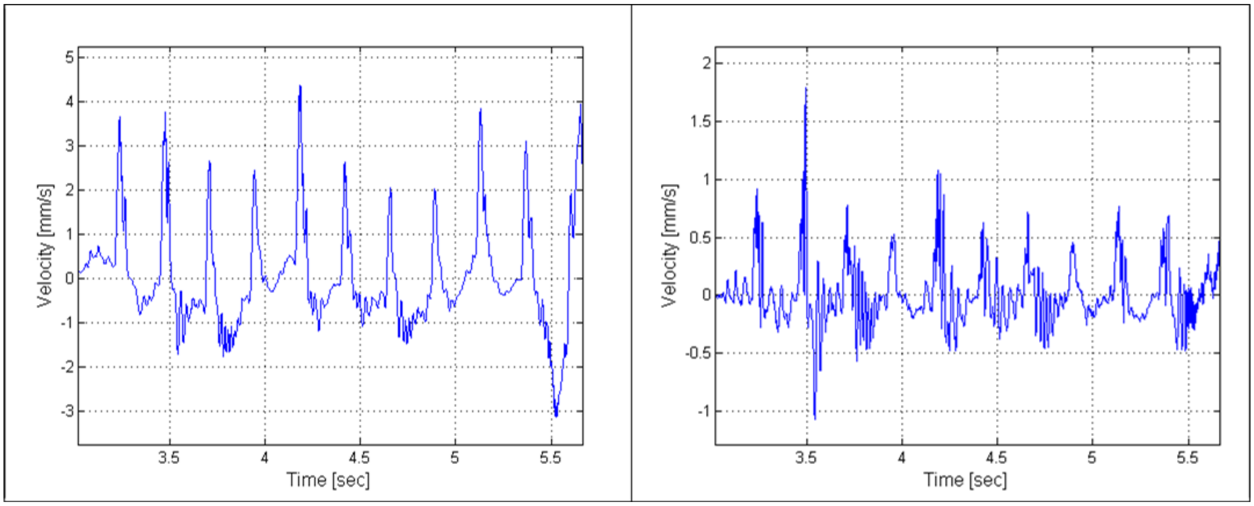

(a) (b)

Figure 7.28 In vivo tissue velocity during 4 Hz EMS. The velocity is shown before and after motion artefact removal in (a) and (b) respectively. Observed at a depth of about 6.93 mm.

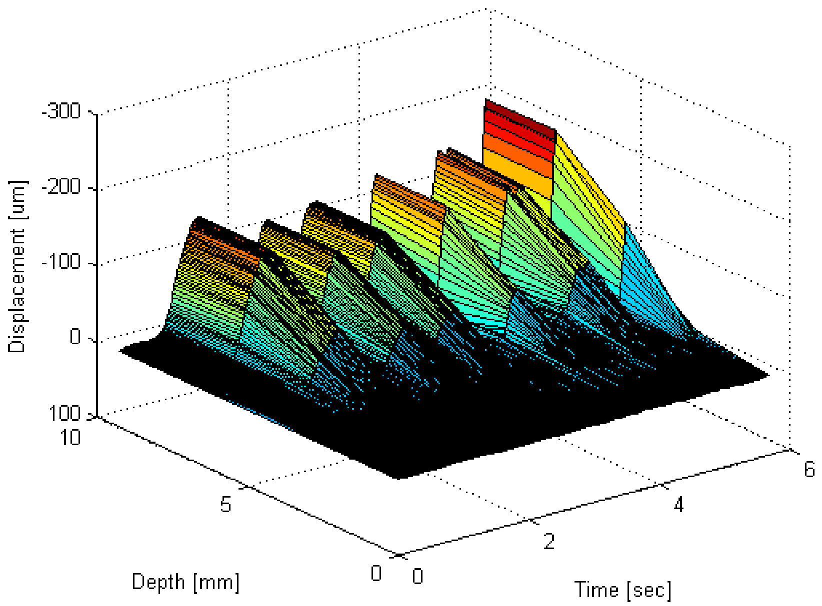

Figure 7.29 In vivo tissue displacement during 4 Hz EMS over all depth and time before motion artefact removal.

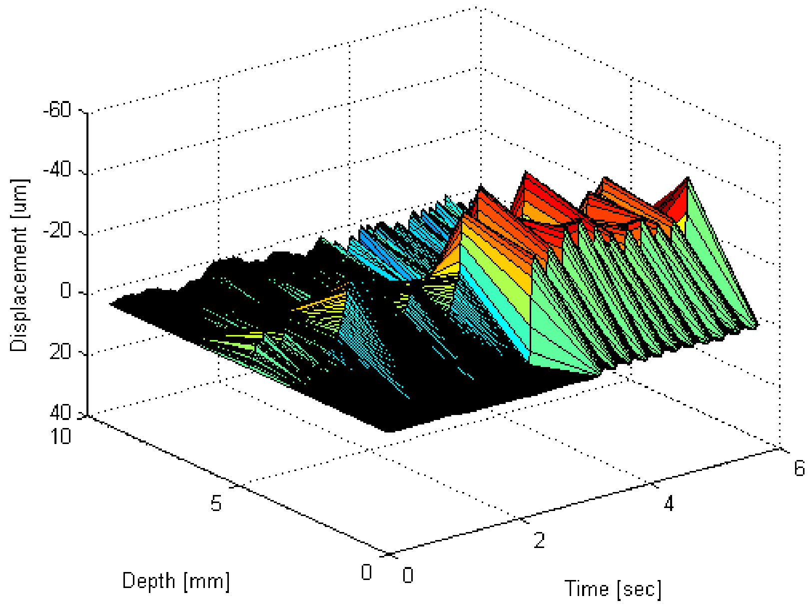

Figure 7.30 In vivo tissue displacement during 4 Hz EMS over all depth and time after motion artefact removal.

The above results demonstrate that the motion removal algorithm is a viable way to remove motion artefacts during in vivo experiments. These results show that after the motion removal algorithm has been applied the resultant signal is much less affected by the externally applied probe motion. It can be seen that the external motion has, for the most part, been removed and what is left behind is information about the internal motion of the tissue. After motion artefact removal, the displacement due to muscle stimulation is much more clearly observed.

Chapter 8:

Conclusions and Future Work

The following chapter concludes the thesis, summarizes the findings and suggests future work.

8.1 Overall Conclusions

This thesis examined the use of ultrasound techniques to study human skeletal muscles in terms of its relative motion and stiffness. The thesis provided background information on skeletal muscle anatomy, ultrasound physics and techniques that are currently used to study muscles. This was followed by a presentation and analysis of simulation and in vivo results.

In order to obtain results, experimental procedures and data processing algorithms were developed. In addition, both software and tissue mimicking phantom simulation environments were designed to model and test the muscle measurement system. The simulations were also used to evaluate the accuracy of the ultrasonic hardware as well as the developed and implemented algorithms. A GUI was also designed to allow a user quick, easy and intuitive access to their collected data.

Muscle analysis and measurements were made using a variety of existing and newly developed algorithms. In particular, using quadrature demodulation and autocorrelation methods, tissue displacement and velocity can be estimated both internally and globally. Internal tissue motion is estimated by applying a developed motion artefact removal algorithm. In addition, a strain estimation algorithm was implemented that provides a representation of the relative strain profile of the area being imaged.

The overall developed system was shown to be a viable means with which to obtain information about human skeletal muscle. This thesis demonstrates the systems application to estimating strain, tissue displacement and tissue velocity. It provides the novel ability to analyze muscle motion internally using the developed motion artefact removal algorithm.

8.2 Future Work

As stated a number of times throughout this thesis, the major purpose of the work done was to design a muscle measurement system and to validate the methodologies developed and employed. The research done was a first step in the direction of perfecting a system able to analyze muscle physiology and motion quantitatively. For this reason, there is a large amount of work remaining to be done in the future on optimizing the methodology used throughout this thesis. The following section outlines some suggestions for future research.

The phantom simulation environment has room for improvement. Improving on the relatively short useable lifetime of the tissue phantoms would increase the consistency between data acquired during different simulation experiments. In addition, more accurate and repeatable methods with which to apply force to an object being imaged should be considered. One way to do this could be to use a computer controllable mechanical stage to hold the ultrasonic probe. This would provide a way to apply very controllable stresses to an object being imaged.

Phase jumping was the largest source of error on measurements taken during this thesis research. It has been described and a means with which to remove its effects are provided in Section 4.6.2. Although a possible solution has been presented, the actual implementation of this solution during experimental data acquisition is left as future work. In addition, some work could be done on other ways with which to estimate motion using ultrasonic techniques. In this thesis, quadrature demodulation was applied to estimate phase shifts which were converted into displacement estimations. However, phase information can also be obtained using other techniques such as the Hilbert transform [49] or cross-correlation methods could be applied to the received RF ultrasonic signal to obtain displacement estimations [90].

Finally, there is a large amount of work to be done in the area of in vivo studies. The developed system provides a means to obtain a large amount of data about skeletal muscles. Due to the fact that it is capable of making a wide variety of measurements, it would make sense to spend time collecting and analyzing in vivo data in order to better understand skeletal muscle and to potentially make novel discoveries. The development of this system as a viable application for use in studying muscles depends largely on exploring and fully understanding the results obtained during in vivo experiments.

References

[1] D. U. Silverthorn, *Human Physiology: An integrated approach,* New Jersey: Prentice Hall, 1998, pp. 324-361.

[2] J. Kimball, “Muscles,” May 2009. [Online]. Available: *http://users.rcn.com/jkimball.ma.ultranet/BiologyPages/M/Muscles.html*. [Accessed: Jun. 29, 2009].

[3] J. W. Clark, “The origin of biopotentials,” in *Medical Instrumentation: Application and design,* 3rd ed., J. G. Webster, Ed. USA: John Wiley & Sons, 1998, pp. 121-182.

[4] D. A. Jones and J. M. Round, *Skeletal Muscle in Health and Disease: A textbook of muscle physiology,* Manchester, England: Manchester University Press, 1990. pp. 41-53.

[5] C. R. Bagshaw, *Muscle Contraction,* London, England: Chapman and Hall, 1982, pp. 11-29.

[6] J. H. Green, *An Introduction to Human Physiology,* 3rd Ed., London, England: Oxford University Press, 1972, pp. 179-189.

[7] K. S. Centofanti, “Electrical Stimulation for health, Beauty, Fitness, Sports Training and Rehabilitation: A users guide,” in *Advances in Muscle Research: Application of muscle/nerve stimulation in health and disease,* Vol. 4, G. J. M. Stienen Ed. Dordrecht, Netherlands: Springer Science + Business Media B.V., 2008, pp. 69-116.

[8] A. R. Sauter, M. S. Dodgson, A. Stunhaug, M. Cvancarova, and Ø. Klaastad, “Ultrasound controlled nerve stimulation in the elbow region: high currents and short distances needed to obtain motor responses,” *Acta Anaesthesiol Scand.,* Vol. 51, pp. 942-948, 2007.

[9] A. Perlas, A. Niazi, C.McCartney, V. Chan, D. Xu, and S. Abbas, “The sensitivity of motor response to nerve stimulation and paresthesia for nerve localization as evaluated by ultrasound,” *Regional Anesthesia and Pain Medicine,* Vol. 31, No.

5, pp. 445-450, Sept. 2006.

[10] A. M. Ali and Y-X. Qin, “Effects of electrically stimulated muscle contractions on bone loss and muscle atrophy,” *IEEE 33rd Annual Northeast Bioengineering Conference,* pp. 37-38, Jan. 2008.

[11] T. Helgason, P. Gargiulo, F. Jóhannesdóttir, P. Ingcarsson, S. Knútsdóttir, V. Gudmundsdóttir, and S. Yngvason, “Monitoring muscle growth and tissue changes induced by electrical stimulation of denervated degenerated muscles with CT and stereolithographic 3D modeling,” *Artif. Organs,* Vol. 29, pp. 441-443, Nov. 2005.

[12] J. L. Prince and J.M. Links, *Medical Imaging: Signals and Systems,* Upper Saddle River, NJ: Pearson Prentice Hall, 2006.

[13] D. A. Christensen, *Ultrasonic Bioinstrumentation,* U.S.A: John Wiley & Sons, 1988.

[14] P. Hoskins, A. Thrush, K. Martin, and T. Whittingam, *Diagnostic Ultrasound: Physics and equipment,* London, England: Greenwich Medical Media Limited, 2003.

[15] W. R. Hedrick, D. L. Hykes, and D. E. Starchman, *Ultrasound Physics and Instrumentation,* 4th ed., Missouri, U.S.A: Elesvier Mosby, 2005.

[16] F. W. Kremkau, *Diagnostic Ultrasound: Principles and Instruments,* 7th ed., Missouri, U.S.A: Saunders Elesvier, 2006.

[17] M. A. Mañanas, R. Jané, J. A. Fiz, J. Morera, and Pere Caminal, “Study of myographic signal from sternomastoid muscle in patients with chroni obstructive pulmonary disease,” *IEEE Transactions on Biomedical Engineering,* Vol. 47, No. 5, pp. 674-681, May 2000.

[18] M. Knaflitz and F. Molinari, “Assessment of muscle fatigue during biking,” *IEEE Transactions on Neural Sysytems and Rehabilitation Engineering,* Vol. 11, No. 1, pp. 17-23, Mar. 2003.

[19] T. Kondo, O. Amagi, and T. Nozawa, “Proposal of anticipatory patter recognition for EMG prosthetic hand control,” *IEEE International Conference on Systems, Man and Cybernetics,* pp. 897-902, 2008.

[20] L. Xu and A. Adler, “An improved method for muscle activation detection during gait,” *Canadian Conference on Electrical and Computer Engineering,* Vol. 1, pp.

357-360, May 2004.

[21] P. AAgaard, E. B. Simonsen, J. L. Andersen, P. Manusson, and P. Dyhre-Poulsen, "Increase rate of force development and neural drive of human skeletal muscle following resistance training," *J. Appl. Physiol.,* Vol. 93, pp. 1318-1326, Jul. 2002.

[22] J. C. Coggshall and G. A. Bekey, "EMG-Force dynamics in human skeletal muscle," *Medical and Biological Engineering and Computing,* Vol. 8, No. 3, pp. 265-270, Sept. 2006.

[23] P. K. Kasi, L. S. Krivickas, M. Meister, E. Chew, P. Bonata, M. Schmid, G. Karmen, L. Pu, E. A. Clancy, "Characterization of motor unit behavior in patients with amyotrophic lateral sclerosis", *Proceedings of the 4th International IEEE EMBS Conference on Neural Engineering,* pp. 10-13, May 2009.

[24] J. Guo, Y. Zheng, Q. Huang, X. Chen, and J. He, "Comparison of sonomyography and electromyography of forearm muscles in the guided wrist extension," *5th Internation Summer School and Symposium on Medical Devices and Biosensors,* pp. 235-238, Jun. 2008.

[25] M. T. Tarata, "Mechanomyography versus electromyography, in monitoring the muscular fatigue," *BioMedical Engineering OnLine,* Vol. 2, 2003. Available: BioMedical Engineering OnLine, http://www.biomedical-engineering-online.com/content/2/1/3. [Accessed June 24, 2009].

[26] M. I. A. Harba and G. E. Chee, "Muscle mechanomyographic and electromyographic signals compared with reference to action potential average propagation velocity," *Proceedings of the 19th International Conference of the IEEE EMBS,* Vol. 3, pp. 1282-1285, Nov. 1997.

[27] M. Kuozaki and T. Fukunagam, "Frequency features of mechanomyographic signals of human soleus muscle during quiet standing," *Journal of Neuroscience Methods,* Vol. 173, pp. 241-248, 2008.

[28] K. Akataki, K. Mita, and Y. Itoh, "Relationship between mechanomyogram and force during voluntary contraction reinvestigated using spectral decomposition," *Eur. J. Appl. Physiol.,* Vol. 80, pp. 173-179, Mar. 1999.

[29] C. Orizio, "Surface mechanomyography," in *Electromyography: Physiology, Engineering, and Noninvasive Applications*, R. Merletti and P. A. Parker, Ed. New Jersey: Wiley-IEEE Press, 2004, pp. 305-322.

[30] Y. Yoshitake, Y. Kawakami, H. Kanahisa, and T. Fukunaga, “Surface mechanomyogram reflects length changes in fascicles of human skeletal muscles,” *International Journal of Sport and Health Science,* Vol. 3, pp. 280-285, 2005.

[31] K. G. Sabra, S. Conti, P. Roux, and W. A. Kuperman, “Passive in vivo elastography from skeletal muscle noise,” *Applied Physics Letters,* Vol. 90, Issue 19, pp. 1-3, May 2007.

[32] W. L. C. Rutten, A. Wildeman, B. K. van Veen, and W. Wallinga, “In vivo magnetomyograms of skeletal muscle,” *Proceedings of the Annual Internal Conference of the IEEE in Engineering in Engineering in Medicine and Biology Society,* Vol. 3, pp. 981-982, Nov. 1989.

[33] G. ÓLaighin, B. J. Broderick, M. Clarke-Moloney, F. Wallis and P. A. Grace, “A technique for the computation of lower leg muscle volume from MRI images in the context of venous return,” *Proceedings of the 29th Annual International Conference of the IEEE EMBS,* pp. 951-954, Aug. 2007.

[34] P. Selskog, E. Heiberg, T. Ebbers, L. Wigström, and M. Karlsson, “Kinematics of the heart: strain-rate imaging from time-resolved three-dimensional phase contract MRI,”, *IEEE Transactions on Medical Imaging,* Vol. 21, No. 9, pp. 1105-1109, Sept. 2002.

[35] K. Hoyt, B. Casteneda, and K. J. Parker, “Muscle Tissue Characterization using quantitative sonoelastography: preliminary results,” *IEEE Ultrasonics Symposium,* pp. 365-368, Oct. 2007.

[36] S. Pillen, R. O. Tak, M. J. Zwarts, M. M. Y. Lammens, K. N. Verrijp, I. M. P. Arts, J. A. van der Laak, P. M. Hoogerbrugge, B. G. M. van Engelen, and A. Verrips, “Skeletal muscle ultrasound: correlation between fibrous tissue and echo intensity,” *Ultrasound in Med. & Biol.*, Vol. 35, No. 3, pp. 443-446, 2009.

[37] N. R. Grubb, A. Fleming, G. R. Sitherlan, and K. A. A. Fox, “Skeletal muscle contraction in healthy volunteers: assessment with Doppler tissue imaging,” *Radiology,* Vol. 194, pp. 837-842, 1995.

[38] T. Deffieux, J. Gennisson, M. Tanter, and M. Fink, “Ultrafast ultrasonic imaging of in vivo muscle contraction,” *IEEE Ultrasonics Symposium,* pp 1001-1004., Oct. 2006.

[39] T. Miyoshi, T. Kihara, H. Koyama, S. Yamamoto, and T. Komeda, “Automatic detection method of muscle fiber movement as revealed by ultrasound images,”

Medical Engineering & Physics, Vol. 31, Issue 5, pp. 558-564, Jun. 2008.

[40] J. Guo, Y. Zheng, Q. Huang, X. Chen, "Dynamic monitoring of forearm muscle using one-dimensional sonomyography system," *Journal of Rehabilitation Research & Development,* Vol. 45, No. 1, pp. 187-196, 2008.

[41] P. W. Hodges, L. H. M. Pengel, R. D. Herbert, and S. C. Gandevia, "Measurement of muscle contraction with ultrasound imaging," *Muscle and Nerve,* Vol. 27, pp. 682-692, Feb. 2003.

[42] I. D. loram, C. N. Maganaris, and M. Lakie, "Use of ultrasound to make noninvasive in vivo measurements of continuous changes in human muscle contractile length," *J. Appl. Physiol.,* Vol. 100, pp. 1311-1323, Dec. 2005.

[43] L. Herrington and S. Pearson, "The applicability of ultrasound imaging in the assessment of dynamic patella tracking: a preliminary investigation," *The Knee,* Vol. 15, Issue 2, pp. 125-127, Mar. 2008.

[44] Q. Peng and L. Zhang, "Ultrasound evaluation of mechanical properties of individual muscles-tendons during active contraction," *Proceedings of the 27th Annual International Conference of the IEEE EMBS,* pp. 7436-7439, Jan. 2006.

[45] A. Nordez, J. L. Gennisson, P. Casari, S. Catheline, and C. Cornu, "Characterization of muscle belly elastic properties during passive stretching using transient elasrography," *Journal of Biomechanics,* Vol. 41, pp. 2305-2311, Mar. 2008.

[46] J. Farron, T. Varghese, and D. G. Thelen, "Measurement of tendon strain during muscle twitch contractions using ultrasound elastography," *IEEE Transactions on Ultrasonics, Ferroelectrics, and Frequency Control,* Vol. 56, No. 1, pp. 27-35, Jan. 2009.

[47] K. Hoyt, T. Kneezel, B. Casteneda, and K. J. Parker, "Quantitative Sonoelastography for the in vivo assessment of skeletal muscle viscoelasticity," *Phys. Med. Biol.,* Vol. 53, pp. 4063-4080, 2008.

[48] J. Gennison, S. Catheline, S. Chaffaï, and M. Fink, "Transient elastography in anisotropic medium: application to the measurement of slow and fast shear wave speeds in muscles," *J. Acoust. Soc. Am.,* Vol. 114, Issue 1, pp. 536-541, Jul. 2003.

[49] P. J. Brands, A. P. G. Hoeks, L. A. F. Ledoux, and R. S. Reneman, "A radio frequency domain complex cross-correlation model to estimate blood flow

velocity and tissue motion by means of ultrasound," *Ultrasound in Med. & Biol.,* Vol. 23, No. 6, pp. 911-920, 1997.

[50] A. P. G. Hoeks, T. G. J. Arts, P. J. Brands, and R. S. Reneman, "Comparison of the performance of the RF cross correlation and Doppler autocorrelation technique to estimate the mean velocity of simulated ultrasound signals," *Ultrasound in Med. & Biol.*, Vol. 19, No. 9, pp. 727-740, 1993.

[51] V. W. S. Chan, "Applying ultrasound imaging to interscalene brachial plexus block," *Regional Anesthesia and Pain Medecine,* Vol. 28, No. 4, pp. 340-343, Aug. 2003.

[52] B. Hete and K. Shung, "Using RF ultrasound to monitor the progression of muscular dystrophy through passive stretching," *Proceedings of the IEEE Ultrasonics Symposium,* Vol. 2, pp. 1123-1126, Dec. 1991.

[53] Y. Liu, S. Chen, C. Lin, C. Huang, and Y. Sun, "Motion tracking on elbow tissue from ultrasonic image sequence for patients with lateral epicondylitis" *Processings of the 29th Annual International Conference of the IEEE EMBS,* pp. 95-98, Aug. 2007.

[54] J. Shi, Y. P. Zheng, X. Chen, and Q. H. Huang, "Assessment of muscle fatigue using sonomyography: muscle thickness change detected from ultrasound images," *Medical Engineering & Physics,* Vol. 29, pp. 472-479, 2007.

[55] Y. P. Zheng, M. M.F. Chan, J. Shi, X. Chen, and Q. H. Huang, "Sonomyography: monitoring morphological changes of forearm muscles in actions with the feasibility for the control of powered prosthesis," *Medical Engineering & Physics,* Vol. 28, pp. 405-415, 2006.

[56] U. Bae, and Y. Kim, "Angular strain estimation method for elastography," *IEEE Transaction on Ultrasonics, Ferroelectrics and Frequency Control,* Vol. 54, No. 12, pp. 2653-2661, Dec. 2007.

[57] Esaote© Europe, "Picus User Manual: Instructions for Use and Technical Description", 2008.

[58] Brands, P.J., "Ultrasound Installation and Orientation Session", Carleton University, August, 2008.

[59] "Ultrasound Probes," 2009. [Online]. Available: http://www.esaote.com/modules/core/page.asp?p=US_TRANSDUCERS. [Accessed: May 22, 2009].

[60] A. C. H. Yu, A. H. Steinman, and R. S. C. Cobbold, "Transit-time broadening in pulsed Doppler ultrasound: A generalized amplitude modulation model," *IEEE Transaction on Ultrasonics, Ferroelectrics, and Frequency Control,* Vol. 53, No. 3, pp. 531-541, Mar. 2006.

[61] F. J. de Ana and M. O'Donnel, "Quantitative real-time blood flow estimation with intravascular ultrasound in the presence on in-plane flow," *IEEE Transactions on Ultrasonics, Ferroelectrics, and Frequency Control,* Vol. 52, No. 11, pp. 1952-1961, Nov. 2005.

[62] D. H. Evans, W. N. McDicken, *Doppler Ultrasound: Physics, instrumentation and signal processing,* 2nd ed., West Sussex, England: John Wiley & Sons, 2000, pp. 43-67.

[63] S. Huang, R. M. Lerner, and K. J. Parker, "On estimating the amplitude of harmonic vibration from the Doppler spectrum of reflected signal," *J. Acoust. Soc. Am.,* Vol. 88, No. 6, pp. 2702-2712, Dec. 1990.

[64] S. Huang, R. M. Lerner, and K. J. Parker, "Time domain Doppler estimators of the amplitude of vibrating targets," *J. Acoust. Soc. Am.,* Vol. 91, No. 2, pp. 965-974, Feb. 1992.

[65] Y. Tamakoshi, J. Sato and T. Sato, "Ultrasonic imaging of internal vibration of soft tissue under forced vibration," *IEEE Transaction on Ultrasonics, Ferroelectrics, and Frequency Control,* Vol. 37, No. 2, pp. 45-53, Mar. 1990.

[66] H. Kanai, H. Satoh, K. Hirose, and N. Chubachi, "A new method for measuring small local vibrations in the heart using ultrasound," *IEEE Transactions on Biomedical Engineering,* Vol. 40, No. 12, pp. 1233-1241, Dec. 1993.

[67] J. Holen, R. C. Waag, and R. Gramiak, " Representations of rapidly oscillating structures on the Doppler display," *Ultrasound in Med. & Biol.,* Vol. 11, No. 2, pp. 267-272, Apr. 1985.

[68] R. Omoto, and C. Kasai, "Basic principles of Doppler color flow imaging," *Echocardiography A Review of Cardiovascular Ultrasound,* Vol. 3, No 6, pp. 463-473, 1986.

[69] L. W. Couch, *Digital and Analog Communication Systems: Sixth Edition,* Upper Saddle River, NJ: Pearson Prentice Hall, 2001, pp. 318-332.

[70] N. Aydin, and H.S. Markus, "Time-scale analysis of quadrature Doppler ultrasound signals," *IEE Proc.-Sci. Meas. Technol.* Vol. 148, No. 1, pp. 15-22,

Jan 2001.

[71] N. Feng, J. Zhang, and W. Wang, “A quadrature demodulation method based on tracking the ultrasound echo frequency,” Vol. 44, pp. 47-50, June 2006.

[72] M. E. Anderson, “A heterodyning demodulation technique for spatial quadrature,” *IEEE Ultrasonics Symposium,* pp. 1487-1451, 2000.

[73] M. E. Anderson, “Multi-dimensional velocity estimation with ultrasound using spatial quadrature,” *IEEE Transaction on Ultrasonics, Ferroelectrics and Frequency Control,* Vol. 45, No. 3, pp. 852-861, May 1998.

[74] P. Levesque, and M. Sawam, “New digital quadrature demodulator for real-time hand-held ultrasound medical imaging device,” *IEEE International Symposium on Circuits and Systems,* pp. 2949–2952, May 2008.

[75] G. F. Pinton, J. J. Dahl, and G. E. Trahey, “Rapid tracking of small displacements with ultrasound,” *IEEE Transaction on Ultrasonics, Ferroelectrics and Frequency Control,* Vol. 53, No. 6, pp. 1103-1117, June 2006.

[76] S. H. Chang, S. B. Park, and G. H. Cho, “Phase-error-free quadrature sampling technique in the ultrasonic B-Scan imaging system and its application to the synthetic focusing system,” *IEEE International Symposium on Circuits and Systems,* Vol. 40, No. 3, pp. 216-223, May 1993.

[77] T. Loupas, J.T. Powers, and R. W. Gill, “An axial velocity estimator for ultrasound blood flow imaging, based on a full evaluation of the Doppler equation by means of a two-dimensional autocorrelation approach,” *IEEE Transaction on Ultrasonics, Ferroelectrics and Frequency Control,* Vol. 42, No. 4, pp. 672-688, July. 1995.

[78] H. Trop, K. Kristoffersen, and B. A. J. Andelsen, “Autocorrelation techniques in color imaging: signal model and statistical properties of the autocorrelation estimates,” *IEEE Transaction on Ultrasonics, Ferroelectrics and Frequency Control,* Vol. 41, No. 5, pp. 604-612, Sept. 1994.

[79] C. Kasai, K. Namekawa, A. Koyano, and R. Omoto, “Real time two-dimensional blood flow imaging using an autocorrelation technique,” *IEEE Transactions on Sonics and Ultrasonics,* Vol. SU-32, No. 3, pp. 458-464, May 1985.

[80] H. Hasegawa, and H. Kanai, “Reduction of influence of variation in center frequencies of RF echoes on estimation of artery-wall strain,” *IEEE Transaction*

on Ultrasonics, Ferroelectrics and Frequency Control, Vol. 55, No. 9, pp. 1921-1934, Sept 2008.

[81] V. Shamdasani and Y. Kim, "Two-dimensional autocorrelation method for ultrasound-based strain estimation," *Proceedings of the 26th Annual International Conference of the IEEE EMBS,* Vol. 1 pp. 1380-1383, Sept. 2004.

[82] S. I. Rabben, S. Bjærum, V. Sørhus, and H. Torp, " Ultrasound-based vessel wall tracking: an autocorrelation technique with RF center frequency estimation," *Ultrasound in Med. & Biol.,* Vol. 28, No. 4, pp. 507-517, 2002.

[83] X. Lai, H. Torp, and K. Kristoffersen, "An extended autocorrelation method for estimation of blood velocity," *IEEE Transaction on Ultrasonics, Ferroelectrics and Frequency Control,* Vol. 44, No. 6, pp. 1332-1342, Nov. 1997.

[84] J. D'hooge, A. Heimdal, F. Jamal, T. Kukulski, B. Bijnens, F. Rademakers, L. Hatle, P. Suetens, and G. R. Sutherland, "Regional strain and strain rate measurements by cardiac ultrasound: principles, implementation and limitations," *Eur J Echocardiography,* Vol. 1, pp. 154-170, 2000.

[85] R. Souchon, "Ultrasound elastography, " in *Physics for medical imaging applications*, Vol. 240 Netherlands: Springer, 2007, pp.197-209.

[86] A. Hein, and W. D. O'Brien, Jr., "Time-domain methods for assessing tissue motion be analysis from reflected ultrasound echoes-a review," *IEEE Transaction on Ultrasonics, Ferroelectrics and Frequency Control,* Vol. 40, No. 2, pp. 84-102, Mar. 1993.

[87] M. O'Donnell, A. R. Skovoroda, B. M. Shapo, and S. Y. Emelianov, "Internal displacement and strain imaging using ultrasonic speckle tracking,", *IEEE Transaction on Ultrasonics, Ferroelectrics and Frequency Control,* Vol. 41, No. 3, pp. 314-325, May 1994.

[88] A. R. Skovoroda, S. Y. Emelianov, M. A. Lubinski, A. P. Sarvazyan, and M. o'Donnell, "Theoretical analysis and verification of ultrasound displacement and strain imaging," *IEEE Transaction on Ultrasonics, Ferroelectrics and Frequency Control,* Vol. 41, No. 3, pp. 302-313, May 1994.

[89] Y. Yamashita, and M. Kubota, "Tissue elasticity reconstruction based on ultrasonic strain measurements," *IEEE Ultrasonics Symposium Proceedings,* Vol. 2, pp. 1113-1116, Nov. 1996.

[90] J. Ophir, I. Céspedes, H. Ponnekanti, Y. Yazdi and X. Li, "Elastography: a quantitative method for imaging the elasticity of biological tissues." *Ultrasonic*

Imaging, Vol. 13, pp. 111-134, 1991.

[91] S. A. Gross, R. L. Johnston and F. Dunn, “Comprehensive compilation of empirical ultrasonic properties of mammalian tissues,” *J. Acoust. Soc. Am.,* Vol. 64, No. 2, pp 423-457, Aug. 1978.

[92] M. Weichenthal, P. Mohr and E. W. Greitbart, “The velocity of ultrasound in human primary melanoma tissue – implications for the clinical use of high resolution sonography,” *BMC Dermatology 2001,* Vol. 1, June 2001.

[93] C. R. Mol and P. A. Breddels, ”Ultrasound velocity in muscle,” *J. Acoust. Soc. Am.,* Vol. 71, No. 2, pp. 455-461, Feb 1982.

[94] Z. Wu, L. S. Taylor, D. J. Rubens and K. J. Parker, “Sonoelastographic imaging of interference patterns for estimation of the shear velocity of homogeneous biomaterials,” *Phys. Med. Biol.,* vol. 49, pp. 911-927, Feb. 2004.

[95] K. Kawabata, Y. Waki, T. Matsumura and S. Umemura, “Tissue mimicking phantom for ultrasonic elastography with finely adjustable elastic and echographic properties,” *2004 IEEE Ultrasonics Symposium,* Vol. 2, pp. 1502-1505, Aug. 2004.

[96] E. L. Madsen, J. A. Zagzebski, R. A. Banjavie and R. E. Jutila, “Tissue mimicking materials for ultrasound phantoms,” *Medical Physics,* Vol. 5, No. 5, pp. 391-394, May 1978.

[97] “Forearm Training,” 2008. [Online]. Available: http://www.illpumpyouup.com/articles/forearm-training.htm. [Accessed: June 12, 2009].

[98] “EMS 7500,” [Online]. Available: http://austinmedical.stores.yahoo.net/ems7500.html. [Accessed: June 12, 2009].

[99] “Instant Anatomy,” 2006. [Online]. Available: http://www.instantanatomy.net/arm/areas/forearm/pcrosssection.html. [Accessed: June 22, 2009].